

FACULTY FOR PHYSICS AND ASTRONOMY

UNIVERSITY OF HEIDELBERG

Diploma Thesis

in Physics

submitted by

Johannes Hendrik Stiller

born in Cologne, Germany

2011

**Gain Calibration
of the ALICE TRD using
the Decay of $^{83\text{m}}\text{Kr}$
and
Alignment of the ALICE TRD**

This diploma thesis has been carried out by
Johannes Hendrik Stiller
at the Physikalisches Institut Heidelberg
under the supervision of
Helmholtz Young Investigator
Dr. Kai Schweda

Gain calibration of the ALICE Transition Radiation Detector (TRD) using the decay of $^{83\text{m}}\text{Kr}$ and alignment of the ALICE TRD.

The TRD is an important subsystem of the ALICE experiment, because it provides excellent electron identification and a fast trigger. Each of the 522 TRD readout chambers consists of a radiator and a multi-wire proportional chamber with a drift region. The cathode pad plane of each chamber is segmented into either 16×144 or 12×144 readout pads, giving a total number of 1,150,848 pads. For the gain calibration at the level of individual pads, a dedicated calibration run with a radioactive Krypton source has been carried out. We have recorded 2.67×10^9 decays of metastable $^{83\text{m}}\text{Kr}$ in the 10 supermodules presently installed in the ALICE cavern. The gain calibration of each chamber on a pad-by-pad level was improved to better than 2 % resolution in an iterative analysis. Measured gain maps of all chambers were compared to data from the individual chamber construction sites and good agreement was found. The gain dependence on the high voltage was measured and compared to detailed prototype measurements. The gain dependence on the atmospheric pressure, the energy resolution and the linear signal processing of the readout chambers were determined. The pad-by-pad gain factors of all installed chambers are uploaded into the data base and made available for offline analysis and download to the TRD Front-End Electronics ensuring trigger stability. In a second part of this thesis, all installed TRD readout chambers were aligned relative to the ALICE Time Projection Chamber, and thus the momentum and spatial resolution in the central barrel of the ALICE experiment strongly improved.

Kalibrierung der Verstärkungsfaktoren des ALICE Übergangsstrahlungsdetektors (TRD) unter Verwendung des Zerfalls von $^{83\text{m}}\text{Kr}$ und Ausrichtung des ALICE TRD.

Auf Grund seiner hervorragende Elektronenidentifikation und einem schnellen Trigger ist der TRD ein wichtiger Bestandteil des ALICE Experiments. Jede der 522 TRD Ausleseammern besteht aus einem Strahlmedium und einer Vieldraht-Proportionalkammer mit Driftregion, wobei die Kathodenpadebene in 16×144 oder 12×144 Auslesepads unterteilt ist. Dies ergibt eine Gesamtzahl von 1,150,848 Pads. Zum Zweck der Kalibrierung der Verstärkungsfaktoren der einzelnen Pads, wurde eine Datenaufnahme mit einer radioaktiven Kryptonquelle durchgeführt. Insgesamt sind 2.67×10^9 Zerfälle des metastabilen $^{83\text{m}}\text{Kr}$ in den 10, momentan in der ALICE Kaverne installierten Supermodulen gemessen worden. In einer iterativen Analyse ist die Kalibrierung der Verstärkungsfaktoren in diesen Kammern auf Padniveau auf weniger als 2 % verbessert worden. Pad-Verstärkungsfaktoren wurden für jede Kammer mit Daten von der Kammerkonstruktion verglichen, und gute Übereinstimmung wurde gefunden. Die Abhängigkeit der Verstärkung von der Hochspannung ist gemessen und mit detaillierten Prototypmessungen verglichen worden. Die Abhängigkeit der Verstärkung vom atmosphärischem Druck, die Energieauflösung sowie die lineare Datenverarbeitung der Ausleseammerelektronik wurden bestätigt. Die einzelnen Padverstärkungsfaktoren sind nun in die Datenbank integriert und stehen für Offlineanalysen sowie zum Herunterladen in die Ausleseammerelektronik für einen stabilen Trigger zur Verfügung. Im zweiten Teil dieser Arbeit wurden alle installierten TRD Ausleseammern relativ zu der ALICE Zeit-Projektionskammer ausgerichtet und dadurch die Impuls- und Raumauflösung im zentralen Teil des ALICE Experiments deutlich verbessert.

Contents

| | |
|--|------------|
| Contents | vii |
| List of Figures | x |
| List of Tables | xii |
| 1. Introduction | 1 |
| 2. Theoretical Background | 4 |
| 2.1. Basic Constituents of Matter | 4 |
| 2.1.1. The Standard Model of Particle Physics | 4 |
| 2.1.2. The Quark-Gluon Plasma | 5 |
| 2.1.3. QGP in Heavy Ion Collisions | 7 |
| 2.2. Interactions of Particles and Matter | 8 |
| 2.2.1. Energy Loss of charged Particles | 8 |
| 2.2.2. Bethe Equation | 8 |
| 2.2.3. Bremsstrahlung | 9 |
| 2.2.4. Transition Radiation | 10 |
| 2.3. Amplification of Ionization | 11 |
| 2.3.1. Gain of the Proportional Wire | 12 |
| 2.3.2. The Role of Photons and the Penning Effect | 13 |
| 2.3.3. Local Variations of the Gain | 14 |
| 3. CERN and the LHC | 20 |
| 3.1. The Large Hadron Collider | 20 |
| 3.2. The ALICE Detector | 22 |
| 4. The ALICE Transition Radiation Detector | 25 |
| 4.1. The TRD Design | 25 |
| 4.2. The TRD Readout Chamber | 26 |
| 4.2.1. Radiator | 27 |
| 4.2.2. Multi-Wire Proportional Chamber with Drift Region | 28 |
| 4.2.3. Front-End Electronics | 30 |
| 4.3. Chamber Numbering | 31 |
| 4.4. The ALICE Coordinate System | 32 |
| 5. Concept of Calibrating with Krypton | 34 |
| 5.1. Krypton Properties | 34 |
| 5.2. Range of Krypton Decay Electrons | 36 |

| | |
|---|-----------|
| 6. Experimental Setup and Data Taking of the Krypton Calibration | 39 |
| 6.1. Foregoing Considerations | 39 |
| 6.1.1. Properties of the available Rubidium Source | 39 |
| 6.1.2. Data and Statistics | 40 |
| 6.2. Experimental Setup | 42 |
| 6.3. Data Taking | 42 |
| 6.4. Experimental Conditions during Data Taking | 43 |
| 6.4.1. Increase of Gas Flow | 44 |
| 6.4.2. Change of Atmospheric Pressure | 45 |
| 6.4.3. Gas Admixture | 45 |
| 6.4.4. High Voltage Stability | 46 |
| 7. Analysis and Results | 48 |
| 7.1. Global Reconstruction and Analyzed Datasets | 48 |
| 7.2. Analysis Strategy | 49 |
| 7.3. The Krypton Cluster Finder Algorithm | 51 |
| 7.3.1. Noise Analysis | 51 |
| 7.4. Fit Analysis | 56 |
| 7.4.1. Fit Quality | 59 |
| 7.5. Spectra Analysis | 60 |
| 7.5.1. Spectra recorded in Pads | 60 |
| 7.5.2. Spectra reconstructed in Chambers | 61 |
| 7.5.3. Energy Resolution Measurement | 61 |
| 7.5.4. Linearity | 62 |
| 7.5.5. Gain Variations due to Pressure Changes | 65 |
| 7.6. Gain Factor Analysis | 66 |
| 7.6.1. Gain Factor Distribution of all installed Chambers | 67 |
| 7.6.2. Iterative Analysis Steps | 68 |
| 7.6.3. Gain Maps of single Chambers | 69 |
| 7.6.4. Chambers and Pads excluded from the Analysis | 71 |
| 7.7. Comparison to the previous Method | 72 |
| 7.8. Comparison to Gain Uniformity Measurements | 75 |
| 7.9. Correlation between Gain and Anode Voltage | 78 |
| 7.9.1. Analysis Strategy and Results | 78 |
| 8. Alignment of the ALICE TRD | 83 |
| 8.1. Motivation | 83 |
| 8.2. Analysis Strategy and Theory | 83 |
| 8.2.1. Alignment Parameters | 84 |
| 8.2.2. Alignment with Particle Trajectories | 85 |
| 8.2.3. Alignment with Collisions from 2011 | 86 |
| 8.3. Results | 88 |
| 9. Summary and Outlook | 93 |

| | |
|--|------------|
| A. Appendix | 95 |
| A.1. Acronyms and Technical Terms | 95 |
| A.2. Chambers used in the Analysis | 96 |
| Bibliography | 106 |

List of Figures

| | | |
|------|---|----|
| 1.1. | PbPb collisions at $\sqrt{s_{NN}} = 2.76$ ATeV in ALICE. | 2 |
| 2.1. | The Standard Model. | 4 |
| 2.2. | The QCD phase diagram. | 6 |
| 2.3. | Simulation of a heavy ion collision. | 7 |
| 2.4. | Mean rate of energy loss for positive muons in copper. | 9 |
| 2.5. | Fractional energy loss per radiation length in lead for electrons or positrons. | 10 |
| 2.6. | Model of mirror charge. | 11 |
| 2.7. | Evolution of a charge avalanche near a proportional wire. | 12 |
| 2.8. | Example of a TPC geometry. | 15 |
| 3.1. | The accelerator complex at CERN. | 21 |
| 3.2. | The ALICE experiment. | 23 |
| 4.1. | Axonometric view of the ALICE space frame. | 25 |
| 4.2. | The ALICE TRD readout chamber. | 26 |
| 4.3. | TRD readout chamber with electric field lines. | 27 |
| 4.4. | Testbeam data for electrons and pions. | 28 |
| 4.5. | Schematic view of the sandwich radiator. | 28 |
| 4.6. | Schematic view of the multi-wire proportional chamber. | 29 |
| 4.7. | Logical components of the TRD Front-End Electronics. | 31 |
| 4.8. | Axonometric view of the ALICE TRD components. | 32 |
| 4.9. | Schematic drawing of the ALICE TRD pad plane. | 33 |
| 5.1. | Schematic drawing of the decay of ^{83}Rb into ^{83}Kr | 35 |
| 5.2. | Expected ^{83}Kr decay spectrum. | 37 |
| 5.3. | Range of the Krypton decay electrons. | 38 |
| 6.1. | Estimated activity of the ^{83}Rb source during data taking. | 39 |
| 6.2. | Installation status of the ALICE TRD sectors. | 40 |
| 6.3. | Schematic layout of the TRD gas system. | 42 |
| 6.4. | Schedule plot of the 2011 Krypton calibration campaign. | 43 |
| 6.5. | Schematic drawing of the gas inlets in a TRD sector. | 44 |
| 6.6. | Statistical distribution of Krypton decays in each sector for each chamber. | 45 |
| 6.7. | Cavern pressure as a function of time. | 46 |
| 6.8. | Standalone simulation of electron and pion dE/dx. | 47 |
| 7.1. | Flow chart of the Krypton cluster finder. | 52 |
| 7.2. | Visualization of the working principle of the ^{83}Kr cluster finder. | 53 |
| 7.3. | Krypton decay spectrum of chamber (0-0-0) with and without noise cuts. | 54 |

| | | |
|-------|---|----|
| 7.4. | Example of "shot noise". | 55 |
| 7.5. | Signal distribution as a function of root mean square time and ADC counts. | 56 |
| 7.6. | Krypton spectrum assigned to a single pad. | 57 |
| 7.7. | Principle of pad smoothing. | 58 |
| 7.8. | Reduced Chi-square distribution. | 59 |
| 7.9. | Fit of the pad spectrum on the reference spectrum. | 60 |
| 7.10. | ^{83}Kr decay spectrum of chamber (0-0-0). | 62 |
| 7.11. | Energy resolution for all pads in chamber (15-1-0). | 63 |
| 7.12. | Energy resolution for all chambers. | 63 |
| 7.13. | Linear relation between gain and electron energy in chamber (0-0-0). | 64 |
| 7.14. | Gain and pressure as a function of time. | 66 |
| 7.15. | Gain factor distribution in all chambers. | 67 |
| 7.16. | Gain factor distribution of all pads in all installed chambers. | 68 |
| 7.17. | Iterative development of the pad gain correction in a chamber. | 69 |
| 7.18. | Gain map of chamber (16-4-2). | 70 |
| 7.19. | Gain map of chamber (15-1-0). | 71 |
| 7.20. | Spectrum recorded in a noisy chamber. | 72 |
| 7.21. | Floating pad of chamber (15-1-2). | 73 |
| 7.22. | Comparison of the new and old fitting algorithms. | 74 |
| 7.23. | Profile of the ratio of the relative gain factors. | 74 |
| 7.24. | Gain uniformity measurement during construction of chamber (16-1-3). | 76 |
| 7.25. | Gain map of chamber (16-1-3). | 77 |
| 7.26. | Profile comparison between gain maps. | 77 |
| 7.27. | Decay spectra of chamber (0-0-0) for different anode high voltage settings. | 79 |
| 7.28. | Mean of the main decay peak in ADC counts as a function of anode voltage. | 79 |
| 7.29. | Distribution of slope parameters of all installed chambers. | 81 |
| 7.30. | Correlation between gain and high voltage for small-sized prototypes. | 82 |
| 8.1. | Possible misalignment of a TRD readout chamber. | 84 |
| 8.2. | Working principle of the global tracking algorithm. | 85 |
| 8.3. | Working principle of the offline alignment procedure. | 87 |
| 8.4. | Track point distribution in the installed TRD chambers. | 88 |
| 8.5. | 2-dimensional view of the track points used for alignment. | 89 |
| 8.6. | $r\phi$ -shift and -tilt alignment parameters. | 90 |
| 8.7. | z -shift and -tilt alignment parameters. | 91 |
| 8.8. | r -shift and -tilt alignment parameters. | 92 |

List of Tables

| | |
|---|-----|
| 2.1. Gain variations caused by mechanical imperfection. | 17 |
| 4.1. Chamber types and their specifications. | 30 |
| 5.1. Minimum ionization energy in different gases. | 34 |
| 5.2. Krypton decay scheme. | 36 |
| 5.3. Range of Krypton decay electrons. | 38 |
| 6.1. Ordering scheme of the installed chambers. | 40 |
| 6.2. TRD setup during data taking. | 41 |
| 6.3. Runs recorded for the 2011 Krypton calibration campaign. | 43 |
| 7.1. Processed runs with nominal and reduced high voltage settings. | 49 |
| 7.2. Applied cuts in the Krypton cluster finder. | 55 |
| 7.3. Processed runs with nominal and reduced high voltage settings. | 65 |
| 7.4. Chambers excluded from the calibration. | 71 |
| 7.5. List of chamber types and their construction site. | 75 |
| 8.1. Cuts imposed on track points used for alignment. | 88 |
| A.1. Overview of the settings of the chambers in supermodule II installed in TRD sector 00. | 96 |
| A.2. Overview of the settings of the chambers in supermodule VI installed in TRD sector 01. | 97 |
| A.3. Overview of the settings of the chambers in supermodule III installed in TRD sector 07. | 98 |
| A.4. Overview of the settings of the chambers in supermodule I installed in TRD sector 08. | 99 |
| A.5. Overview of the settings of the chambers in supermodule IV installed in TRD sector 09. | 100 |
| A.6. Overview of the settings of the chambers in supermodule VII installed in TRD sector 10. | 101 |
| A.7. Overview of the settings of the chambers in supermodule IX installed in TRD sector 11. | 102 |
| A.8. Overview of the settings of the chambers in supermodule XI installed in TRD sector 15. | 103 |
| A.9. Overview of the settings of the chambers in supermodule VIII installed in TRD sector 16. | 104 |
| A.10. Overview of the settings of the chambers in supermodule V installed in TRD sector 17. | 105 |

1. Introduction

How did the universe begin? History reveals that not just physicists were confronted with this fundamental question. It is interesting to know, that the origin of our present believe of a *big bang* was first laid out by the scientist and priest Georges Lemaître in 1927 [1]. Today, scientists from all over the world spend enormous efforts to put together the puzzle pieces of the observational evidence of the *Big Bang Theory*. The earliest evidence are several cosmological phenomena, for example the *Hubble-type expansion* [2], the detailed measurement of the *cosmic microwave background* [3] and the *apparent evolution of galaxies* [4]. Many nuclear physicists dedicate their research to the first instants of a second after the big bang. The *Large Hadron Collider* (LHC) at the *European Organization for Nuclear Research* (CERN) near Geneva is a powerful tool in nuclear and high energy particle physics to examine many unsolved phenomena. Among others, these are the search for the *Higgs Boson*, *supersymmetry*, *extra dimensions*, and *dark matter*. In addition, physicists at *A Large Ion Collider Experiment* (ALICE) [5] perform a dedicated research for the *Quark Gluon Plasma* (QGP) [6], a phase at extremely high temperatures, consisting of free quarks and gluons. It is the current understanding, that between 1 ps - 10 μ s after the big bang, this state of strongly interacting matter existed, containing the complete matter, anti-matter and energy of the universe, until it cooled and hadrons were formed. Generally, looking back onto a long history of heavy ion research, the ALICE experiment draws upon the highest collision energy ever achieved in a laboratory for its research. The LHC is designed to collide protons at an instantaneous luminosity of $10^{34} \text{ cm}^{-2}\text{s}^{-1}$ and a center-of-mass energy of $\sqrt{s} = 14 \text{ TeV}$, and lead ions at an instantaneous luminosity of $5 \times 10^{26} \text{ cm}^{-2}\text{s}^{-1}$ at a center-of-mass energy of $\sqrt{s_{NN}} = 5.5 \text{ TeV}$ per nucleon-nucleon pair. At present the LHC is operated at half of the design energy and will reach its design energy after a shutdown for machine consolidation in the years 2013 and 2014. A typical event display of a PbPb collision at $\sqrt{s_{NN}} = 2.76 \text{ TeV}$ recorded in November 2011 in the ALICE *Time Projection Chamber* (TPC) and *Inner Tracking System* (ITS) is shown in Fig. 1.1. Specifically for the purpose of characterizing the QGP, the ALICE experiment was equipped with several subsystems with outstanding capabilities of particle tracking and identification. Of these subsystems, the ALICE *Transition Radiation Detector* (TRD) [7] is the main electron detector. It provides electron identification capabilities for studies on light and heavy vector mesons, especially for momenta above 1 GeV/c. In this range the *pion rejection* through the mean energy loss in the TPC, described with the Bethe formula, is not sufficient. Above momenta of 3 GeV/c the TRD is designed to reject pions by a factor of up to 100. Other main physics goals of the TRD are the analysis of semi-leptonic decays of hadrons with open charm and open beauty and the analysis of jets with high transverse energy. For these analysis, the TRD aims to provide a physics trigger for high p_t electron pair selection with Υ mass, high- p_t J/Ψ and other event selection triggers for hard and rare probes of open charm and beauty.

For the separation of electrons and pions, the TRD uses *transition radiation*. For quality

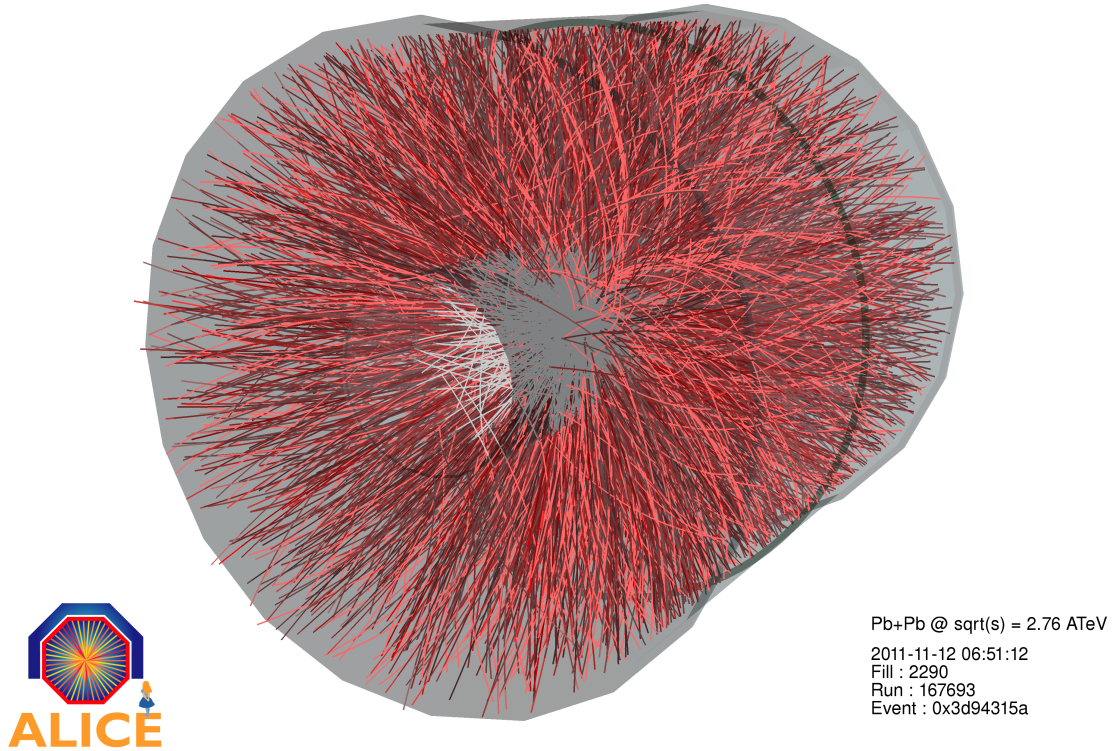


Figure 1.1.: Typical event from PbPb collisions at $\sqrt{s_{NN}} = 2.76$ ATeV, as seen by the ALICE Time Projection Chamber (red tracks) and Inner Tracking System (white tracks).

of electron identification the detector is subdivided into six layers of individual readout chambers, each consisting of a radiator, a multi-wire proportional chamber with a drift region and front-end electronics. Because of the high pad-granularity of the TRD readout chambers, the amplification factor (gain) of the multi-wire proportional chamber varies on pad level due to local imperfections in the geometry, such as a bump in the pad plane, pressure gradients within a chamber, or other phenomena causing gain variations. However, gain uniformity of all readout pads is essential for stable particle identification and triggering. In this thesis these relative gain variations are determined on the pad level for all installed chambers, using data recorded in dedicated runs with a radioactive Krypton source. The electron spectrum of the decay of metastable ^{83m}Kr by internal conversion is analyzed to improve the gain uniformity to better than 2 %. A change of 1 % in the gain corresponds to a change in pion suppression of 10 % or less [8], which meets the design requirements of the TRD. The obtained gain factors are then available for download into the front-end electronics of each readout chamber, and used for online gain corrections. A smaller part of this thesis addresses the alignment of all installed TRD readout chambers relative to the TPC. Strong mechanical constraints are imposed on the TRD design, however, mechanical tolerances during assembly of the individual detector components and

time driven deformations would restrict the tracking capabilities of the devices. To correct for deviations from the ideal geometry, the alignment of the detector elements relative to the TPC is accomplished with particle trajectories from pp collisions at $\sqrt{s} = 7$ TeV per nucleon.

This thesis is organized as follows: Chapter 2 gives a brief summary of the key theoretical elements. A more detailed introduction into the infrastructure at CERN, the LHC and the ALICE experiment is given in chapter 3. Chapter 4 contains a detailed explanation of the ALICE TRD. The concept of using the decay of ^{83m}Kr by internal conversion is explained in chapter 5. The actual experimental setup during the Krypton calibration and statistics on the recorded runs are presented in chapter 6. The analysis strategy and results of the gain calibration are described in chapter 7. Correlations between the gain and anode high voltage are studied and comparisons of the acquired gain maps to results from measurements during TRD chamber construction are presented. A description of the alignment procedure and results are given in chapter 8. A Summary and an outlook are presented in chapter 9.

2. Theoretical Background

2.1. Basic Constituents of Matter

In order to understand the physics goals of the ALICE experiment, the *Standard Model of Particle Physics* will be briefly summarized in this section. A small introduction on the *Quark Gluon Plasma* and its generation in heavy ion collision is given subsequently, to emphasize the necessity of the ALICE experiment as the dedicated heavy ion experiment at the Large Hadron Collider at CERN.

2.1.1. The Standard Model of Particle Physics

Increasing knowledge collected in detailed and high-precision experiments of the universe led to a set of building blocks of the matter around us, the so called Standard Model of Particle Physics, or briefly, the *Standard Model*. The Standard Model is one of the most successful theories in science, explaining the basic constituents of the universe and the forces between them. As visible in Fig. 2.1 there are three types of particles, quarks, leptons and gauge bosons. According to their mass, these are split up into three generations.

| | | Generation | | | |
|-------------------|---------|------------------------------|----------------------------|----------------------------|---------------------------|
| | | I | II | III | |
| mass → | | 2.49 MeV/c ² | 1.27 GeV/c ² | 172 GeV/c ² | 0 |
| electric charge → | | $\frac{2}{3}$ | $\frac{2}{3}$ | $\frac{2}{3}$ | 0 |
| flavor → | | u up | c charm | t top | γ photon |
| | Quarks | 5.05 MeV/c ² | 101 MeV/c ² | 4.19 GeV/c ² | 0 |
| | | $-\frac{1}{3}$ | $-\frac{1}{3}$ | $-\frac{1}{3}$ | 0 |
| | | d down | s strange | b bottom | g gluon |
| | Leptons | <2.4 eV/c ² | <0.19 MeV/c ² | <18.2 MeV/c ² | 91.2 GeV/c ² |
| | | 0 | 0 | 0 | 0 |
| | | ν_e electron neutrino | ν_μ muon neutrino | ν_τ tau neutrino | Z ⁰ Z boson |
| | | 511 keV/c ² | 106 MeV/c ² | 1.78 GeV/c ² | 80.4 GeV/c ² |
| | | -1 | -1 | -1 | ± 1 |
| | | e electron | μ muon | τ tau | W [±] W boson |
| | | | | | Gauge Bosons |

Figure 2.1.: Shown are the elementary particles of the Standard Model. Quarks (grey), leptons (green) and gauge bosons (red) are listed with their mass, charge, spin and name. This figure has been taken from [9].

All leptons carry spin $1/2$ and an additional quantum number, the so called lepton flavor. The muon (μ) and the tau (τ) are considered as heavy siblings of the electron, because they carry the same electric charge and spin, but have a larger mass. They can only be produced in high energy collisions or decays and rapidly decay into the stable electron. Additionally, there are three neutrino types, one for each flavor (ν_e, ν_μ and ν_τ). Quarks carry spin $1/2$ as well, and are ordered similarly: The lightest quarks are the up (u) and the down (d) quark, followed by the heavier strange (s) and charm (c) quark. The heaviest quarks are the bottom (b) and the top (t). The top-quark, with a mass of $172.9 \pm 1.5 \text{ GeV}/c^2$, was discovered in 1995 by the *CDF* [10] and *DØ* [11] collaborations at the *Tevatron collider* at *Fermilab*, because very high energies in particle collisions are necessary for its generation. In addition to their electric charge of either $-1/3e$ or $+2/3e$, all quarks carry a color charge of red, blue or green. For each of the particles previously mentioned (all fermions) there are anti-particles, having the same mass but opposite intrinsic quantum numbers. From this set of elementary particles in the Standard Model the complete structure of the visible (anti-)matter can be explained. However, due to *confinement*, quarks are never directly observed, and only found in hadrons. Besides the common nucleons, the particle zoo is dominated by a large number of hadrons, which is split up into two groups. The *Baryons*, such as the nucleons n and p , are made up of three quarks, whereas the *Mesons*, such as the π^0 - and η -meson, are built from a quark-antiquark pair. This basic principle of construction leads to the variety of observed particles and excited states at elevated energy levels. These states only differ in their mass and quantum properties.

Besides these elementary particles, the Standard Model concludes in three fundamental forces in nature. Gravitation is not considered, because of its relative weakness compared to the other forces. There are the twelve vector bosons mediating these three forces, namely the W^\pm -boson and the Z^0 -boson for the weak interaction, the massless photon γ for the electromagnetic interaction, and eight types of massless, color-charged gluons g for the strong interaction [12]. Whereas leptons only experience weak and electromagnetic interaction, quarks also have strong interactions. More detailed information can be found in [12].

Physics beyond the Standard Model

Despite the tremendous success of prediction and experimental evidence, the Standard Model leaves many questions in particle physics unanswered, i.e. the origin of mass of quarks and charged leptons, a question which may be explained by the introduction of the so called Higgs-Mechanism and the Higgs Boson [13][14]. Many other experimental observations, such as neutrino oscillations [15], matter-antimatter asymmetry [16] and dark matter and dark energy [17] are still open research topics to which the Standard Model does not deliver an adequate explanation.

2.1.2. The Quark-Gluon Plasma

Even though the theory of *quantum chromodynamics* (QCD), describing the strong interaction, evolved from a generalization of *quantum electrodynamics* (QED), there are crucial differences [6]. Whereas the mediating vector boson of QED, the photon, does not transfer charge, the gluons in QCD are not neutral in color and therefore lead to im-

portant characteristics of quark-gluon dynamics. On the one hand, at high energies and small distances, gluons and quarks only interact weakly because the interaction becomes small. This is due to *asymptotic freedom*, an aspect arising from the anti-screening of color charge. On the other hand, the interaction becomes strong at low energies and results in the *confinement of color*, thus quarks are never observed in isolation but are confined inside hadrons. However, at very small distances in a quark-anti-quark pair the coupling strength decreases and the state of a deconfined phase of matter, namely the *quark-gluon plasma* (QGP), is expected [18]. The subsequent formulation of QCD predicts a phase transition of the vacuum from a hadronic phase into this QGP phase. Calculations indicate a rapid crossover near the narrow temperature interval around a critical temperature of $T_C \sim 170 \text{ MeV}$. At large chemical potential μ_B and low temperatures, the model of nearly degenerate, interacting Fermi gases describes the properties of matter accurately. In the high-density phase, numerical calculations predict a remnant attractive interaction among quarks, leading to the state of a color superconducting phase, as shown in Fig. 2.2.

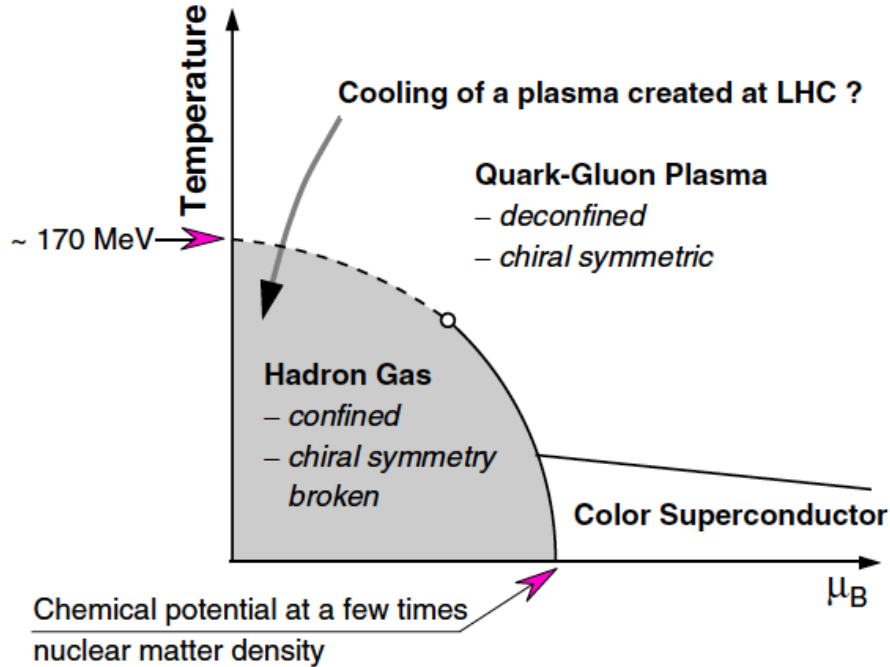


Figure 2.2.: The figure displays the QCD phase diagram. Solid lines show likely first-order transitions, whereas the dashed line implies a possible rapid transition. The open circle describes a second-order critical endpoint, which may be located closer to $\mu_B = 0$ in the interior of the QCD diagram. This figure has been taken from [5].

A first-order phase transition is expected at low temperatures and high densities. In the case that the first-order transition does not occur at $\mu_B \approx 0$ and $T_C \approx 170 \text{ MeV}$, the first-order transition has to end somewhere in a second-order critical endpoint in the interior of the QCD phase diagram. This point is indicated by the open circle in Fig. 2.2, but it may as well be located closer to the $\mu_B = 0$ axis. As symbolized by the black arrow, a transition of the QGP to a hadron gas via cooling of the plasma is expected at the LHC. More details can be found in [6].

2.1.3. QGP in Heavy Ion Collisions

As described above, QCD predicts a phase transition of strongly interacting matter into a state of deconfined quarks and gluons, the QGP. It is the aim of the studies of ultra-relativistic heavy ion collisions to analyze this strongly interacting matter under extreme conditions around a critical energy density $\epsilon_C = 0.6 \pm 0.3 \text{ GeV}/\text{fm}^3$ [19]. The time scale of collisions, for example in AuAu-collisions with $\sqrt{s_{NN}} = 200 \text{ GeV}$ at the *Relativistic Heavy Ion Collider* (RHIC), is typically of 10 fm/c, corresponding to a typical system size of 10 fm [6]. A schematic view of colliding gold-ions, which generate a quark-gluon plasma, is displayed in Fig. 2.3. Here, the Lorentz-contracted nuclei (a and b) generate the deconfined phase state (c and d) from quarks (white) and gluons (green). Prehadronic clusters (red) eventually hadronize (d-f) into pions (blue), kaons (yellow) and nucleons (magenta).

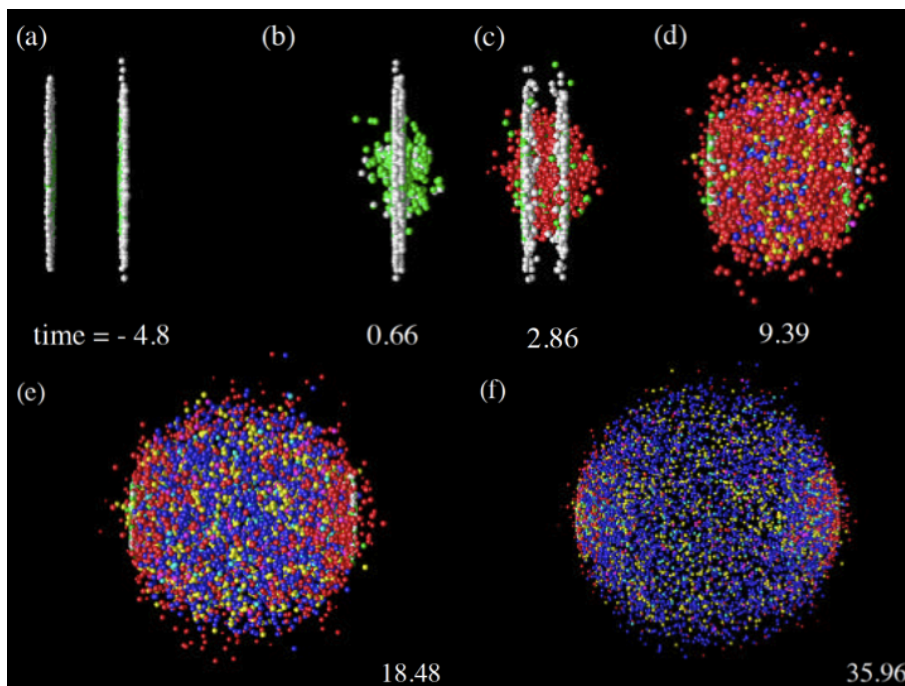


Figure 2.3.: Simulation of an AuAu-collision, which generates a QGP. The deconfined phase state of quarks (white) and gluons (green) is generated. The prehadronic clusters (red) then hadronize into pions (blue), kaons (yellow) and nucleons (magenta). The time is given in units of $3 \times 10^{-24} \text{ s}$. The figure has been taken from [20].

As the QGP expands and cools under emission of different radiation, for example gluon emission and electromagnetic radiation, it undergoes a phase transition to a hadron gas, which eventually dissolves into many color-white hadrons [6]. Detection of particles and radiation generated during this process enables the reconstruction of the initial formation of the QGP. This leads to extremely relevant experimental probes such as properties of the transverse momentum spectra of photons, dileptons and hadrons [19], or production rates of strangeness and charm from the QGP [6]. These measurements are comparable to studies of the early universe by analysis of remnants like the cosmic microwave background [3] and the abundance of chemical elements, among others.

2.2. Interactions of Particles and Matter

2.2.1. Energy Loss of charged Particles

In the following chapter the basic concepts of particle interactions in matter will be briefly introduced, as they ultimately lead to signal production, for example in the ALICE TRD (chapter 4.1). Here, particles generated at pp or PbPb collisions pass through a gaseous medium, ionize atoms along their path and thus deposit their energy. To understand these processes and to estimate the amount of energy such a particle deposits, the *Bethe Equation* will be explained. The energy loss of particles in the range of low and high energies will be described. Further on, as they are of significant importance for particle identification, the concepts of *Bremsstrahlung* and *Transition Radiation* will be discussed. Here the principle of *Cherenkov Radiation* should be mentioned as well, however, as it is not of tremendous importance for the ALICE TRD, no details are presented. Further information can be found here [12].

2.2.2. Bethe Equation

When a charged particle with the speed $\beta = v/c$ transverses a medium, it loses energy through single collisions with atoms of the medium. This results in ionization and atomic or collective excitation [21]. Beginning with the Rutherford differential cross section, Bethe used *Born Theory* to describe the single energy loss for bound electrons in matter, considering the bulk and atomic structure of the material [21]. However, the theory developed by Bethe was only valid to some energy, above which atomic effects are not important. Atomic effects at low particle energies and the density effect at high particle energies, as it was introduced by Enrico Fermi, had to be taken into account, too. The result is the famous *Bethe Equation* for the mean rate of energy loss in the region of $0.1 \leq \beta\gamma \leq 1000$ for low and intermediate Z-materials, for example Selenium (Z=34):

$$-\left\langle \frac{dE}{dx} \right\rangle = Kz^2 \frac{Z}{A} \frac{1}{\beta^2} \left[\frac{1}{2} \ln \frac{2m_e c^2 \beta^2 \gamma^2 T_{max}}{I^2} - \beta^2 - \frac{\delta(\beta\gamma)}{2} \right] \quad [21] \quad (2.1)$$

Here, $K/A = 4\pi N_A r_e^2 m_e c^2 / A$, where N_A is the *Avogadro constant*, r_e and m_e are the classical electron radius and the electron mass, and A is the atomic mass of the medium. Further on, z describes the number of charges in units of e , I is the mean excitation energy in eV, and T_{max} the maximum transferable energy to a single electron in a collision. $\delta(\beta\gamma)/2$ introduces the density effect correction at high particle energies. Usually, with increasing particle energies, the electric field flattens and extends, increasing equation 2.1 as $\ln(\beta\gamma)$. However the density effect accounts for a limited field extension due to polarization of the medium and therefore reduces the slope, as visible in Fig. 2.4, in the region of $\beta\gamma \approx 10 - 100$. The remaining relativistic rise of equation 2.1 is caused by large energy transfers to only a few electrons (because $T_{max} \sim \beta^2 \gamma^2$). It has to be mentioned that generally the Bethe equation returns too high values, because it describes the mean dE/dx . Usually, significantly lower values for the most probable energy loss are observed.

For particle with very high kinetic energies, radiative processes are of significant importance in understanding the particle energy loss. These are typically characterized by small cross

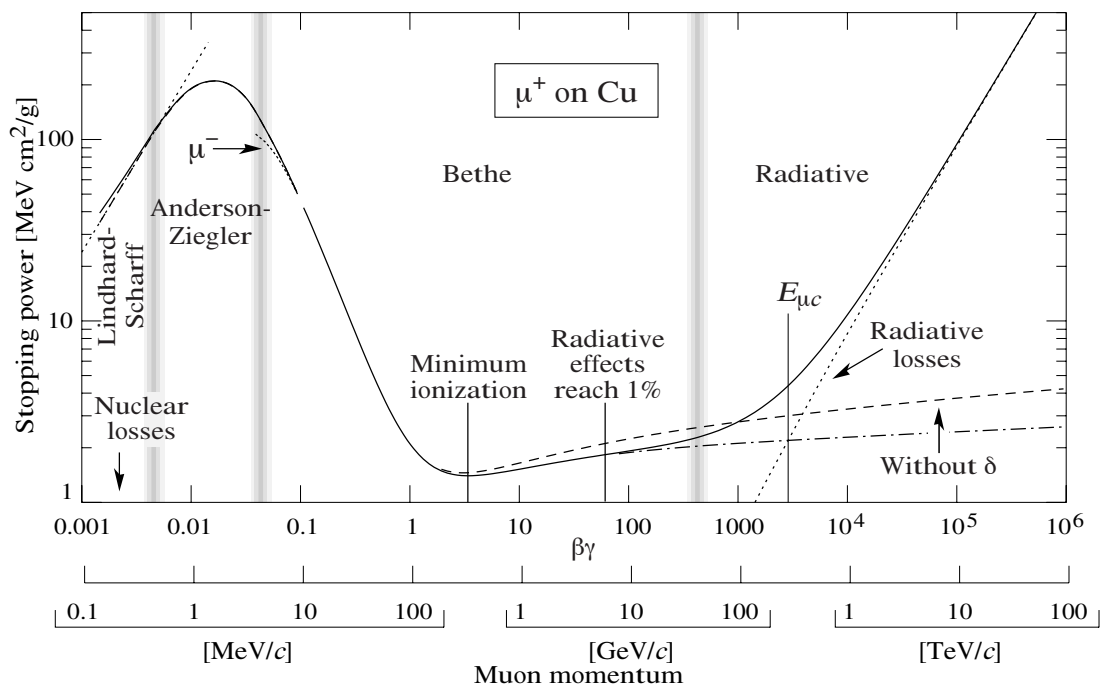


Figure 2.4.: Mean rate of energy loss for positive muons in copper. Solid lines represent the total stopping power. This figure has been taken from [21].

sections, hard momentum spectra and large energy fluctuations and can generate electromagnetic or hadronic showers [21]. Contributors are pair production, Bremsstrahlung and photonuclear interactions.

2.2.3. Bremsstrahlung

For highly energetic charged particles, particularly electrons with their low mass, energy loss via Bremsstrahlung is large. Above the so-called *critical energy* E_c charged particles lose more energy via photon emission than via ionization, due to the de-acceleration of the charged particle in the vicinity of an atomic nuclei. E_c is estimated via [21]

$$E_c = \frac{610 \text{ MeV}}{Z + 1.24} \text{ (solids and liquids)} \text{ and } E_c = \frac{710 \text{ MeV}}{Z + 0.92} \text{ (gases)}. \quad (2.2)$$

The critical energy is visible in Fig. 2.5, where fractional energy loss through ionization equals the amount of energy lost through Bremsstrahlung.

Electron and positron scattering at low energies is considered as ionization, when the energy loss per collision is below 0.255 MeV. If it is above, it is assumed to be Møller (Bhabha) scattering ($e^+e^- \rightarrow e^+e^-$) [21]. The energy loss by Bremsstrahlung is calculated via

$$-\frac{dE}{dx} \approx 4\alpha \cdot N_A \cdot \frac{Z^2}{A} z^2 \left(\frac{1}{4\pi\epsilon_0} \cdot \frac{e^2}{mc^2} \right)^2 \cdot E \ln \frac{183}{Z^{1/3}} [22], \quad (2.3)$$

where $\alpha = 1/137$ denotes the *fine structure constant*. Other variables are the same as for equation 2.1. This energy loss is proportional to the particles energy as well as inversely

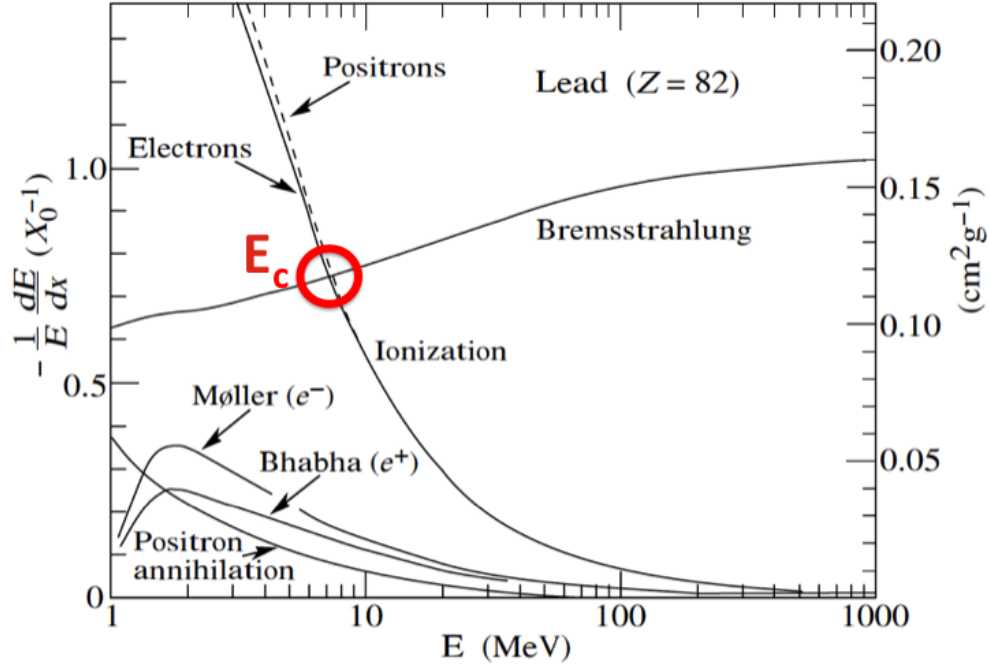


Figure 2.5.: Fractional energy loss per radiation length in lead for electrons or positrons, as a function of their energy. The critical energy E_c describes the intersection of the ionization curve and the Bremsstrahlung curve. This figure has been taken from [21].

proportional to its squared mass, and thus has a large contribution to the complete energy loss of low mass particles, such as electrons. For electrons, equation 2.3 can be re-written with the *radiation length* X_0 as follows:

$$-\frac{dE}{dx} = \frac{E}{X_0} \quad [22] \quad (2.4)$$

where $X_0^{-1} \propto Z^2$. The radiation length describes the length, after which a particle energy dropped to $1/e$ of its initial value due to the emission of Bremsstrahlung radiation.

2.2.4. Transition Radiation

If a relativistic charged particle traverses the boundary between two media with different dielectric constants, *transition radiation* [22] is emitted. Its production can be explained with the model of mirror charge: Moving towards a boundary, the charged particle forms, together with its mirror charge, an electric dipole, as shown in Fig. 2.6.

As the particle moves very fast, the field strength varies in time and vanishes when the particle enters the medium, causing the emission of electromagnetic radiation at an angle of $\Theta \propto 1/\gamma$, where γ is the *Lorentz factor*. The angular dependency is a results of the continuous change of the electric displacement $\vec{D} = \epsilon\epsilon_0 \vec{E}$, while the field strength is

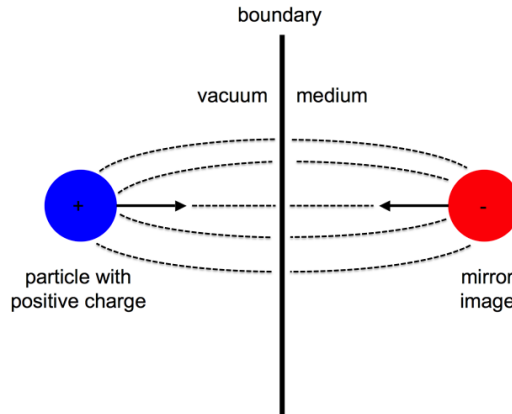


Figure 2.6.: Schematic drawing of the production of transition radiation, using the model of mirror charge. Electric field lines are indicated by the dotted lines. The figure was inspired by [22].

constant. The number of photons emitted with energy $\hbar\omega$ larger than some threshold $\hbar\omega_0$ is

$$N_\gamma(\hbar\omega > \hbar\omega_0) \approx \frac{\alpha z^2}{\pi} \left[\left(\ln \frac{\gamma \hbar\omega_p}{\bar{\omega}_0} - 1 \right)^2 + \frac{\pi^2}{12} \right] \quad [22], \quad (2.5)$$

where $\hbar\omega_p$ is the *plasma energy*, which is estimated with the *plasma frequency* ω_p . The plasma frequency defines a threshold specific to a material, below which irradiated electromagnetic waves are reflected. The total energy emitted at a single boundary, e.g. vacuum to medium(ϵ), is given by

$$S = \frac{1}{3} \alpha z^2 \hbar\omega_p \gamma \quad \text{with} \quad \hbar\omega_p = \sqrt{4\pi N_e r_e^3 m_e c^2} / \alpha \quad [22]. \quad (2.6)$$

Here, N_e describes the electron density. Because the number of emitted photons N_γ is low, usually several layers of radiator material are used in detectors. The specific setup of the radiator used in the ALICE TRD is described in chapter 4.2.1.

2.3. Amplification of Ionization

As visible in chapter 4.1 an essential part of the ALICE transition radiation detector is a multi-wire proportional chamber. The physics of amplification of ionization is of significant importance to fully comprehend the functionality of such a device. In the following the basic physics principles regarding the amplification of ionization, the gain, will be explained for a proportional wire, the key element of the chamber. Further on, the dependencies of the gain on the high voltage setting, the pressure within the gas system and position within a multi-wire proportional chamber will be explained.

2.3.1. Gain of the Proportional Wire

Since the beginning of the development of proportional counters in 1948 [23], a proportional wire is most likely the simplest and best-studied tool to understand particle detection and signal amplification. Operated at high voltages and connected to further sensitive electronic equipment it is able to detect even single electrons originating from the ionization of a particle transversing a gaseous medium. The strong advantage of such a proportional counter is the high amplification factor of the signal.

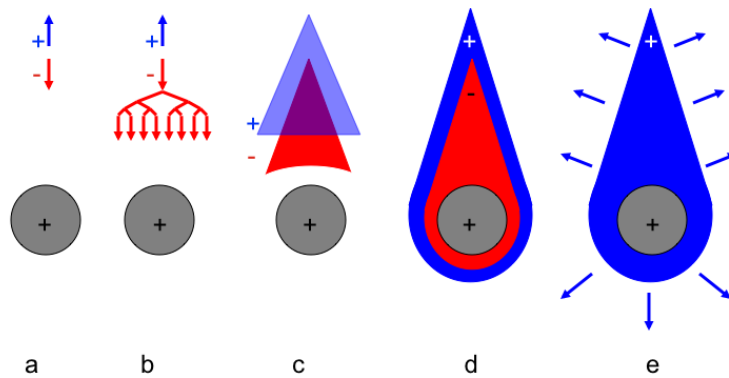


Figure 2.7.: Evolution of the avalanche for ions (blue) and electrons (red) near a proportional anode wire. An ionization electron drifts towards the wire (a). In the vicinity of a high electric field near the wire, the electron creates secondary ionization and avalanches form (b). Electron- and ion-cloud are formed (c) until the electrons reach the wire (d) and the ion cloud disperses (e). The figure was inspired by [24].

Fig. 2.7 illustrates the evolution of the signal near a proportional wire [24]. Once created by ionization through an energetic particle passing the gas inside the counter (chapter 2.2.1), the primary ionization electrons drift towards the anode wire (a). Near the surface of a thin anode wire, the strength of the electric field at the electrons position is large enough for the electron to acquire sufficient energy between the collisions with the gas molecules to further ionize more atoms. An avalanche is produced by secondary ionization and continuously moves towards the anode wire (b). These electron- and ion-clouds drift away from each other (c) until the electrons reach the wire (d) and the ion-cloud radially disperses (e). For the high voltages applied, a magnetic field, generally strongly affecting the path of the electrons, does not prevent the trajectory to end on the wire [23]. As a consequence the induced final signal is proportional to the number of electrons collected and therefore to the number of primary particles.

The multiplication of ionization is qualitatively described by the first *Townsend coefficient* α , which relates the number of secondary ionization electrons produced per path length ds to the number of primary ionization electrons:

$$dN = N\alpha ds \quad (2.7)$$

α is determined by the excitation and ionization cross sections of the secondary ionization electrons and must be found experimentally for each gas composition. For the ALICE TRD typically 275 electrons per cm are produced [7] in a $Xe - CO_2$ [85-15] gas mixture and anode voltage of 1530 V. Further on, the applied high voltage and the density of the gas mixture enter into the measurement of the Townsend coefficient. For higher electric fields the ionization cross section of the primary electrons is increased, whereas α increases proportionally with the gas density ρ , because the linear dimensions in the gas scale with the mean free collision length. The total amplification factor of the wire can then be found via integration over the path from the origin of the avalanche R to the surface of the wire at radius r . The path may also be described by a change of the electric field:

$$N/N_0 = \exp \int_R^r \alpha(s) ds = \exp \int_{E_R}^{E(r)} \frac{\alpha(E)}{dE/s} dE. \quad (2.8)$$

Here, N and N_0 describe the initial and final number of ionization electrons. The electric field close to the wire may be expressed through charge per unit length λ of the wire, if the wire radius r is small compared to the distance between the electrodes

$$E(r) = \frac{\lambda}{2\pi\epsilon_0 r}, \text{ with } \epsilon_0 = 8.85 \times 10^{-12} \text{ As/(Vm)}, \quad (2.9)$$

which leads to

$$G = N/N_0 = \exp \int_{E_R}^{E(r)} \frac{\lambda\alpha(E)}{2\pi\epsilon_0 E^2} dE. \quad (2.10)$$

$G = N/N_0$ is called gas amplification factor or gain [23]. For the ALICE TRD the typical gain is of the order of $G = 3 \cdot 10^3$ in a $Xe - CO_2$ [85-15] gas mixture and anode voltage of 1530 V (see chapter 7.9 for more details).

2.3.2. The Role of Photons and the Penning Effect

Produced by the processes of excitation and ionization, a small but not negligible fraction of generated photons is energetic enough to further ionize atoms. In case the average range of these photons is larger than the longitudinal size of the avalanche, more avalanches may be produced at a large range. These essentially lead to a break down of the counter. Originating from avalanches, photons which reach the conducting surface cause a similar effect, because they free electrons from the material via the photoelectric effect. To prevent any interferences or damages caused by this effect, an organic *quench gas* is added to the gas mixture, for example CO_2 in case of the ALICE TRD. With their many degrees of freedom, organic molecules have large photo absorption coefficients over a large variety of wavelengths, larger than that of noble gases, which are typically used in particle detector

applications. The quench gas reduces the average possibility that a long-range photon further ionizes the gas and thus increases the gain. A measure on how good the quench gas works is the *Penning Transfer*. It scales up the Townsend coefficients according to the energy transfer rate resulting from the ionization of gas species because of collisions with other excited, metastable gas states (*Penning Effect*). The *Penning Fraction*, namely the amount of a specific excited species which further ionizes the gas, normalized to its abundance, is not dependent on the electric field or the high voltage, but only on the noble and the quench gas of the mixture. More details and numbers can be found in [25].

2.3.3. Local Variations of the Gain

In the following, variations of the gain caused by different effects will be reviewed [23].

Gain Variations with Changes of the Gas Density

Because typical field strength for heavy noble gases are in the range of 10^2 and 10^3 [V/cmTorr] near the surface of a proportional wire, it is a reasonable assumption that the Townsend coefficient is proportional to the electric field E , thus $\alpha = \beta E$. Further considering that each generation of the avalanche of secondary ionization electrons doubles the total number of electrons, β is the inverse average potential required to produce one electron in the avalanche, multiplied by $\ln 2$ [23]. Thus, the gain is described by the formula

$$\ln G = \frac{\ln 2}{\Delta V} \frac{\lambda}{2\pi\epsilon_0} \ln \frac{\lambda}{2\pi\epsilon_0 a E_{min}} \quad [23] \quad (2.11)$$

Here, a is the distance between two potentials, whereas E_{min} describes the minimal electric field necessary for ionization at a distance s_{min} . λ describes the charge per unit length. Using the proportionality of the electric field E_{min} to the gas density ρ ,

$$E_{min}(\rho) = E_{min}(\rho_0) \frac{\rho}{\rho_0} \quad [23] \quad (2.12)$$

a correlation between the change of gain and the change of gas density, is derived:

$$\frac{dG}{G} = - \frac{\lambda \ln 2}{\Delta V 2\pi\epsilon_0} \frac{d\rho}{\rho} \quad [23]. \quad (2.13)$$

Further the gain varies with the local charge density of the wire, λ . Geometrical imperfections or other effects such as high voltage fluctuations or space charge near the wire eventually lead to relative changes $d\lambda/\lambda$, modifying the gain as following:

$$\frac{dG}{G} = \left(\ln G + \frac{\lambda \ln 2}{\Delta V 2\pi\epsilon_0} \right) \frac{d\lambda}{\lambda} \quad [23]. \quad (2.14)$$

Gain Variations near the Edges of a Wire Chamber

Dependent on the exact geometry of a wire chamber, the gain is significantly lower near the edges of such a chamber, because the charge density on the wire surface is not as uniform as centrally within the chamber [23]. Thus a drop of gain to zero is observed at the sides, in a range comparable to the distance between the anode wire and the cathode readout plane.

Local Variations of the Gain due to Mechanical Imperfections

Small deviations from an ideal geometry in the construction of a wire chamber effect the gain and are omnipresent, as they are permanently connected to a chamber and its mechanical tolerances. Especially the effect of a change of distance between the sense-wire grid and the readout plane of a chamber is a common source for gain fluctuations. In order to fully understand the consequence of geometrical imperfections not only a single sense-wire but surrounding wires and electrodes need to be considered. As these variations are strongly dependent on the exact chamber geometry, a TPC example geometry, shown in Fig. 2.8, will be used for further explanations. In this example, assuming the pad plane is grounded, there are four independent potentials, V_s (sense-wires), V_z (zero grid wires), V_f (field wires) and V_p (high voltage plane). Here, S_1 and S_2 describe the wire distance of the field wire grid and the zero grid wires, and Z_1 , Z_2 , and Z_3 describe the distance between the pad plane and the field wire grid, the zero grid wires, and the high voltage plane respectively.

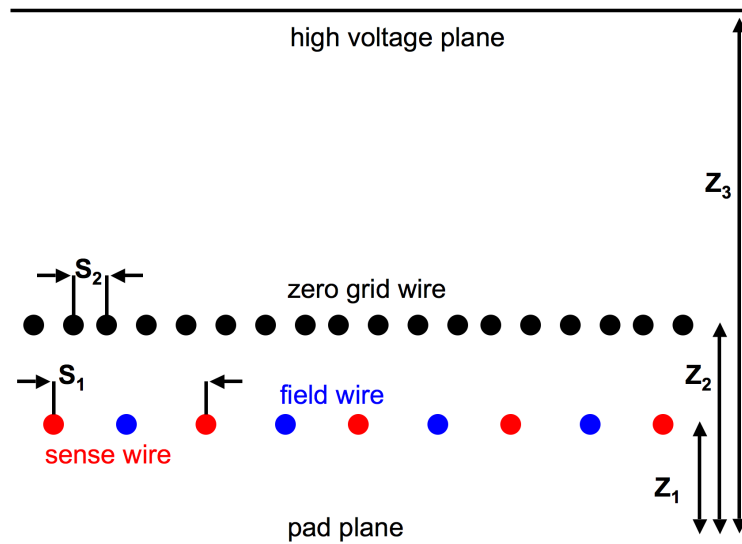


Figure 2.8.: Example of a TPC geometry [23].

The potential of each grid is computed via the sum of the fraction of the charges induced on each grid, expressed via their surface charge densities σ_s , σ_z , σ_f , and σ_p divided by their respective pitch. These relations are formulated as follows:

$$V = \begin{pmatrix} V_s \\ V_f \\ V_z \\ V_p \end{pmatrix} = A\sigma = A \begin{pmatrix} \sigma_s \\ \sigma_f \\ \sigma_z \\ \sigma_p \end{pmatrix} \quad [23], \quad (2.15)$$

where A is the matrix of the potential coefficients. In typical operating conditions of a TPC, the electric field in the drift region is much smaller than the field in the amplification region. Thus σ_p can be neglected, because the induced charge on the high voltage plane is approximated via

$$\sigma_p = \epsilon_0 \frac{V_p - V_z}{z_3 - z_2} \quad [23]. \quad (2.16)$$

Subsequently, A is reduced to a 3×3 matrix:

$$A = \frac{1}{\epsilon_0} \begin{pmatrix} z_1 - \frac{s_1}{2\pi} \ln \frac{2\pi r_s}{s_1} & z_1 - \frac{s_1}{2\pi} \ln 2 & z_1 \\ z_1 - \frac{s_1}{2\pi} \ln 2 & z_1 - \frac{s_1}{2\pi} \ln \frac{2\pi r_f}{s_1} & z_1 \\ z_1 & z_1 & z_2 - \frac{s_2}{2\pi} \ln \frac{2\pi r_z}{s_2} \end{pmatrix} \quad [23]. \quad (2.17)$$

Changing the geometry varies the surface charge density and therefore the matrix. For fixed values of V,

$$Ad\sigma = -dA\sigma \quad [23] \quad (2.18)$$

is derived and returns

$$d\sigma = -A^{-1}dA\sigma \quad [23]. \quad (2.19)$$

Displacements of the pad plane lead to a change of σ_z , resulting with equation 2.19 in

$$d\sigma = \frac{dz}{\epsilon_0} A^{-1} \begin{pmatrix} \sigma_s + \sigma_f + \sigma_z \\ \sigma_s + \sigma_f + \sigma_z \\ \sigma_s + \sigma_f + \sigma_z \end{pmatrix} \quad [23]. \quad (2.20)$$

Similar calculations can be done for differences caused by a change in the sense-wire radius r_s , resulting in:

$$d\sigma = -\frac{s_1}{2\pi\epsilon_0} \frac{dr_s}{r_s} A^{-1} \begin{pmatrix} \sigma_s \\ 0 \\ 0 \end{pmatrix} \quad [23]. \quad (2.21)$$

Considering the design of the ALICE TRD (chapter 4.1) and the Diethorn parameter $\Delta V=40$ V for the gas mixture Xe-CO₂ [85-15], the relation between gain and local relative charge-density variation is calculated with equation 2.14:

$$\frac{dG}{G} = 14.19 \frac{d\sigma_s}{\sigma_s}. \quad (2.22)$$

Thus the gain variations caused by variation of the sense-wire diameter or by a bump in the cathode pad plane are estimated. The results are shown in table 2.1.

| Imperfection | dG/G |
|--------------------------------------|-------------------------------------|
| Bump on the pad plane | $0.83\Delta z(1+\sigma_F/\sigma_s)$ |
| Variation of the sense wire diameter | $2.6\Delta r/r$ |

Table 2.1.: Gain variation of the ALICE TRD readout chamber caused by mechanical imperfections in the geometry. A gain of 3500 is assumed, shown displacements are in mm.

More details and further example calculations for a time projection chamber can be found in [23].

Gain Drop due to Space Charge

As already described in Fig. 2.7, the cloud of positive ions radially drifts away from the wire while the electrons are collected. These ions move towards the cathodes with a relatively low speed, because they have a low mobility (μ) of approximately 10^5 cm/s. Thus it takes a few microseconds until they drift to the nearest cathode, a few millimeters away. For large charge densities caused by these ions, or for initial particle frequencies higher than values corresponding to the drift time, stationary space charge effects are seen in the chamber. These reduce the electric field in the vicinity of the wire. To calculate the space charge density ρ , a small area A_1 of the wire surface with electric field E_1 is considered, emitting positive charged (q) ions at a rate $\nu = \text{const}$. With the speed of $v = \mu E_1$ the charge $Q_1 = q\nu\Delta t$ moves within the time Δt into the volume $V_1 = A_1 v \Delta t$. The charge density within the vicinity of the wire is then estimated by $\rho_1 = Q_1/V_1 = q\nu/\mu E_1 A_1$. Further, the ions continuously move away from the wire, entering the equipotential area A_2 with field E_2 , resulting in a charge density of $\rho_2 = q\nu/\mu E_2 A_2$. Applying *Gauss Law*, the result is $E_2 A_2 - E_1 A_1 = Q/\epsilon_0$, with Q as the total charge between A_1 and A_2 . However, Q may be neglected because it is negligible compared to the electric field of the wire. Then, as first order approximation, the charge density is constant along its path at any distance from the wire:

$$E_1 A_1 = E_2 A_2 \quad [23] \quad (2.23)$$

or

$$\rho_1 = \rho_2 = \rho = \frac{qR}{\mu E_1 2a\pi} \quad [23], \quad (2.24)$$

for a wire with radius a , surface field E_1 and charge deposit q at rate R . For a wire chamber with a wire grid of pitch s and potential V_0 , positioned centrally between two cathode planes at distance h , the electric field on the surface of the wire is $E_1 = V_0/(a \cdot \log \frac{r_c}{a})$. r_c is a

length with similar magnitude as s or h . With a particle flux $\Phi = R/s$, the uniform charge density is given with

$$\rho = \frac{sq\Phi \ln \frac{r_c}{a}}{2\pi\mu V_0} \quad [23] \quad (2.25)$$

Neglecting the wires, this causes an electric field of $E(z) = \rho z/\epsilon_0$, giving a potential difference of

$$\Delta V = \int_0^h E(z) dz = \frac{h^2}{2\epsilon_0} \rho = \frac{sh^2 q\Phi \ln \frac{r_c}{a}}{4\pi\epsilon_0\mu V_0} \quad [23]. \quad (2.26)$$

Statistical Fluctuation of the Gain

In case a wire chamber is set to proportional mode, the number of electrons in the avalanche is proportional to the number of initial electrons. In this section, the random fluctuation of the multiplication process of secondary ionizing electrons will be analyzed. For this purpose it is assumed that each electron produces an avalanche, independent of the surrounding electrons. The probability distribution of N ions in the avalanche is equal to the sum of the probability distributions $P(n)$ of n electrons in the independent avalanches. Considering a large number k of initial electrons, the central-limit theorem of statistics returns

$$N = n_1 + n_2 + n_3 + \dots + n_{k-1} + n_k \quad [23] \quad (2.27)$$

with each n_i having the same distribution function $P(n)$. In case of $k \rightarrow \infty$, $F(N)$ is of Gaussian shape

$$F(N) = \frac{1}{S\sqrt{2\pi}} \exp[-(N - \bar{N})^2/2S^2] \quad [23] \quad (2.28)$$

with $\bar{N} = k\bar{n}$ and $S^2 = k\sigma^2$, where \bar{n} is the mean of $P(n)$ and the σ^2 the variance. As visible in equation 2.28, the probability distribution $P(n)$ does not have to be known a priori. These statistical fluctuations are most likely caused by impurities of the gas mixture and other chemical reactions connected to the formation of avalanches.

Summary

The amplification of primary ionizing particles is strongly dependent on the exact geometry of the built detector. Clearly, local imperfections in the geometry of the chambers have the largest impact on gain variations. For example, considering table 2.1, a small bump on the pad plane of $\Delta z = 0.1$ mm would already lead to gain variation of >8.3 %. In case the sense wire diameter shows slight imperfection of the order of 1 %, for example because of ageing effects, the gain shows variations of the order of 2.6 %. Both observations are explained by the strong dependence of the gain on relative charge-density variations of the sense-wires. In addition, near the support structure of a readout chamber, the gain drops to zero values, because of inhomogeneities of the electric field.

As shown in chapter 7.5.5, the dependence of the gain on the gas density is not as big as in equation 2.22. However, as the atmospheric pressure permanently changes, these gain variations must be closely monitored and, if necessary, the high voltage adjusted in

order to keep a constant gain during measurements. Compared to the just mentioned dependencies of the gain, gain variations due to space charge effects are expected to be reasonably small, as long as the chamber dimension are kept at a minimal level, and the chamber is not irradiated by too high particle fluxes. Typically, wire chambers are used in particle experiments because of their high amplification factors, thus no strong gain variations due to statistical fluctuations are expected.

3. CERN and the LHC

Established in 1954 the *European Organization for Nuclear Research*, CERN, dedicated itself to provide complete infrastructure and accelerators for high-energy physics research. Located near Geneva on the French border, the laboratory can look back to many significant scientific achievements, such as the discovery of *neutral weak currents* in the *Gargamelle Bubble Chamber* in 1973, the discovery of the *W and Z bosons* in 1983, the first anti-hydrogen production in 1995, or the discovery of *direct CP-violation* in 1999, only to name a few. In the following, the current infrastructure will be briefly summarized to give a basis for a description of the ongoing main experiments carried out at the *Large Hadron Collider*. Special emphasis will be given on the ALICE detector.

3.1. The Large Hadron Collider

The *Large Hadron Collider*, known as the largest machine of the world and highest-energy particle accelerator, began its operation on the 10th of September 2008. Since 1984, the official starting point of research and development on the LHC, the accelerator was designed to collide opposing particle beams of protons at an energy of 7 TeV per beam particle, or lead nuclei at 2.76 TeV per nucleon. The old tunnel of the *Large Electron Positron Collider*, about 27 km in circumference and up to 110 m below surface, was used to install thousands of superconducting magnets, necessary to circulate the accelerated particles at a speed of 99.99 % of the speed of light and essentially collide them in four interaction points at a record design luminosity of up to $10^{34} \text{ cm}^{-2}\text{s}^{-1}$ for pp collisions. To achieve these high energies, several pre-accelerators are necessary to feed the particles into the machine, as can be seen in Fig. 3.1.

Lead ions are bunched and accelerated in an radio frequency quadrupole system after their production in an electron cyclotron. The lead ions are stripped and selected via the charge state Pb^{27+} until they are fed into a linear accelerator, LINAC3. Here they reach an energy of 4.2 MeV/nucleon. Further they are stripped with a carbon foil and the Pb^{54+} -state is selected in a filter line, until the ions reach an energy of 72 MeV/nucleon in a low energy ion ring (LEIR). After acceleration to 5.9 GeV/nucleon in the *Proton Synchrotron* (PS) the particles reach the *Super Proton Synchrotron* (SPS), where they are accelerated to 176 GeV/nucleon until they eventually are transferred into the LHC. Protons are created in a 90 kV duoplasmatron proton-source and undergo similar stages as the ions. Instead of the accelerating stages of the LINAC3 and LEIR, they pass the linear accelerator LINAC2 and the *Proton Synchrotron Booster* (PSB) before they are accelerated in the PS and SPS. In the LHC they have a final energy of 7 TeV per particle.

The four major experiments, also visible in Fig. 3.1, are ATLAS, ALICE, CMS and LHCb:

- **A Toroidal LHC ApparatuS** (ATLAS) [26]: The 2900 person-strong collaboration sustains one of the two general purpose experiments. Besides the search for evidence

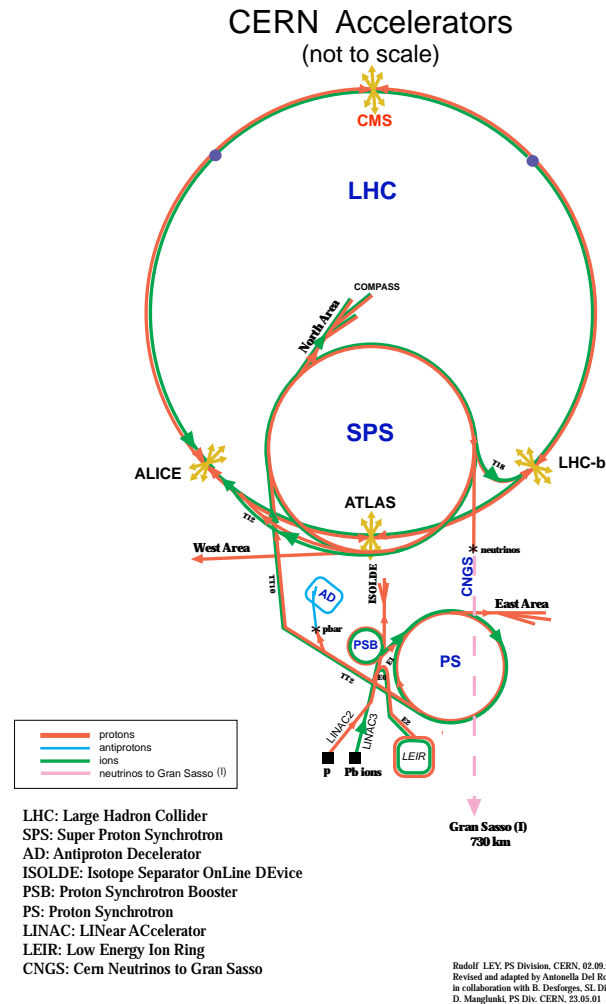


Figure 3.1.: The accelerator complex at CERN. Different particle species are indicated by different colors. Visible are the stages of acceleration for protons, antiprotons, ions and neutrinos. Protons and ions respectively are collided in the LHC at the interaction points of ATLAS, ALICE, CMS and LHCb. This figure has been taken from [27].

for physics beyond the Standard Model, ATLAS is looking for the *Higgs boson*, *extra dimensions* and *dark matter* candidates. It consists of several subdetectors laid out for momentum measurements, energy measurements and identifications of the produced particles. It also has an extremely strong superconducting magnet with

a field strength of $B = 2$ T in use.

- **Compact Muon Solenoid (CMS)** [28]: The CMS collaboration dedicated itself to the same scientific goals as ATLAS, however using different technical solutions. CMS is laid out specifically for the detection of muons, and thus consists of 1400 muon chambers. The detector is designed inside and around a huge solenoidal magnet, producing a magnetic field of 4 T. This large magnetic field allows the measurement of muons with very high momenta. About 2000 scientists are part of the collaboration.
- **Large Hadron Collider beauty (LHCb)** [29]: The 650 scientists of the collaboration mainly investigate the differences between matter and antimatter with studies of the b – quark. For this purpose the detector was constructed as a single arm forward spectrometer.
- **A Large Ion Collider Experiment (ALICE)** [5]: The following section 3.2 will be completely devoted to this experiment, as it hosts the ALICE TRD, the detector that was calibrated within this thesis.

3.2. The ALICE Detector

Scientists from 116 institutes from 33 nations work for the ALICE experiment [5]. As the dedicated heavy ion experiment at the LHC, it was designed to study heavy ion collisions at center-of-mass energies of up to 5.5 TeV per nucleon pair, and optimized to analyze the quark-gluon plasma (see chapter 2.1.2). The experiment consists of two major parts, the *central barrel* and the *muon spectrometer*. The latter, also called *Muon Arm*, covers a pseudorapidity range of $-2.5 \leq \eta \leq -4.0$ and consists of an own dipole magnet for charge separation and momentum reconstruction. The Muon Arm also hosts several subsystems, such as tracking and trigger chambers and muon filters. It has an invariant mass resolution of the order of 70 MeV in the J/Ψ region and about 100 MeV in the Υ region. The dipole produces an integrated field of 3 Tm. Only muons coming from the interaction vertex or hadronic decays can pass the front absorber, and are then bent by the magnetic field surrounding the tracking system - a set of 10 cathode pad/strip chambers arranged in 5 stations of 2 chambers each. These chambers have a spatial resolution better than 100 mm. Essentially a trigger system selects the heavy quark resonance decays via the transverse momentum (p_t) of the two unlike sign muons.

An overview of the subsystems installed in the ALICE experiment is shown in Fig. 3.2, where the central barrel detectors are housed in the L3 magnet. Hadrons, electrons and photons are identified and measured in the central rapidity region of $-0.9 \leq \eta \leq 0.9$. The L3 magnet can provide a magnetic field of up to 0.5 T. The main subsystems are the *Inner Tracking System* (ITS), a state of the art *Time Projection Chamber* (TPC), a *Transition Radiation Detector* (TRD) and a *Time Of Flight* array (TOF). Two single arm detectors are placed close to mid-rapidity, namely an array of *Ring-Imaging Cherenkov Counters* (HMPID) for hadron identification and an array of crystals (PHOS) for photon detection. In addition an *Electro-Magnetic Calorimeter* (EMCAL) for studies on jet-quenching was installed.

Further elements of the central detection system are located at large rapidities. For the measurement of charged particles and triggering, the *Forward Multiplicity Detector* (FMD),

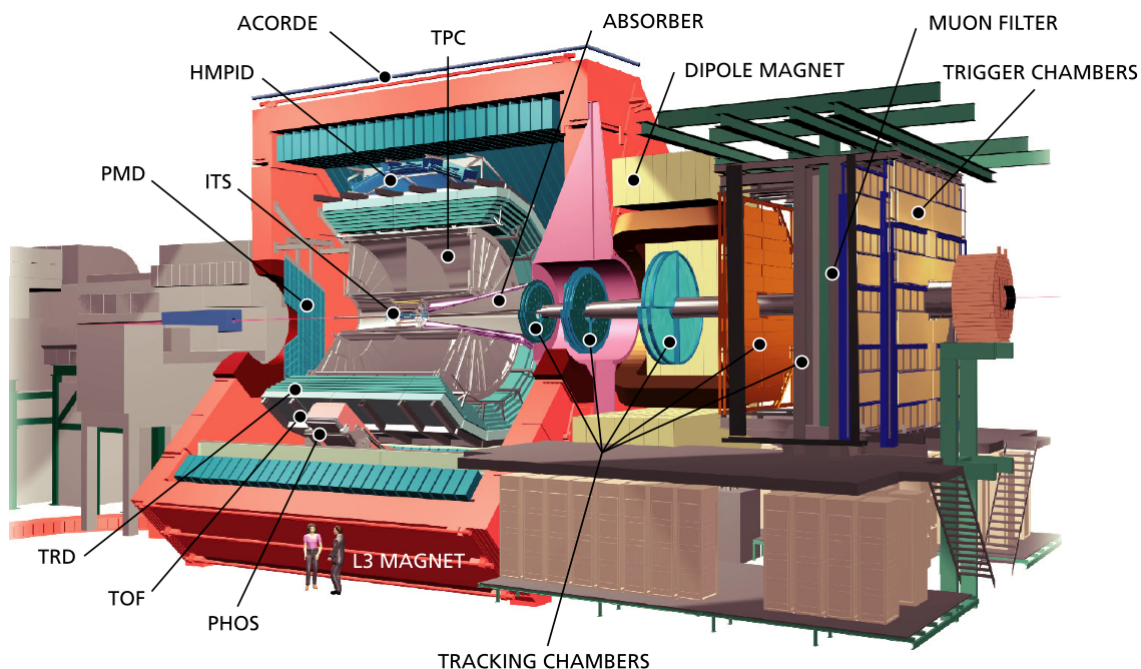


Figure 3.2.: Schematic drawing of the ALICE detector and its subsystems. This figure has been taken from [5].

and the $V0$ and $D0$ detectors cover a range of $-3.4 \leq \eta \leq -5.1$. At large rapidities of $-2.3 \leq \eta \leq -3.5$ a *Photon Multiplicity Detector* (PMD) is installed, whereas *Zero-Degree Calorimeters* (ZDCs) provide coverage of the beam rapidity, 116.1 m away from the collision point.

- **Inner Tracking System (ITS)** [30]: The ITS is designed to determine the primary vertex and the secondary vertices for the reconstruction of charm, beauty and hyperon decays. Additionally, it serves as particle identification, tracks low-momentum particles and improves the momentum and angle measurements of the TPC. The ITS consists of a silicon pixel detector, a silicon drift detector and a silicon strip detector, each arranged in 2 layers around the interaction point. Because of the extremely high track density of up to 90 tracks per square centimeter, the ITS detectors have a very high granularity and a spatial resolution of a few tens of μm . They also are radiation hard because of the harsh environment close to the interaction point.
- **Time Projection Chamber (TPC)** [31]: Of the detectors in the central barrel, the TPC has the main charged particle tracking capabilities and momentum determination. In addition, particle identification is performed via the measurement of the specific energy loss dE/dx . It has an overall length of 5 m and has complete azimuthal coverage. The cylindrical field cage inhibits a gas volume of 88 m^3 , and is divided by a central electrode into two drift regions, each with a uniform electrostatic field of 400 V/cm . The TPC is operated with a gas mixture of $\text{Ne} - \text{CO}_2 - \text{N}$ [85-10-5], achieving a maximum drift time of $88 \mu\text{s}$. It is designed to provide charged particle momentum measurement and primary vertex determination with accurate momen-

tum resolution with a tracking efficiency of 90 % or higher. Additionally it serves as a tool for two-track separation in the region of $p_t < 10$ GeV/c. Stretching from an inner radius of 0.8 m to an outer radius of 2.5 m it correctly identifies patterns of the high multiplicity PbPb central collisions with up to 20.000 particle tracks per event in the sensitive volume.

- **Transition Radiation Detector (TRD)** [7]: A dedicated section on the TRD can be found in chapter 4.
- **Time Of Flight (TOF)** [32]: The TOF detector consists of 18 sectors located at a radial distance of 3.7 m from the beam line with full ϕ coverage. Its main components are multi resistive plate chambers, covering about 150 m². With a time resolution in the 50 ps range, TOF can provide excellent π/K separation up to 2.2 GeV/c and K/p separation up to 4 GeV/c.

In Fig. 3.2 many more subsystems are visible, however, not all are described here and only subsystems of significant importance for particle identification at ALICE were sketched. More information can be found in [5] and in the specific technical design reports.

4. The ALICE Transition Radiation Detector

4.1. The TRD Design

The ALICE *Transition Radiation Detector* (TRD) is a junction of 522 readout chambers, distributed into 18 supermodules [7]. Each supermodule is segmented into 5 sections, so called *stacks*, along the z -direction. As motivated by the main physics goals of the TRD (chapter 1), the readout chambers are positioned in 6 layers, which cover a radial range of $2.9 < r < 3.7$ m. With a total length of maximal 7.0 m in the z -direction, the complete TRD covers a pseudorapidity range of $-0.9 < \eta < 0.9$ and has an azimuthal coverage of 2π . To support the whole TRD, a main support structure, the *space frame*, is placed inside the L3 magnet. It is capable of carrying the 75 tons of total weight of many ALICE subsystems, such as the ITS, TPC, TRD, TOF, HMPID and PHOS. A TRD supermodule itself is a closed volume functioning as one unit of installation, with connections to outside services such as low voltage, high voltage, cooling, gas and readout/control lines. These services are supported by the *baby space frame*, a structure which can be mounted into the space frame but remains detached. After the construction, the supermodules are inserted into the 18 sectors in the space frame. Supermodules located in sectors 13, 14 and 15 do not have any readout chamber inserted in their central stack to reduce material in front of the PHOS [33] detector. A schematic view of the space frame, filled with 18 supermodules, is found in Fig. 4.1. More information is available in [7].

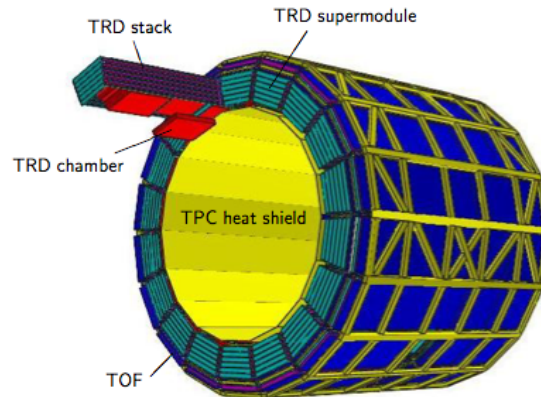


Figure 4.1.: Axonometric view of the ALICE space frame (yellow bars), with 17 inserted supermodules (green) between the TPC heat shielding (yellow plates) and the TOF subsystem (blue). One supermodule is only partially inserted into the space frame. Here, the segmentation into individual chambers (red) is visible. This figure has been taken from [34].

4.2. The TRD Readout Chamber

The previously mentioned 522 readout chambers each consist of three major components, a *radiator*, a *multi-wire proportional chamber* with a drift region, and *front-end electronics*. A schematic cross section of a readout chamber can be seen in Fig. 4.2. The front-end electronics is mounted on a honeycomb sandwich support structure on top of the 3.7 cm-thick multi-wire proportional chamber, which is located behind the 4.8 cm-thick sandwich radiator. The radiator also serves as "entry window" for particles into the chamber.

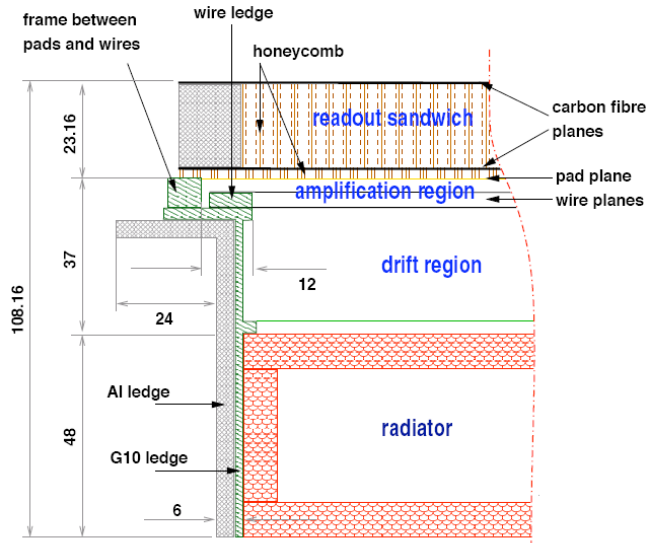


Figure 4.2.: Schematic cross section of a readout chamber. Particles enter through the radiator into the drift region. Units are in mm. This figure has been taken from [34].

The functionality of the TRD readout chamber is similar to a TPC, as shown in Fig. 4.3. If a minimum ionizing particle traverses through the entrance window into the drift volume, electrons are produced by ionization and excitation of the gas. Because of the applied high voltage, these primary ionized electrons (primary clusters) drift towards the anode wires. In the vicinity of the wires, due to the inhomogeneous electric field, they eventually start avalanches (see chapter 2.3). The positive ions created by these avalanches then propagate towards the pad plane, inducing a positive signal. Additionally, as explained in chapter 2.2.4, highly energetic electrons ($\gamma \gg 1000$) passing the radiator produce transition radiation, allowing a simple identification from other particles, i.e. pions. This is due to the large amount of primary ionized electrons produced by the energetic photons, which are absorbed in the gas upon entering the chamber. For a 10 keV photon from transition radiation the typical absorption length in Xenon is ≈ 2 mm, for a 30 keV photon ≈ 2 cm. Thus, the generated signal of the transition radiation has the longest possible drift length, which corresponds to the longest possible drift time, and leads to a second amplification peak. Because $e^{+/-}$ and $\pi^{+/-}$ are identified not only via their deposited charge, but essentially through the drift time and time of arrival of the signal, the readout chamber is considered as a small time projection chamber.

Fig. 4.4 shows a typical average pulse height distribution as a function of the drift time

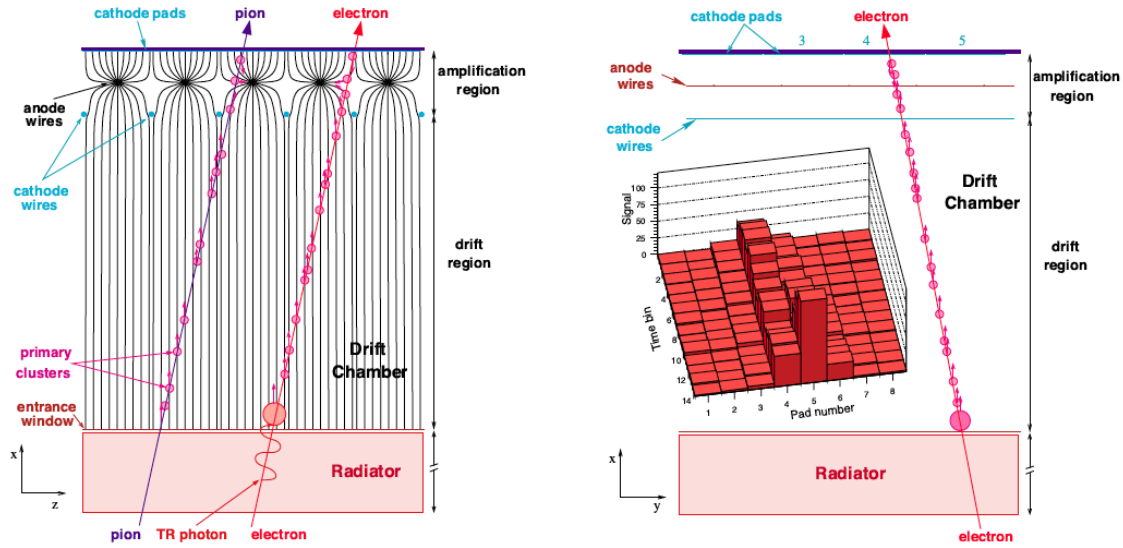


Figure 4.3.: Left: Schematic xz-view of a readout chamber with electric field lines. The large amount of primary ionized electrons at the beginning of the electron track inside the drift volume originates from transition radiation photons absorbed. Right: Schematic xy-view of a readout chamber. As shown in the inset, the primary ionized electrons generated by transition radiation reach the cathode pads in the later time bins. This figure has been taken from [7].

measured with a TRD prototype chamber. During the measurements with a test beam of 1 GeV/c electrons, the chamber was operated with $Xe - CH_4$ [90-10]. The expected pulse height distribution for electrons without transition radiation was determined by scaling a pion distribution with a factor of 1.45, measured in a separate experiment without radiator. For this signal, a flat distribution behind the first peak, which originates from the amplification region, is expected. However, as the signal arising from transition radiation sits on top of this plateau, caused by the energy loss of transversing particles in the drift region, a second peak at higher drift times is observed.

4.2.1. Radiator

Stringent mechanical and geometrical constraints limit the choice of material for the ALICE TRD radiator [7]. On the one hand, it has to provide high efficiency for transition radiation, on the other hand it cannot be significantly larger than 15 % of a radiation length. Too much material would have strong negative effects on the performance of the TRD and other ALICE subsystems positioned behind it. This is due to particle interactions such as multiple scattering, conversions and Bremsstrahlung in the material. Besides, the radiator has to contribute to the stability of the readout chambers to prevent geometrical changes, since the chambers are operated at overpressure. The decision for a radiator sandwich was made because the design also has to avoid dead material to prevent acceptance losses. Shown in Fig. 4.5, 8 mm-thick sheets of polymethacrylimide (PMI) foam, called Rohacell HF71, were chosen to cover the main radiator material, polypropylene fibers of 17 μm thickness. The sheets are the optimal compromise between high mechanical and chemical stability and good transition radiation production rate. For more geometrical

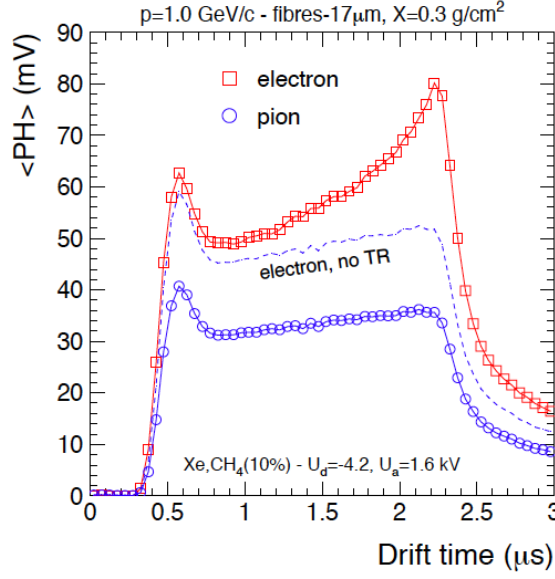


Figure 4.4.: Average pulse height as a function of drift time for 1 GeV/c electrons and pions. The electron signal is shown with (solid red line) and without (dashed blue) transition radiation. This figure has been taken from [7].

stability they were reinforced by glass fiber sheets. The inner side of the radiator, facing the multi-wire proportional chamber, is covered by a aluminized 25 μm Mylar foil. This foil serves as entrance window for particles and as drift electrode for the readout chamber.

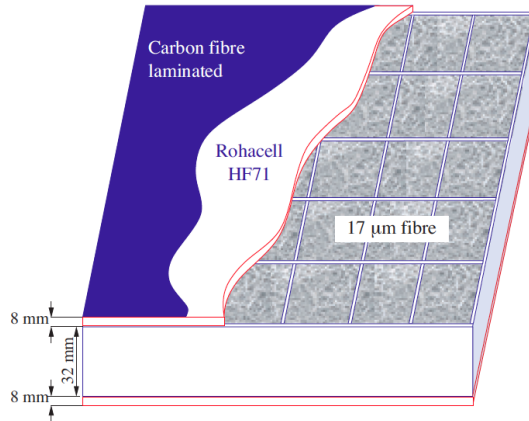


Figure 4.5.: Schematic view of the sandwich radiator used for the ALICE TRD. Two plates of carbon fiber reinforced Rohacell HF71 foam (blue & white) surround the main radiator material, polypropylene fibers (grey). This figure has been taken from [35].

4.2.2. Multi-Wire Proportional Chamber with Drift Region

A multi-wire proportional chamber (MWPC) filled with $Xe - CO_2$ [85-15] and operated at 1 mbar overpressure is mounted on top of the radiator [7], separated by a drift region.

Because only $275 e^-/cm$ are produced for a minimum ionizing particle passing the drift region, the signal generated by the primary ionized electrons needs further amplification (see chapter 2.3).

The pad plane and the cathode wire plane, which both have ground potential, are separated by the same distance through the anode wire plane (see Fig. 4.6). The anode wires are operated at nominal positive potential of 1530 V. The gap length was tuned to provide appropriate charge sharing on the pad plane. Also, the cathode wires are staggered with respect to the anode wires, so they separate the drift field from the amplification region, and prevent about 72 % of the positive ions created in an avalanche to reenter the drift region. This design allows specific tuning of drift velocity and gas gain respectively. The MWPC has a gas amplification of about 3500. Gain variations are mainly caused geometrical imperfections and the operation at slight overpressure of 1 mbar. As a consequence, the deformation is expected to lead to gain variations of 7 % in a chamber. Gain variations of $< 3 \%$ are expected due to gravitational sag.

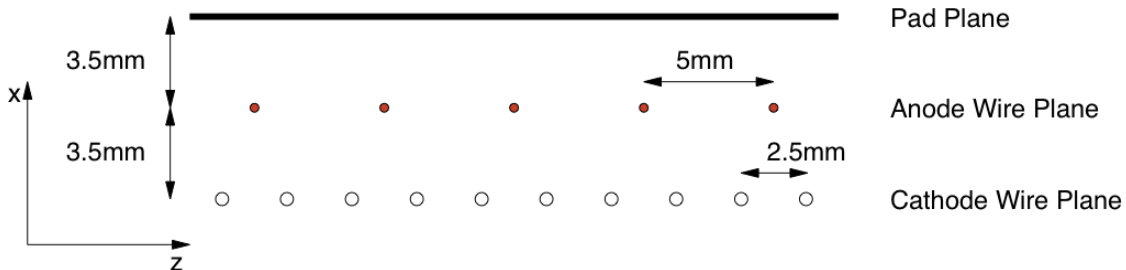


Figure 4.6.: xz -view of the multi-wire proportional chamber. The anode wire plane is centered between pad and cathode wire plane. This figure has been taken from [7].

For high detection resolution the pad plane is segmented, so the track position can be measured via induced charge sharing of adjacent pads. Depending on the layer it is located in, the chamber length differs by a few centimeters so the pad sizes increase with the increasing radial position of the individual chamber in the supermodule as well. The granularity of the pad plane depends on the type of chamber used: For chambers located in the second stack of each supermodule, so called C0 chambers, the pad plane is segmented into 12 pad rows and 144 pad columns. In any other stack within a supermodule so called C1 chambers are used. These are segmented into 16 pad rows and 144 pad columns respectively. In total the ALICE TRD consists of 1,150,848 readout pads [7]. The size of the pads can be taken from table 4.1.

Because of their different dimensions, each chamber is also tagged with an additional information on the layer. For example, a chamber of type L0C1 would be positioned in the layer closest to the interaction point, in any stack but stack two. The choice of gas $Xe - CO_2$ [85-15] was derived from the need of a high X-ray photoabsorption probability, which excludes lower mass noble gases from consideration. The drift velocity is chosen to be $1.5 \text{ cm}/\mu\text{s}$ at a drift field of 700 V/cm . CO_2 serves as a quench gas, suppressing the emission of photons, which are produced when the nuclei de-excite. Additionally, CO_2 is very useful in terms of safety, as it is non-flammable.

| Type | L_z | $W_{r\phi}$ | # of rows | α_{tilt} | L_{opad} | L_{ipad} | W_{opad} | W_{ipad} |
|------|-------|-------------|-----------|-----------------|------------|------------|------------|------------|
| L0C0 | 1080 | 922 | 12 | -2 | 80 | 90 | 5.15 | 6.35 |
| L0C1 | 1220 | 922 | 16 | -2 | 75 | 75 | 5.15 | 6.35 |
| L1C0 | 1080 | 966 | 12 | +2 | 80 | 90 | 5.85 | 6.65 |
| L1C1 | 1220 | 966 | 16 | +2 | 75 | 75 | 5.15 | 6.65 |
| L2C0 | 1080 | 1011 | 12 | -2 | 80 | 90 | 7.05 | 6.95 |
| L2C1 | 1290 | 1011 | 16 | -2 | 75 | 80 | 7.05 | 6.95 |
| L3C0 | 1080 | 1055 | 12 | +2 | 80 | 90 | 7.75 | 7.25 |
| L3C1 | 1360 | 1055 | 16 | +2 | 75 | 85 | 7.75 | 7.25 |
| L4C0 | 1080 | 1099 | 12 | -2 | 80 | 90 | 8.45 | 7.55 |
| L4C1 | 1430 | 1099 | 16 | -2 | 75 | 90 | 8.45 | 7.55 |
| L5C0 | 1080 | 1144 | 12 | +2 | 80 | 90 | 9.65 | 7.85 |
| L5C1 | 1450 | 1144 | 16 | +2 | 85 | 90 | 9.65 | 7.85 |

Table 4.1.: Sizes of different TRD chamber types. All numbers are in mm, except ' # of rows ' and ' α_{tilt} '. The latter is measured in degrees. L_z is the length of the chamber in z-direction, $W_{r\phi}$ the width along the $r\phi$ -axis. The subscripts *opad* and *ipad* describe the dimensions of the outer and the inner pads in z-direction respectively.

4.2.3. Front-End Electronics

The TRD *Front-End Electronics* (FEE) is used for readout and analysis of the signals induced on all pads in the individual readout chambers. In case the TRD is used for triggering, the information of chambers positioned in all six layers must be combined at a point close to the readout chambers, thus most of the FEE is directly soldered on them. Fig. 4.7 shows the components for one channel.

The basic building blocks [7] are listed in the following:

- Charge sensitive **PreAmplifierShAper** (PASA): The shaping preamplifier is customized towards low noise and low power. It operates at a conversion gain of 6.1 mV/fC. The channel-to-channel cross talk is limited by the pad-to-pad capacitance of 6.5 pF between neighboring pads in a single row. The cross talk within the PASA itself is below 0.3 %.
- **Local Tracking Unit** (LTU): The following building blocks are grouped together into this chip, which determines the *tracklets*. A tracklet is a linear approximation of a track in a single readout chamber (chapter 8.2.2).
 - *Analog to Digital Converter* (ADC): This 10 bit 10 MHz low power analog chip is connected to digital circuitry, in which data is processed and stored in event buffers for readout.
 - *Tracklet Pre Processor* (TPP): In order to prepare the information necessary for the *Tracklet Processor* (TP), the TPP processes the data during the drift time at digitization rate. Several digital filters are applied during the online reconstruction, i.e. a *Gain Correction Filter*, a *Non-Linearity Filter* and a *Tail Cancellation Filter*, among others. The online gain correction uses the relative pad gain factors found in the Krypton calibration performed in this thesis.

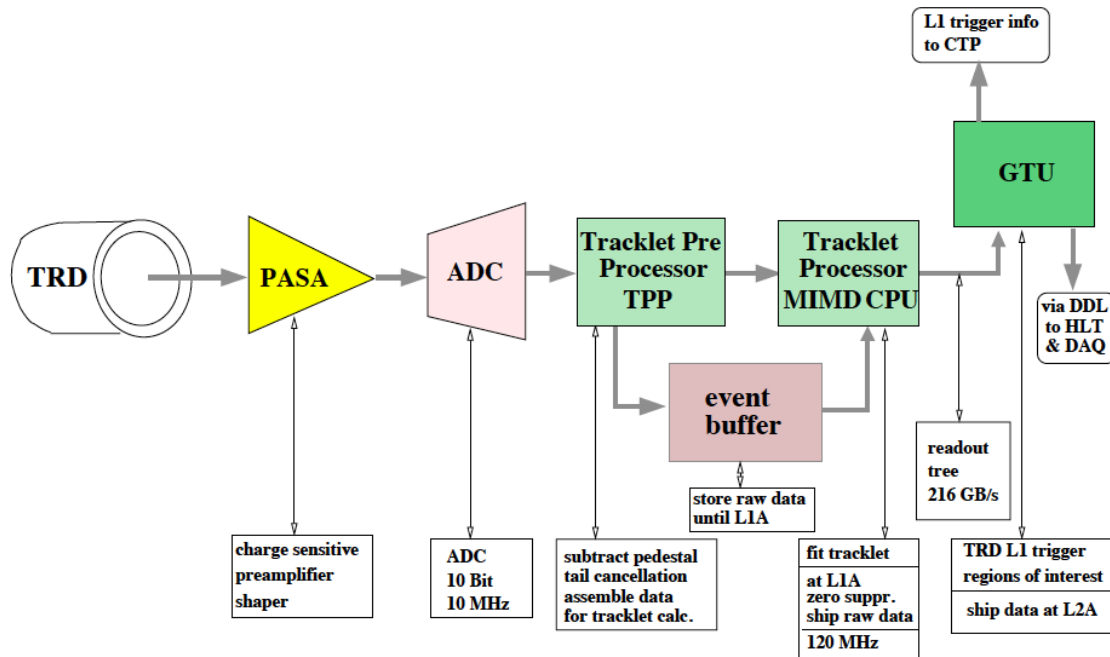


Figure 4.7.: Logical components of a single channel of the TRD Front-End Electronics. This figure has been taken from [7].

- *Tracklet Processor Multiple Instruction Multiple Data* (MIMD) CPU: This micro CPU operates at 120 MHz and processes the data of all time bins. Here, potential tracklets are determined and shipped.
- **Global Tracking Unit** (GTU): Combines and processes the trigger information from single readout chambers.

18 FEE channels are grouped together on one *Multi-Chip Module* (MCM), which is soldered directly on the readout motherboards. This results from a compromise between minimal radiation length, power and cost. After all, each MCM houses two chips, the PASA and the LTU, from where the information is then shipped to the GTU via a high-speed data link [7].

4.3. Chamber Numbering

Throughout the analysis in this thesis, whenever a specific chamber is considered, the location of the chamber will be given by the following coordinates: (sector-stack-layer). These coordinates can be calculated from the individual chamber number with the following formula:

$$\text{Chamber}_{Id} = \text{sector} \times 30 + \text{stack} \times 6 + \text{layer} \quad (4.1)$$

Here, according to the TRD geometry (chapter 4.1), Chamber_{Id} is a number between

0 and 539, *sector* is counted from 0 to 17 and *stack* and *layer* are numbered from 0 to 4 and 0 to 5 respectively.

For example chamber 333 is located in (11-0-3), meaning sector 11, stack 0, layer 3.

4.4. The ALICE Coordinate System

Within this thesis, the coordinate system as it is shown in Fig. 4.8, has been used, with the origin at the collision point in the center of the central barrel. The x-axis is declared as pointing horizontally to the center of the LHC, and the y-axis in upward direction. As a consequence of a right-handed coordinate system, the z-axis points into the direction of the beam, away from the ALICE Muon arm. As for cylindrical coordinates $r\phi$ increases counter-clockwise when looking into the direction of the negative z-axis [36].

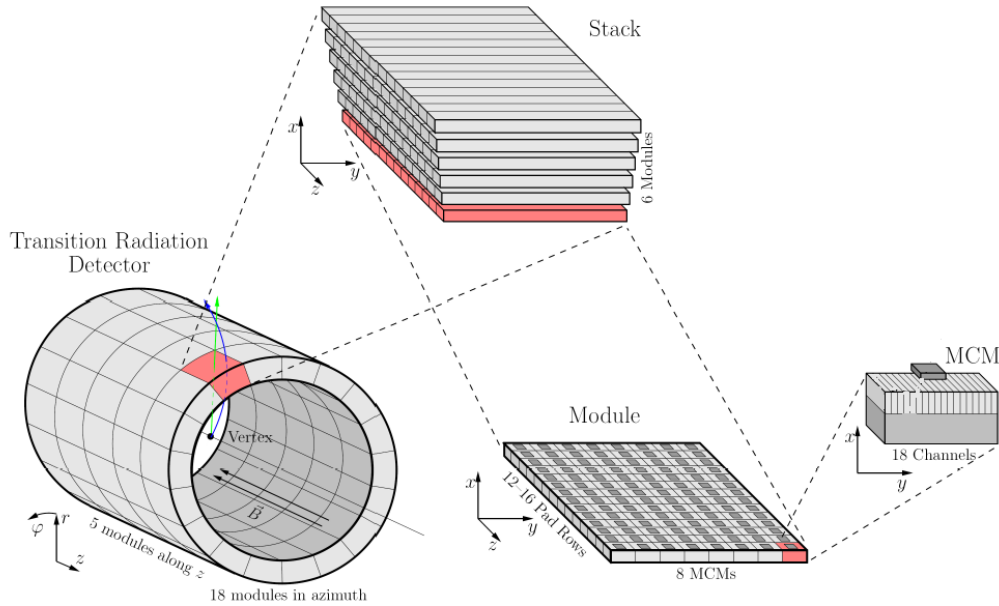


Figure 4.8.: Axonometric view of the ALICE TRD and exploded view of its components. The coordinates have been adjusted to the global ALICE coordinate system. This figure has been taken from [37].

Pad columns increase in positive $r\phi$ -direction whereas pad rows decrease along the z-axis [38]. Given the drift velocity of $v_d = 1.5 \text{ cm}/\mu\text{s}$ and a drift region of 3 cm, the time binning of the TRD was set to 30 time bins, each bin corresponding to up to 100 ns. A sketch of the pad geometry can be seen in Fig. 4.9. Here the time bins increase vertically into positive x direction, so the axis labels generally agree with the global ALICE coordinate system.

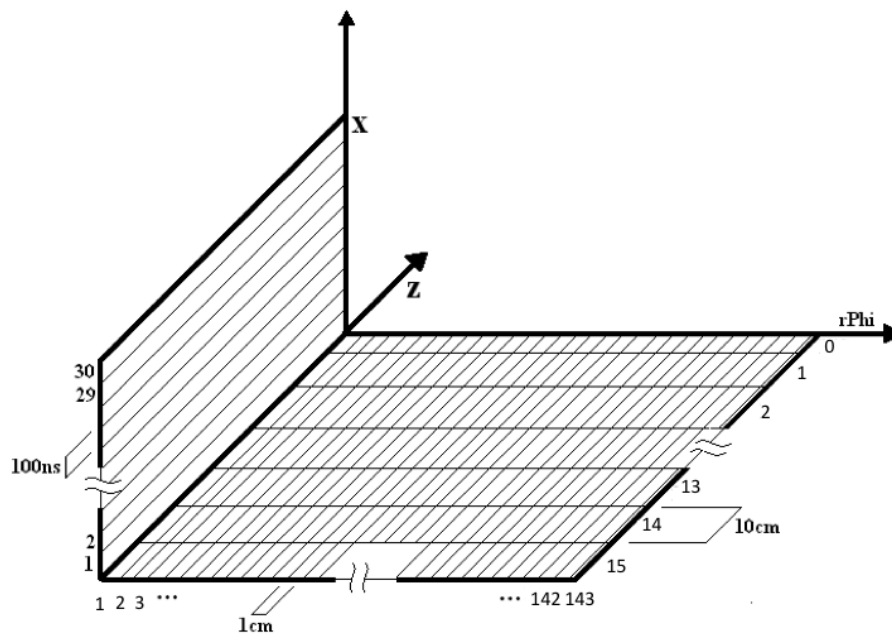


Figure 4.9.: Simple drawing of the pad plane. Pad rows increase in negative z -direction, pad columns increase along the $r\phi$ -axis. For simplicity, the pad dimensions plotted here are 1×10 cm. More details on the pad geometry can be found in table 4.1. The figure was inspired by [39].

5. Concept of Calibrating with Krypton

In this thesis, the gain calibration of the ALICE TRD has been repeated for seven of the ten installed super modules, whereas it was done for the first time for sectors 11, 15 and 16 (see Fig. 6.2), which were newly installed since the previous calibration run. The properties of the radioactive decay are so useful, because the decay electrons deposit energy in the range of 9 - 42 keV, which covers the same range of energy as the energy deposition of minimum ionizing particles in often-used gases. A comparison is shown in table 5.1.

| Gas | Z | Mass (g/mol) | Minimum Ionization Energy Loss (keV/cm) |
|--------|----|--------------|---|
| Ne | 10 | 20.18 | 1.446 |
| Ar | 18 | 39.95 | 2.525 |
| Xe | 54 | 131.29 | 6.882 |
| CO_2 | 22 | 44.00 | 3.351 |
| CH_4 | 10 | 16.00 | 1.613 |

Table 5.1.: Proton number (Z), mass and minimum ionization energy for minimum ionizing particles in different gases. Numbers are taken from [21].

The concept of calibrating proportional counters with Krypton is well established. Many collaborations with different detector technologies, for example the STAR TPC [40], the ALEPH and DELPHI [41] calorimeters respectively, the NA49 TPC [42], the ALICE TPC and TRD [39] were calibrated with ^{83}Kr before.

The homogenous distribution of the radioactive isotope within big gaseous volumes is rather straight forward, as the mother isotope, ^{83}Rb , is a solid and therefore can simply be inserted into the gas flow of the relevant system. This means no handling of radioactive gas is necessary, because after approximately 5.4 hours (3 half-lives) after the source has been detached from the gas system no measurable radioactivity remains in the system. For example, a solid Rubidium source (chapter 6.1.1) was connected to the ALICE TRD gas system. In the following the decay properties of ^{83}Kr will be explained in more detail and special emphasis will be put on the range of the decay electrons, as this is a relevant information for the further analysis.

5.1. Krypton Properties

$^{83}_{37}Rb$ does not directly decay into ground state ^{83}Kr , but decays via electron capture (EC) with a half-life of 86.2 days into various excited states of $^{83}_{36}Kr$. In 92 % of the cases the decay into the ground state of ^{83}Kr happens via the isomeric (metastable) state ^{83m}Kr at an excitation level of 41.56 keV (half-life 1.86 h). $^{83}_{37}Rb$ may also decay directly into a state at the energy level of 9.41 keV (half-life 155.1 ns). To further understand the Krypton

decay spectrum in Fig. 5.1, special emphasis is given to the decay of the two previously mentioned states.

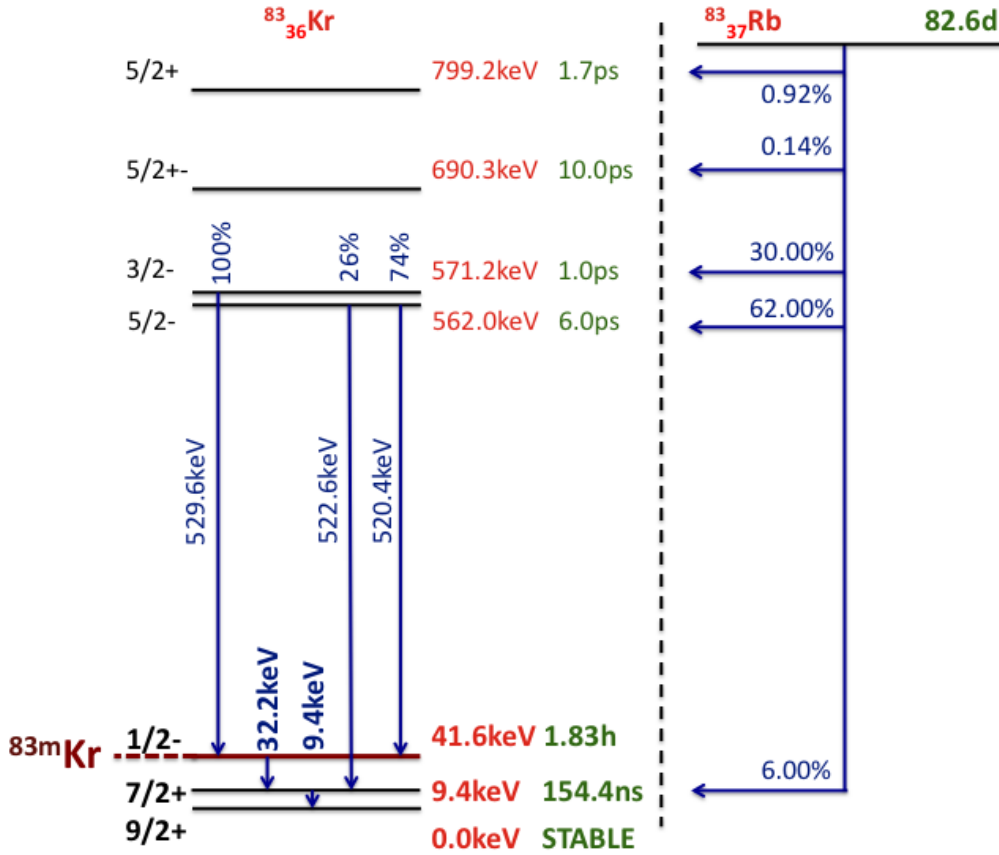


Figure 5.1.: Schematic drawing of the decay of ^{83}Rb into ^{83}Kr . Energy levels, their half-lives, and decays with their energy and probabilities are presented. Spin-parity is shown for the Krypton states only. The most probable decay goes via the isometric state ^{83m}Kr (bold) at a level of 41.6 keV. The energy levels are scaled in proportion. The data was taken from [43].

Most of the time both relevant levels de-excite via internal conversion (IC) with an electron to photon ratio of $(e/\gamma)_{41.56 \text{ keV}} = 2035$ and $(e/\gamma)_{9.41 \text{ keV}} = 17.09$. During this process the energy of the excited nucleus is transferred to a shell-bound electron, which, as implied by the high e/γ -ratio, is ejected. Dependent on its former shell, the electron carries an energy of

$$E_{e^-} = E_\gamma - E_{shell} \quad (5.1)$$

The atomic electron configuration with the left-behind hole in the shell then de-excites via fluorescence (emission of X-ray photon) or Auger electron emission. The branching ratios as well as the different channels of de-excitation can be seen in table 5.2. In 24.8 % [43] of the cases, the decay $41.56 \text{ keV} \rightarrow 9.41 \text{ keV}$ happens through internal conversion (IC) of a K-shell electron. The remaining atomic electron configuration decays either via an X-ray photon or an Auger-electron [44]. However, IC in the outer shells N,L and M is more likely to happen, which means that the energy is carried by freed electrons in 84 % of the cases. Otherwise, the energy is distributed over the IC electron, the Auger-electron and

fluorescence photons. The decay from 9.41 keV to 0 keV is dominated by IC, excluding the K-shell, because the energy is not sufficient. The de-excitation energy is completely carried by Auger-electrons from the outer shell. In the remaining cases a single photon with the whole energy is produced. More details can be found in [40].

| Decay | Probability | IC from | BR | Hole Decay | γ Energy | e^- Energy |
|-----------------------------|-------------|----------|--------------------|-----------------------|-----------------|----------------|
| 41.56 keV to 9.41 keV | 24.80 % | K-shell | 64.37 % 35.63 % | X-ray Auger- e^- | 14.33 - | 17.82 32.20 |
| | 63.70 % | L-shell | - | Auger- e^- | - | 30.23 |
| 9.41 keV | 10.69 % | M-shell | - | Auger- e^- | - | 31.86 |
| | 0.78 % | N-shell | - | Auger- e^- | - | 32.13 |
| 9.41 keV to 0 keV | 95.00 % | K-shell< | - | Auger- e^- | - | 9.41 |
| | 5.00 % | - | - | X-ray | 9.41 | - |

Table 5.2.: Probability for internal conversion for different shells and energy levels. All energies are given in keV. The 41.56 keV level releases the energy in 84 % of the cases via electron emission and in 16 % of the cases via an X-ray and an IC-electron. The column ' e^- Energy' describes the summed energy carried away by Auger-and IC-electrons. For the internal conversion from the K-shell at the 41.56 keV energy level, the third column describes the branching ratio (BR) either into an X-ray or an Auger-electron.

The expected Krypton Spectrum, calculated with table 5.2 according to the following description of the decay peaks, is shown in Fig. 5.2.

The peaks are explained in the following.

- **41.56 keV:** Summed cascade decay from the 41.56 keV energy level via the 9.41 keV level to ground state, because of the high probability that no photon emission or K-shell fluorescence happens. Due to the short lifetime of the 9.41 keV level the total decay appears as a single cluster.
- **29.0 keV:** Either summed electron energy of 9.41 keV and approximately 19.5 keV, where K-shell fluorescence occurs, or 32.1 keV when the 41.56 keV level decays to the 9.41 keV level and the 9.41 keV photon escapes.
- **19.6 keV:** K-shell fluorescence occurs for both energy levels and only the decay-electron is measured.
- **12.6 keV:** Caused by conversion of K-shell fluorescence photons in the chamber medium.
- **9.6 keV:** Either the K-shell fluorescence photon is converted in the chamber medium, or the 9.41 keV electron is separated from the preceding de-excitation.

5.2. Range of Krypton Decay Electrons

The main difference between a measurement of Krypton decays and charged particles created from collisions with the ALICE TRD is, that the decay electrons are freed within the gas volume inside the TRD whereas electrons originating from collisions have a longer trajectory and travel through several layers of the detector. As a consequence, the signal

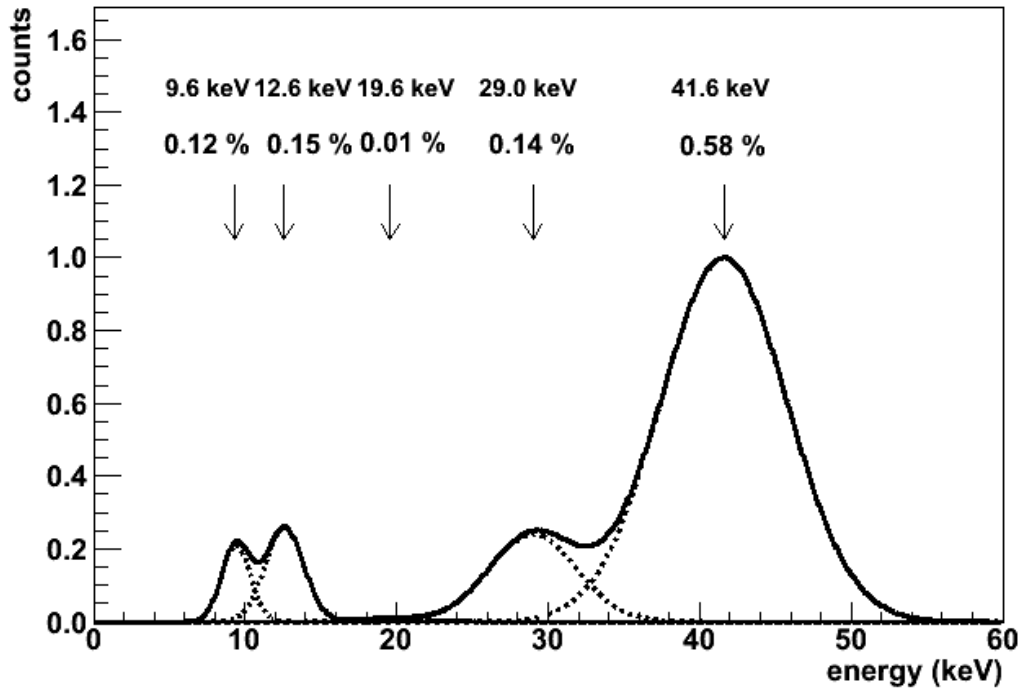


Figure 5.2.: Expected ^{83}Kr decay spectrum. Shown are the individual decay peaks at 9.6 keV, 12.6 keV, 29.0 keV and 41.6 keV (dashed lines), convoluted with a 10 % design energy resolution of the TRD [7]. In addition the branching ratio of each decay is displayed, estimated according to table 5.2. The peak at 19.6 keV is barely visible, due to the low branching ratio. The solid curve represents the complete spectrum.

distribution in the gas looks different. To ensure finding the correct location of the electron cluster from a Krypton decay within the analysis, the range of the produced charged particles (decay- e^-) needs to be considered. Integrating the Bethe formula of electrons over a range, such that the initial energy equals the total energy deposited in the medium, would give a first estimate of the distance travelled. However, randomizing effects of multiple collisions, especially at low electron energies, result in a wrong estimate of the left-behind path. Therefore the following empirical relation is used

$$R(E_{\text{kin}}) = \frac{A \cdot E_{\text{kin}}}{\rho} \left(1 - \frac{B}{1 + C \cdot E_{\text{kin}}} \right) [23]. \quad (5.2)$$

Here, $A = 5.37 \cdot 10^{-4} \text{ gcm}^{-2} \text{ keV}^{-1}$, $B = 0.9815$ and $C = 3.123 \cdot 10^{-3} \text{ keV}^{-1}$ are constants, and E_{kin} describes the initial kinetic energy of the electron before it entered the medium. The density of the TRD gas mixture $Xe - CO_2$ [85-15] at atmospheric pressure is:

$$\begin{aligned} \rho &= (0.85 \times 5.48 \cdot 10^{-3} \text{ gcm}^{-3} + 0.15 \times 1.84 \cdot 10^{-3} \text{ gcm}^{-3}) \\ &= 4.934 \cdot 10^{-3} \text{ gcm}^{-3} \end{aligned} \quad (5.3)$$

5. Concept of Calibrating with Krypton

Considering this density, the range of the electrons in the gas medium is calculated. The values and the estimates of the range expressed in time bins, pad rows and columns are listed in table 5.3.

| $E_{kin}(keV)$ | Range (mm) | Pad Columns | Pad Rows | Time Bins |
|----------------|------------|-------------|----------|-----------|
| 9.4 | 0.48 | 1-2 | 1-2 | 1-2 |
| 12.6 | 0.76 | 1-2 | 1-2 | 1-2 |
| 19.6 | 1.60 | 1-2 | 1-2 | 1-2 |
| 29.0 | 3.16 | 1-2 | 1-2 | 1-2 |
| 32.2 | 3.79 | 1-2 | 1-2 | 1-2 |

Table 5.3.: The table states the range of the electron in the chamber gas for different energies in units of cm and according to the pad dimensions. Note that the decay energy of 32.2 keV does not come from a single electron decay but is a cascade decay of two electrons with 32.2 keV and 9.4 keV energy respectively.

The range of the electrons, calculated with Eqn. 5.2, as a function of the electron kinetic energy is plotted for two different gas mixtures in Fig. 5.3. The $Xe - CO_2$ gas mixture corresponds to the current TRD settings, whereas the $Ar - CO_2$ gas mixture was used for the previous calibration. The calculation is only valid for atmospheric pressure.

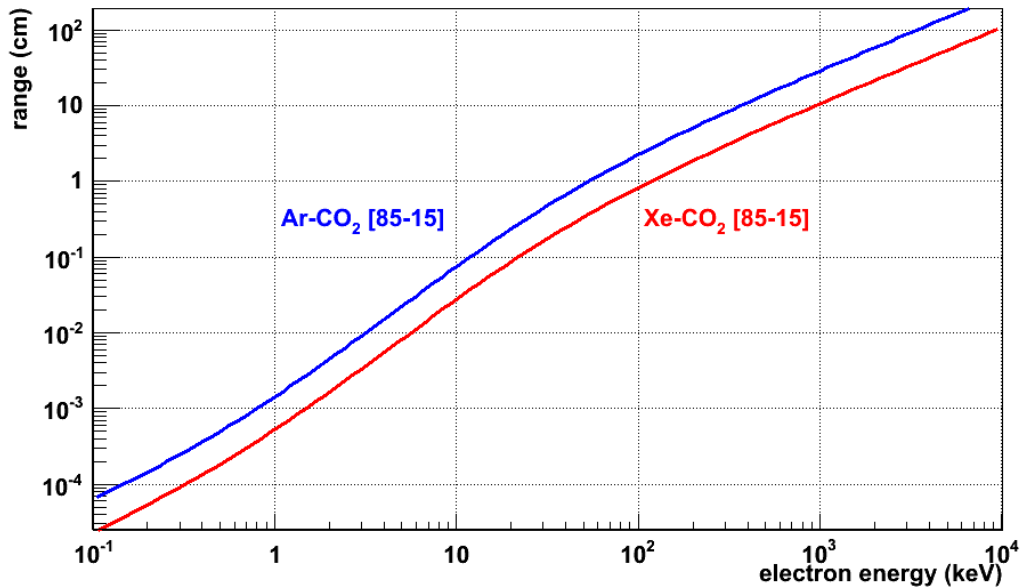


Figure 5.3.: Range of the Krypton decay electrons as a function of their initial kinetic energy for two different gas mixtures, $Xe - CO_2$ [85-15] (red) and $Ar - CO_2$ [85-15] (blue). As the Xenon density is larger than the one of Argon the range in the Xe-mixture is much smaller.

6. Experimental Setup and Data Taking of the Krypton Calibration

The data acquisition of the Krypton calibration run was carried out between February 2nd and 10th, 2011. During the last two days of data taking additional runs with different high voltage settings were recorded. In the following, information on the experimental setup and on the data taking are presented. Challenges, which occurred during the data taking, as well as resulting decisions are also described.

6.1. Foregoing Considerations

6.1.1. Properties of the available Rubidium Source

The decay of Rubidium ($^{83}_{37}\text{Rb}$) into metastable Krypton (chapter 5) was used for the TRD calibration. The available solid Krypton source, also used for the TPC calibration in February 2011, was produced at the *ISOLDE* facility on July 9th, 2010, with an intensity of 3 MBq. Given that the half-life of $^{83}_{37}\text{Rb}$ is $t_{\frac{1}{2}} = 86.2$ days, one can estimate that the source had an activity of 563 kBq at the beginning of the data taking period. Further considering that the activity follows an exponential decay, the activity dropped down to 528 kBq at the end of the data taking period on the 10th of February. The activity of the Rubidium source as a function of time can be seen in Fig. 6.1.

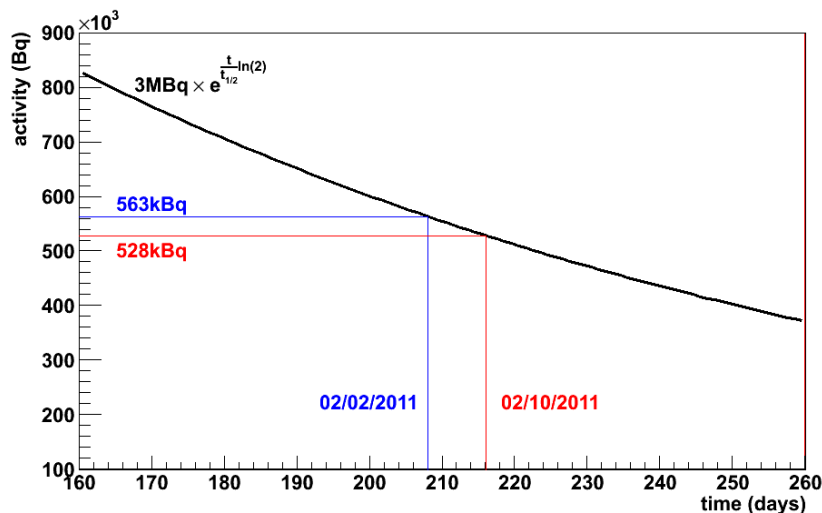


Figure 6.1.: Estimated activity of the ^{83}Rb source. The first day of data taking of the Krypton calibration is marked in blue, the last day in red. The abscissa is the time in days after the creation of the source.

6.1.2. Data and Statistics

Prior to the actual data taking some considerations on the time necessary to collect sufficient statistics had to be made, knowing that the source is significantly weaker than the one used for the calibration run in 2009 [39]. Important factors for this calculation are the relevant TRD specifications, the data recording rate of the TRD, the minimum number of recorded Krypton decays per readout pad to ensure a good quality analysis of the data and the activity of the Rubidium source.

As presented in table 6.1, ten supermodules with a total of 294 chambers were installed in the L3 magnet prior to the data taking.

| TRD Sector | Chamber # |
|------------|----------------|
| 00 | 0-29 |
| 01 | 30-59 |
| 07 | 210-239 |
| 08 | 240-269 |
| 09 | 270-299 |
| 10 | 300-329 |
| 11 | 330-359 |
| 15 | 450-479 |
| 16 | 480-509 |
| 17 | 510-539 |

Table 6.1.: Ordering scheme of the chambers distributed in the TRD. Newly installed chambers are printed in bold letters. The chambers are numbered according to equation 4.1 in chapter 4.1.

The location of the installed sectors is shown in Fig. 6.2.

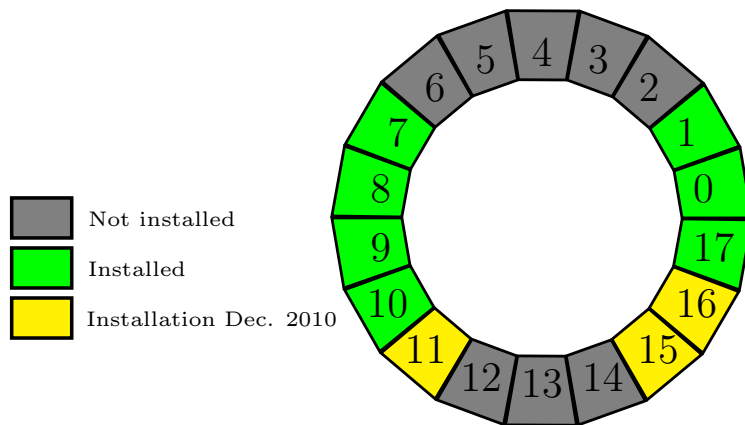


Figure 6.2.: Installation status of the ALICE TRD sectors. The figure was inspired by [8].

The calibration was planned to be carried out on pad-by-pad resolution, so the total number

of pads needs to be calculated first:

$$\begin{aligned} N_{\text{SM}} \times N_{\text{Pad-Columns}} \times (N_{\text{Chambers/SM}}^{16 \text{ Rows}} \times 16 + N_{\text{Chambers/SM}}^{12 \text{ Rows}} \times 12) \\ = 10 \times 144 \times (24 \times 16 + 6 \times 12) = 656,640 \text{ pads} = N_{\text{Pads}}^* \end{aligned} \quad (6.1)$$

All numbers on the TRD geometry can be found in chapter 4.1. However, because sector 15 does not have a central stack, the total number of pads in the installed chambers is:

$$N_{\text{Pads}} = N_{\text{Pads}}^* - (6 \times 144 \times 12) = 646,272 \text{ pads} \quad (6.2)$$

Further it was estimated that a minimum number of 1000 Krypton decays per pad are needed for sufficient statistics. As a result, the minimum number of decays to be recorded is:

$$N_{\text{Pads}} \times N_{\text{decays/Pad}} = 646.27 \cdot 10^6 \text{ decays} \quad (6.3)$$

However, as a consequence of the low gas flow, which leads to lower statistics in chambers at the end of the gas cycle (chapter 6.4.1), it was decided to record more than three times the estimated statistics, i.e. a total of $2.3 \cdot 10^9$ decays, to be safe having enough statistics, even in the chambers at the end of the gas flow. In order to estimate the time needed to record such a large amount of data one needs to consider the TRD settings shown in table 6.2.

| TRD Settings | | |
|-------------------------|-----------|--------------------------------|
| Active Sampling Time | R_t | 3 μs (30 time bins) |
| Average Source Activity | \bar{A} | 545.5 kBq |
| Trigger Frequency | f_{tr} | 3.8 kHz |
| Branching Ratio | BR | 58 % |

Table 6.2.: Information on the relevant factors to estimate the duration of data taking. Only the branching ratio (BR) of the main decay channel is listed.

The active sampling time was increased to 3 μs for the Krypton calibration, which corresponds to typically 1-2 Krypton decays per recorded event. A periodic trigger was set to a frequency of $f_{tr} = 3.8$ kHz, because there is no special event triggers on Krypton decays and the TRD cannot trigger itself. No higher frequency was possible, because of limited bandwidth of the data acquisition system and low voltage trips in the readout chambers FEE.

As a result, the following number of decays per second is expected:

$$\bar{A} \times R_t \times f_{tr} \times BR \approx 3607 \text{ decays/s} \quad (6.4)$$

That means, that for a TRD calibration on pad-by-pad resolution the minimum time to collect is $2.3 \times 10^9 \text{ decays} / 3607 \frac{\text{decays}}{\text{s}} \approx 7.38$ days. Note, that specifically for the purpose of the Krypton calibration the rate of the periodic trigger had been increased to 3.8 kHz.

6.2. Experimental Setup

As high-cost gas components such as Xenon are used, the TRD gas system was designed as a closed loop circulation system with its controlling units located on the surface. As can be seen in Fig. 6.3 the primary gas supplies, the mixer as well as the recovery unit are located in the SGX2 building at the experimental facilities of ALICE. For easy access the solid ^{83}Rb source was connected to the gas system via a bypass line close to the mixer. From here the gas is distributed into the TRD, located in the L3 magnet, via pipelines. Further details on the TRD gas system can be found in [7].

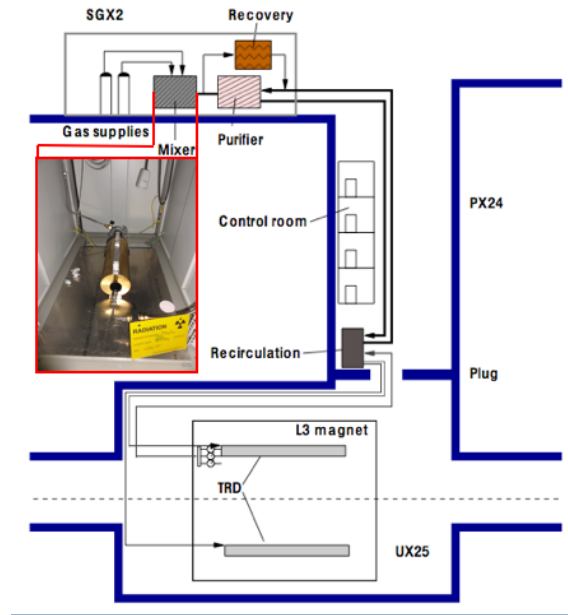


Figure 6.3.: Schematic layout of the TRD gas system. The solid ^{83}Rb source was connected via a bypass line close to the mixer. The figure has been inspired by [7].

6.3. Data Taking

According to calculations presented in chapter 6.1.2, a total of 134 runs with the high voltage setting of $U_{HV} = 1530\text{ V}$ were recorded, including approximately 2.3 billion Krypton decays. To study correlations between gain and high voltage settings, additional runs with different high voltages were recorded as listed in table 6.3.

Generally, after approximately one hour of data taking runs were stopped to limit the data size of the output files to a reasonable amount. With this configuration the data migration to the storage element was stable and no issues, such as data losses, were encountered. A schedule plot of the 2011 Krypton calibration campaign can be seen in Fig. 6.4. Here, the atmospheric pressure measure in the cavern as well as the gas admixture inside the TRD readout chambers are plotted as a function of the time. The installation of the Krypton source in the bypass line on January 31st is indicated by the black line prior to the data taking period. The valve of the source was opened shortly after the installation, to allow

| Anode high voltage (V) | # of runs | Run duration | Raw data size | # of events | # of Kr decays |
|------------------------|-----------|--------------|---------------|-------------------|-------------------|
| -1530 | 134 | 136.2 h | 91.0 TB | $1.81 \cdot 10^9$ | $2.28 \cdot 10^9$ |
| -1490 | 13 | 11.0 h | 7.5 TB | $1.50 \cdot 10^8$ | $1.91 \cdot 10^8$ |
| -1450 | 6 | 11.3 h | 7.6 TB | $1.54 \cdot 10^8$ | $1.95 \cdot 10^8$ |

Table 6.3.: Information on the runs recorded for the Krypton calibration and for studies of correlations between gain and high voltage.

saturation of the gas with Krypton decays in the complete gas cycle. This usually takes a few hours. The data taking periods with the nominal and reduced high voltage settings are indicated by the different shading styles.

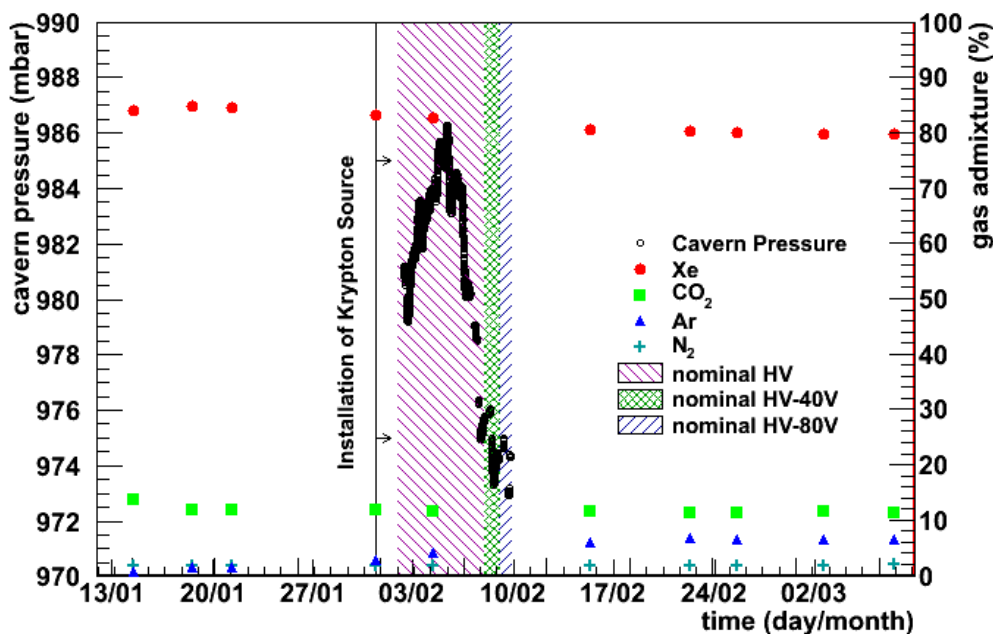


Figure 6.4.: Schedule plot of the Krypton calibration campaign. Presented are the installation of the Krypton source on January 31st (black line) and the periods of data taking with nominal high voltage settings (Feb. 2nd-8th; magenta shaded area), nominal voltage reduced by 40 V (Feb. 8th-9th; green shaded area) and nominal voltage reduced by 80 V (Feb. 9th-10th; blue shaded area). The cavern pressure (black circles) can be read off from the left ordinate, the gas admixture of the gas components (Xe, red dots; CO₂, green squares; Ar, blue triangles; N₂, cyan crosses) from the right ordinate.

6.4. Experimental Conditions during Data Taking

As possible sources of large systematic uncertainties, the atmospheric pressure changes inside the ALICE cavern, the gas admixture and the stability of the high voltage in all chambers were closely monitored. This information is stored in the offline condition data base, which was analyzed for the recorded runs.

6.4.1. Increase of Gas Flow

As visible in Fig. 6.5, each TRD sector inhibits three gas inlets, each circulating through two layers. Chamber numbers in the range of 0 to 29 are indicated in the figure. Here, the direction of the gas flow in the central two layers was swapped. The gas system was designed in this way to achieve a uniform regulated pressure in the chambers.

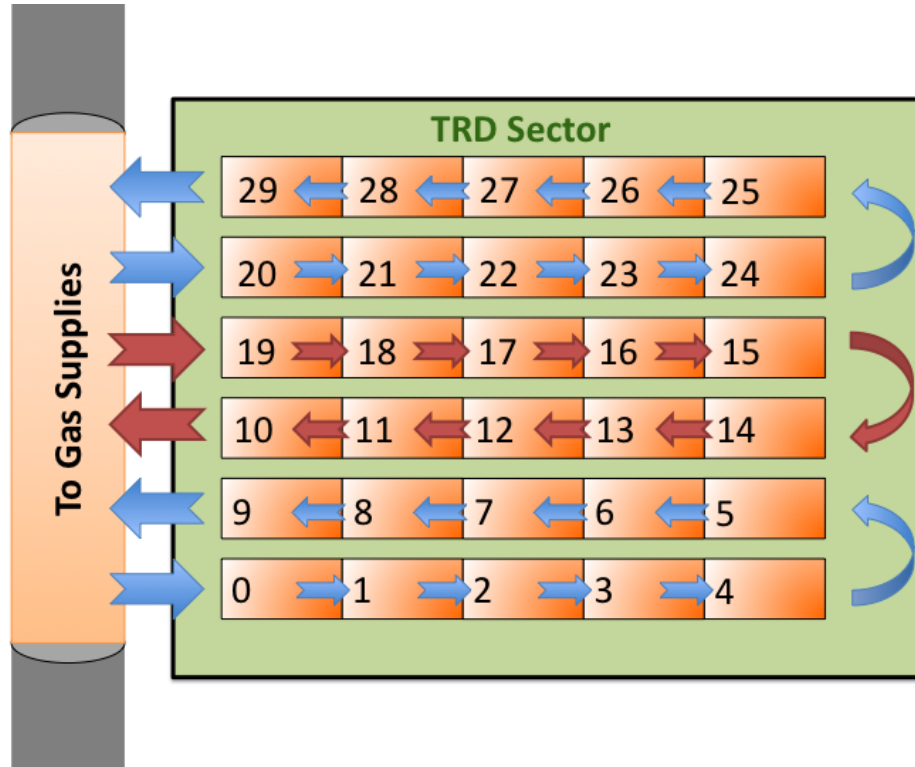


Figure 6.5.: Schematic drawing of the three gas inlets in a TRD sector. The flow direction of the gas coming from the supplies is indicated by the arrows. Each inlet circulates the gas through two layers. The connections, and thus the direction of flow, were swapped for the central two layers.

As a consequence of this design [7], during the calibration run in 2009 it was discovered that the Krypton decays did not reach the last chambers within the gas flow of each gas loop respectively [39], because the decay would happen before. To prevent this problem from evolving again, the gas flow was increased before the data taking period by 80 % up to approx. 900 l/h. In Fig. 6.6 the number of decays in each chamber within one gas circulation loop is drawn. Chambers of each sector (ordinate) are labeled from 0 to 29, corresponding to the numbering as in Fig. 6.5. The drop of statistics within increasing length of the inlet is clearly visible, where chambers at the end of the gas flow collected about a factor three less statistics. For example, in chamber number seven in the sector one, ≈ 500.000 decays were reconstructed in the first dataset (chapter 7.1). If the number of reconstructed decays still was not sufficient, the spectra of three adjacent pads were added, as explained in chapter 7.4. There are also three supermodules with swapped gas connections: sectors 9, 16 and partially sector 17 (chamber 10 to 29). This observation agrees very well compared to online measurements of the data quality monitoring. To be

able to calibrate the TRD on a pad-by-pad resolution, even in the chambers at the end of the gas flow, it was decided to collect sufficiently high amount of data, as explained in chapter 6.1.2.

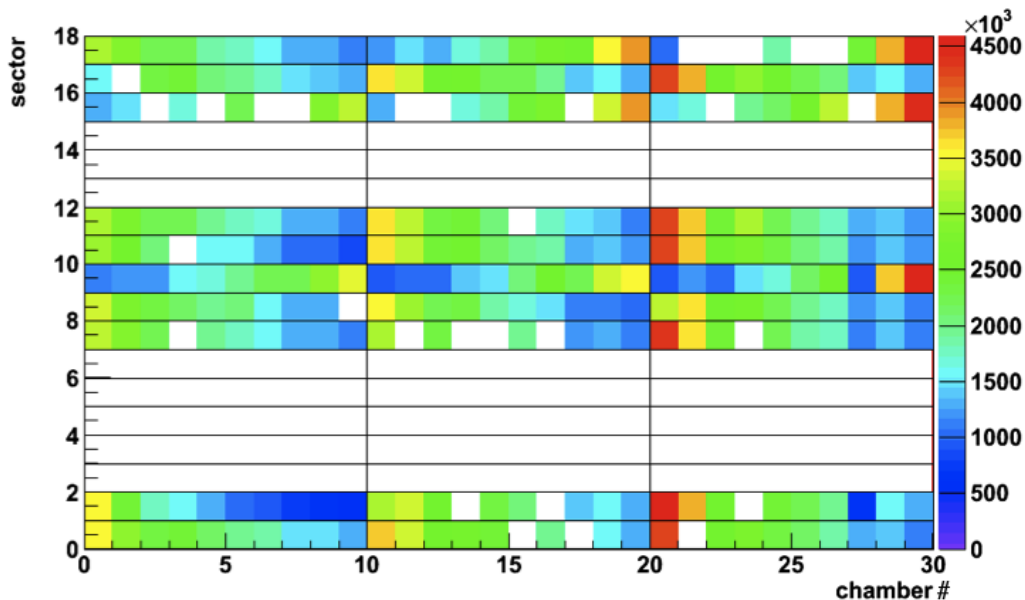


Figure 6.6.: Number of reconstructed decays in each sector for each chamber, recorded with the first dataset (chapter 7.1). Gas inlets circulate from chamber 0-9, 10-19 and 20-29. For supermodules 9 and 16 the gas connections have been swapped, and the gas flow increases vice versa. White bins are either faulty chambers or chambers not inserted in the experiment.

6.4.2. Change of Atmospheric Pressure

Even though it is a closed-loop gas system [7] the TRD is extremely sensitive to changes of the atmospheric pressure. These atmospheric pressure changes effect the detection properties of the TRD, because they effect the gas density inside the TRD and thus have a large impact on the gain (chapter 2.3.3). As visible in Fig. 6.7, relative changes of the atmospheric pressure measured in the ALICE cavern during the data taking are smaller than 0.71 %, therefore from chapter 2.3.3, equation 2.14, gain variations of the order of approximately 4 % are expected. Actual calculations can be found in chapter 7.5.5.

6.4.3. Gas Admixture

Shortly after the data taking period started, a sudden change of the gas composition within the TRD was observed. This was due to some leakage in a membrane module. Between the 13th of January and the 10th of March the gas admixture $Xe - CO_2 - N_2 - Ar$ [84.0-13.6-1.6-0.6] changed to $Xe - CO_2 - N_2 - Ar$ [80.1-11.2-2.2-6.6]. As shown in Fig. 6.4, the

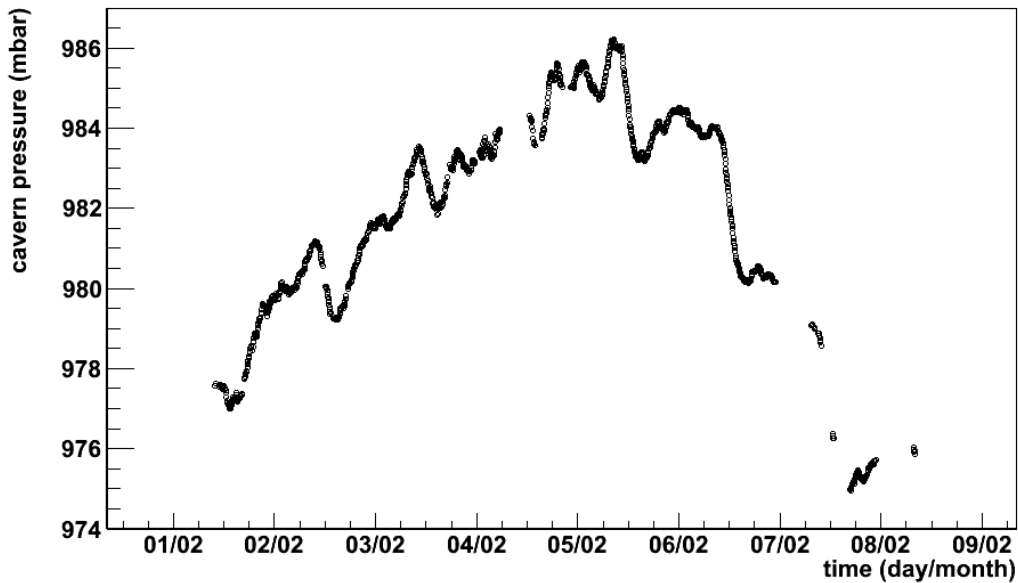


Figure 6.7.: Atmospheric pressure measured in the ALICE cavern as a function of time during the Krypton calibration data taking period.

amount of Argon (blue triangles) in the gas system steeply increased during the Krypton calibration data taking period, while the Xe-component (red dots) of the mixture decreased accordingly. Small amounts of $< 2\%$ of Ar and N_2 are typically included in the gas admixture, because they cannot be completely filtered out.

To understand and estimate how the change of the gas composition would effect the TRD performance, standalone simulations with GEANT3 [45] were carried out. Presented in Fig. 6.8, the simulations show that the energy loss for electrons and pions is slightly shifted to lower values which leads to sizable negative effects on the electron pion separation [46]. However, for the Krypton calibration no significant effects on the calculation of the relative gain factors were found, because after merging the data of all runs for the analysis, the contamination only led to a slight broadening of the spectrum, which is the same for all pads within the installed chambers and is ruled out after the normalization of gains of the readout pads to the chamber average gain value (chapter 7.4).

6.4.4. High Voltage Stability

All chambers which were newly installed were operated at 1530 V. However, other chambers, which were already calibrated, were set to have similar average gain, which is achieved by adjusting the actual anode high voltage for each readout chamber. The relation between gain and anode high voltage is studied in chapter 7.9.1. For the specific runs recorded in these measurements, the high voltage setting were modified. During the time period of the Krypton data taking the high voltage of the chambers was not adjusted or changed. A list of all chambers, at what voltage they were operated and if they were included in the analysis, can be found in the appendix in chapter A.2.

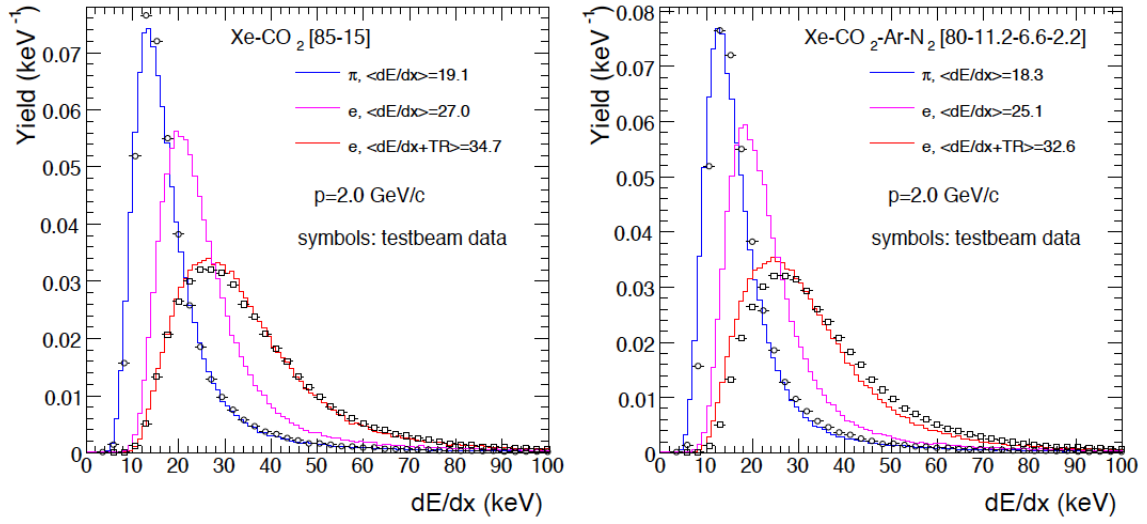


Figure 6.8.: Standalone simulation of electron and pion dE/dx with GEANT3 for the nominal (left) and contaminated (right) gas mixture. Symbols represent testbeam data whereas the blue, pink and red curve show simulation data for pions and electrons with and without transition radiation. This figure has been taken from [46].

7. Analysis and Results

Before the data collected for the Krypton calibration was analyzed, the recorded digits were converted into TRD *clusters* in a global data reconstruction step (chapter 7.1). The processing of the Krypton calibration was then split up into two major stages: First, a Krypton cluster finder was applied, which was specifically tuned to find Krypton decays. After noise cuts (see 7.3.1), It assigned these decays to the corresponding readout pad. An individual histogram with the assigned spectrum was created for each individual pad and chamber. Second, a new fit algorithm was developed to find the relative pad gain factors at the pad level functioning with low statistics and filtering out possible sources of instability of the fit algorithm, such as broken chambers, floating pads, edge effects within a chamber and bad fits. As an output, the analysis returned relative gain factors for each pad of the analyzed chambers. The pad gain factors were normalized to the chamber average, which was determined as the mean of the gain factors of all pads in the specific chamber. The chamber average was normalized to unity and differences in the pad gain are stored as values relative to the chamber mean. After the analysis of all calibration runs was completed, the relative pad gain factors were stored and uploaded into the offline condition data base, where they are available for all user analysis. In addition they are available for download into the FEE of the TRD.

In the following, the working principle and strategy of the analysis will be explained. Results and performance of the algorithm are compared to the previously used method [39]. Emphasis is also put on the development of the analysis code for the CERN GRID [47] to provide an efficient analysis of the large amount of data recorded. Finally, the results are presented and discussed.

7.1. Global Reconstruction and Analyzed Datasets

After the recorded raw data (chapter 6.3) was stored by the ALICE Data Acquisition (DAQ) it was used as input of the ALICE reconstruction framework on the CERN GRID. The GRID is a storage and analysis infrastructure used by a global collaboration of more than 140 computing centers in 35 countries and the four major LHC experiment. Here, the raw data was saved as *digits* and then converted into clusters. A digit is a digitized signal in ADC counts above the nominal pedestal of 10 ADC counts, stored in a special format by the readout detector. Noise is fluctuating in the range of 1 ADC count around the pedestal. The threshold for the zero suppression is 16 ADC counts, which means that the data of a pad is only stored, if at least one signal in a given range of time bins exceeds 16 ADC counts. In case of the Krypton calibration, this range was set to 30 time bins. The TRD standard cluster finder searches in seven pad columns within a single pad row in each time bin for the digit with maximum ADC counts, whereas only cluster above a minimum charge of 4.5 ADC counts after pedestal subtraction are considered. Under the assumption that they originate from a single particle, the signal of that specific pad and the

digits of its two neighbors are then summed to a cluster, which is assigned to the pad with the highest value in pulse height (in ADC counts). Together with the pad location and time bin in the TRD, the cluster information is then stored in the *Event Summary Data* (ESD), which is used for further analysis. The global reconstruction reduced the complete raw data size from ≈ 100 TB to ≈ 50 TB.

During the global reconstruction of the collected data, a bug in the reconstruction setup was found, making two thirds of the reconstructed data temporarily unusable. The cause was identified to be a wrongly updated TRD calibration file, masking runs of the Krypton calibration with an incorrect number of time bins. At that point of time the valid data corresponded to the output of 5.45×10^8 Krypton decays, as visible in table 7.1. After the bug was fixed, the remaining runs were reconstructed and collected into a second dataset. In total, 2.67×10^9 Krypton decays were recorded with nominal and adjusted high voltage settings, which corresponds to 153 runs. However, due to the just mentioned issues not all runs were processed again, even not in the later stage. Thus, a total of 2.01×10^9 Krypton decays were available for the analysis.

After the relative gain factors for all pads were calculated with the first dataset, it was decided to use these for the reconstruction of the second dataset, giving the possibility of an iterative analysis step and an absolute check of the calibration, as explained in chapter 7.2. Table 7.1 also displays the amount of data analyzed with reduced high voltage settings. Here only a small fraction of data was necessary to carry out the analysis on gain correlations versus the anode high voltage (chapter 7.9), because it was performed at the chamber basis.

| Dataset | # of runs | # of runs in % | # of Chunks | # of Chunks in % | # of Kr decays |
|---------|-----------|----------------|-----------------|------------------|--------------------|
| 1 | 33 | 21.57 | 43,216 | 20.43 | 5.45×10^8 |
| 2 | 76 | 49.67 | 99,295 | 46.94 | 1.25×10^9 |
| HV-40V | 13 | 8.50 | 15,102 | 7.14 | 1.90×10^8 |
| HV-80V | 1 | 0.65 | 1,749 | 0.83 | 2.21×10^7 |
| Total | 123/153 | 80.39 | 159,362/211,537 | 75.34 | 2.01×10^9 |

Table 7.1.: Processed runs with nominal and reduced high voltage settings. For the analysis of the reduced high voltage settings a smaller number of runs was used. In the table, one chunk corresponds to 10k events per run, which are equivalent to 12.6k Krypton decays.

7.2. Analysis Strategy

Tuned for the specific operation environment, the analysis is subdivided into two major parts: The ^{83}Kr cluster finder algorithm, performed on the CERN GRID, and the fit analysis, executed on the batch farm of the *Gesellschaft für Schwerionenforschung Darmstadt* (GSI). In the following, these steps are briefly summarized.

1. The ^{83}Kr Cluster Finder

- a) At the time of data reconstruction the required amount of 50 TB of free disk space was not available on the file system at GSI, which is connected to a batch

farm. Thus, it was decided to develop software, which is capable of running on the CERN GRID environment. For this purpose, a modified version of the Krypton cluster finder macro [39], was developed. The Krypton cluster finder was applied after the global reconstruction (chapter 7.1) and searches for clusters in the TRD. Passing certain criteria (chapter 7.3) these clusters were then assigned to Krypton decays. In addition, a job description file, a validation script, an executable file, and a command file were developed and modified to match the required structure of the GRID. For this reason, the user must follow the hierarchical structure demanded by the framework: The job description file is submitted on the GRID by the user and calls the executable on an automatically assigned computing centre, which in turn calls the command file and the Krypton cluster finder macro. After the processing of the macro finished, the validation script checks for the correct output format of the analysis. If it does not find the output, the job is flagged as 'failed', and a text file for debugging of the error is produced. If the job succeeded, the output is written to the directory of the user. After analysis with the developed cluster finder, the data size was reduced to ≈ 5 TB. More details on the algorithm of the ^{83}Kr cluster finder is presented in section 7.3.

- b) As a last step of the first stage performed on the GRID, the data chunks were merged into fewer files per run. Also for this purpose the necessary scripts and macros were produced. This step was necessary to reduce the number of data files, so groups of 40 output files were merged into one and transferred from the GRID to the GSI file servers. Any higher number of output files to be merged would have caused instabilities in the algorithm.
- c) The last two steps, the merging of the remaining output files into one run and the merging into a single output file for analysis, were carried out on the GSI Batch Farm. As an output, a single file in root tree format was produced. In this file, an individual histogram containing the Krypton decay spectrum is filled for each chamber and each pad individually.

2. The Fit Analysis

- a) As described in section 7.4, each pad spectrum of the output file was fit with a reference spectrum. For this purpose a new fitting algorithm for the determination of the relative gain factor for each pad was developed, containing a robust algorithm to locate and remove broken chambers, broken pads and invalid fits from the analysis.

As explained in chapter 7.6.2, beginning with no information on the relative pad gain, the first analysis step determines the pad gains of a chamber. These are then normalized to the chamber average, which is calculated from the arithmetic mean of the pad gain factors in that specific chamber. A subsequent reconstruction and analysis of the data using the updated pad gain factors further corrects them. In principle this analysis converges to the optimal value until the new gain corrections are of the same order as the uncertainties of the analysis, which are less than 2 % (chapter 7.7). This is the case after only two iterations. In addition each iterative step is a cross-check of the previous one, because a

significant deviation from the already applied gain factor would indicate potential mistakes in the analysis. The individual steps of the Krypton cluster finder algorithm are presented in Fig. 7.1.

As a last step, after the final output is produced, the relative pad gain factors are converted into a special format and made available in the offline condition data base to all users. They are also converted into online gain tables, which are then available for download into the FEE of the ALICE TRD (chapter 4.2.3).

7.3. The Krypton Cluster Finder Algorithm

The main part of the Krypton cluster finder was developed in [39]. This algorithm was applied after the global data reconstruction with the TRD standard cluster finder. The aim of this additional cluster finder is to assign recorded TRD clusters to individual Krypton decays. Because the properties of a ^{83m}Kr -decay electron are different from clusters generated by particles originating from collisions, the algorithm is tuned specifically on the decay properties of ^{83}Kr (chapter 5). For example, a charged particle produced in pp or PbPb collisions deposits only a small fraction of its total energy within the range of up to seven pads and passes all layers of the ALICE TRD, whereas the decay electrons deposit their complete energy within the range of up to two pads and time bins (see chapter 5.2) in a single chamber. A schematic drawing of the working principle of the ^{83}Kr cluster finder is shown in Fig. 7.2. Here, clusters detected by the TRD standard cluster finder are drawn in red. The reconstructed ^{83}Kr decay is assigned to the pad with the largest energy deposition (green point), in this picture located centrally. Thus, using Monte Carlo simulations [39], the Krypton cluster finder was specifically adapted as follows:

- Use the output of the TRD standard cluster finder as input for the developed ^{83}Kr cluster finder.
- Apply noise cuts (see chapter 7.3.1).
- Find the TRD cluster with the highest signal per event in a single pad of an individual chamber.
- According to the ^{83}Kr properties, search in three dimensions for further TRD clusters. That means clusters in the two adjacent rows and columns surrounding the primary cluster, and the clusters found in the adjacent 20 time bins ($2\ \mu\text{s}$) are considered.
- Sum up the ADC counts of the found TRD clusters and assign the collected signal as a single ^{83}Kr decay to the pad with the maximum energy deposition.
- Write the number of decays as a function of pulse height into a histogram for each pad and chamber respectively for further analysis.

7.3.1. Noise Analysis

Fig. 7.3 displays the ^{83}Kr decay spectrum reconstructed in a chamber (0-0-0) before and after noise cuts. Without cuts, the Krypton spectrum is polluted with exponentially decreasing noise, especially large in the range between 0 to 100 ADC counts. In the upper

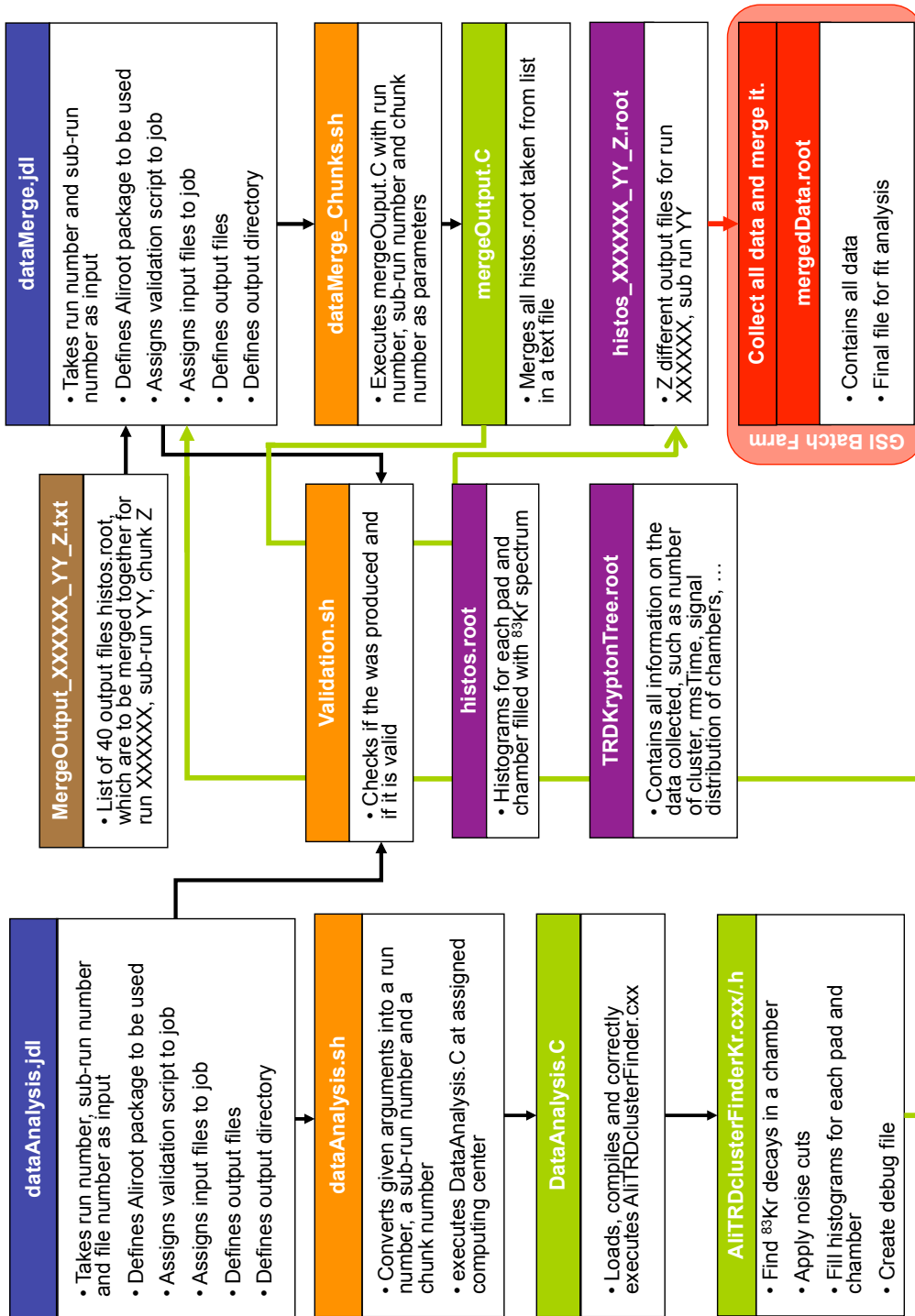


Figure 7.1.: Flow chart of the Krypton cluster finder. Job description files are marked in blue, shell scripts in orange, C++ scripts in green and output for analysis in purple. The last step, which is placed in the red shaded area, was executed on the GSI Batch Farm.

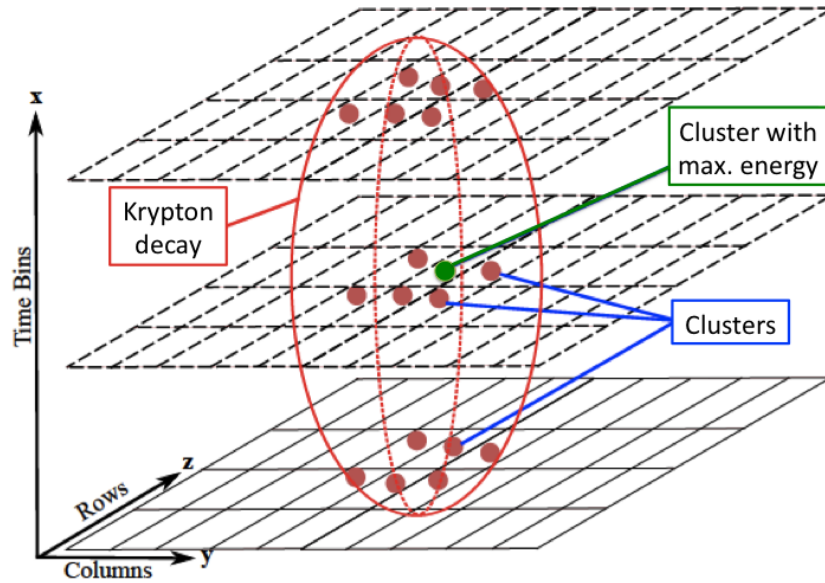


Figure 7.2.: Visualization of the working principle of the ^{83}Kr cluster finder. Clusters are shown as red points, and are assigned to a single ^{83}Kr decay, located on the pad with the most energy deposition (green point), here positioned centrally.

plot, only the decay peak at 41.6 keV is visible around 2500 ADC counts. In the lower plot the effectivity of the noise cuts is clearly visible, as only single counts are visible outside the pulse height region of the Krypton decay. After noise reduction, a clean Krypton spectrum with three decay peaks is visible, corresponding to a deposited energy of 12.6 keV around 800 ADC counts, 29.0 keV around 1700 ADC counts and 41.6 keV around 2500 ADC counts. Note, that in both plots the axis range of the abscissa was reduced for simplicity to 4500 ADC counts respectively.

Two sources of noise mainly contribute to the pollution of the Krypton signal, namely *pedestal* and *pick up noise*:

- **Pedestal noise:**

All electronic circuits suffer from electronic noise, a random fluctuation in an electrical signal. Its structure and strength are of various forms because the source is multilateral. Large contributions come from thermal noise and shot noise, however, many other types are caused by manufacturing quality or semiconductor defects and are related to the individual components of the electric circuit respectively.

- **Pick up noise:**

All electronic devices need to have a reference potential for absolute measurement of voltages, which is called *ground* [48]. Generally, for this purpose a direct connection to the physical earth, as infinite source of charge with constant potential, is used, but a common return path for electric current serves this purpose as well. In case a significant resistance of the ground connection exists, the assumption of "infinite charge and potential" is no longer valid, resulting in stray voltages or potential rise

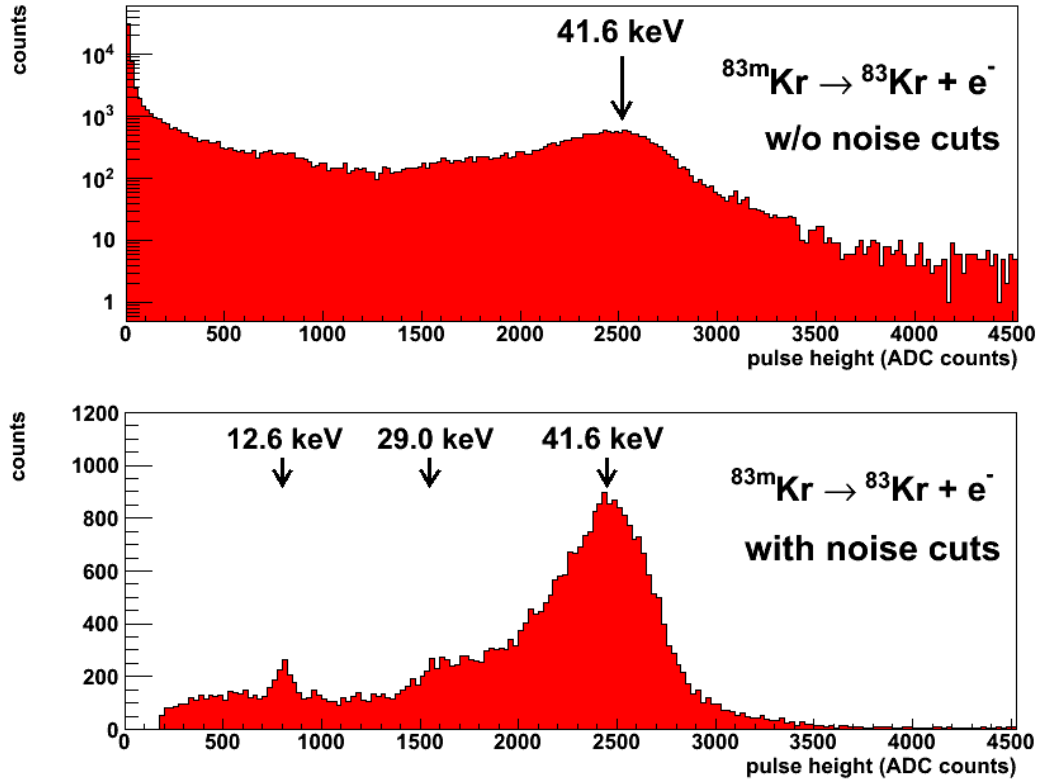


Figure 7.3.: Shown are two Krypton decay spectra reconstructed in chamber (0-0-0) without (top) and with (bottom) noise cuts. The spectra were extracted from two different, very small data samples of 0.02 % of the total statistics.

effects, which create this sort of noise.

By analyzing the collected data in a specific file of the analysis, the amount of noise is completely removed by appropriate cuts. As the *shot noise* is visible as large number of channels with signal above threshold in single events, a cut on the number of clusters per event is performed. In Fig. 7.4 the random relation between number of found clusters and the event number is shown for a single chunk of data, containing 10k events. With a cut on the number of cluster at 1000 entries, the shot noise is completely removed.

The cuts to remove remaining thermal and pedestal noise are more complex. However, as already shown in [39] they prove to be essential for a clean identification of the ^{83}Kr spectrum. As the pedestal noise is randomly distributed in time and found mainly at low energy deposition, it is completely removed by a two-dimensional cut on the root mean square (RMS) time and the signal in ADC counts. A Krypton decay has a defined time distribution depending on its size and energy deposition, thus the root mean square time, which in this case is the arithmetic mean of the squares of the measured time bins, should be located at larger values with larger energy deposition in contrast to the pedestal noise. This type of noise is randomly distributed in time, thus found at low values of the RMS time for low energy deposits. As visible in Fig. 7.5, where the RMS time is plotted against the ADC counts for a given chunk of data, the largest amount of noise is found around

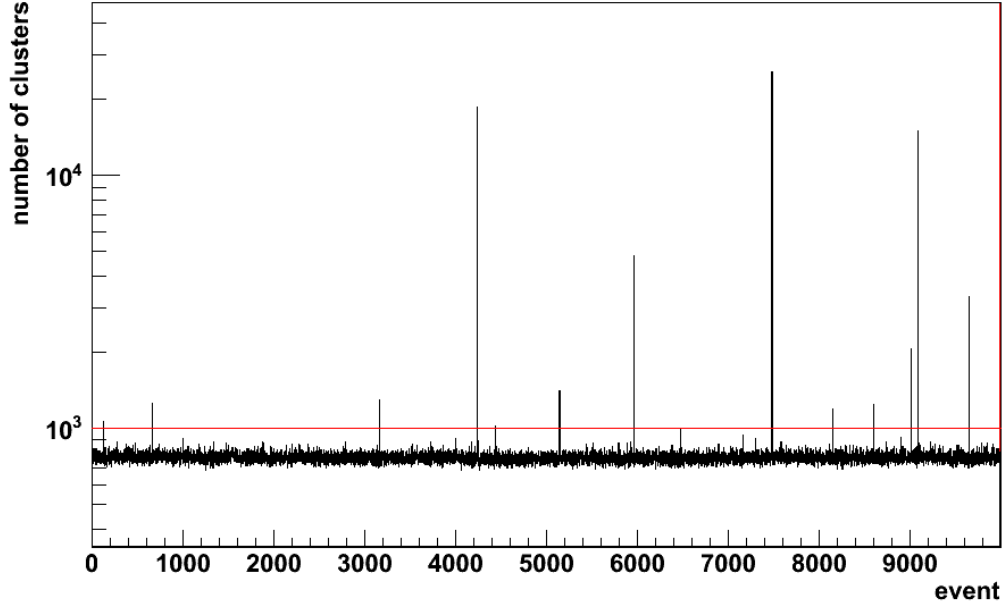


Figure 7.4.: Example of shot noise. Shown is the number of Krypton decay candidates per event in a data chunk of 10k events before cuts. Polluted events are clearly identified, e.g. around event number 4200. To remove the shot noise, a threshold cut on the number of clusters at 1000 counts (red horizontal line) is performed.

0.4 time bins and below 200 ADC counts. Table 7.2 displays the applied noise cuts, which are indicated by red lines in Fig. 7.5.

| Cut Type | |
|---------------------|---------------------------------|
| Threshold Event Cut | 1000 counts/event |
| Cut in RMS Time | $f_1(x) = 1 + 3/3,500 \times x$ |
| as a Function of | $f_2(x) = 5/1200 \times x$ |
| Pulse Height | $f_3(x) = 0.5$ |

Table 7.2.: Applied cuts in the Krypton cluster finder. The threshold event cut is visible in Fig. 7.4. The RMS time cut as a function of the pulse height is given in units of time bins. 'x' is the pulse height in units of ADC counts. These three cuts are indicated as red lines in Fig. 7.5.

These noise cuts were already determined in the previous Krypton calibration [39] and adjusted to the current datasets, i.e. because the pedestal noise was found at higher values of the RMS time, thus the threshold cut on the RMS time was increased to 0.5 time bins. After all, about 60 % of the counts reconstructed in the spectra region in the range of 0 to 8000 ADC counts were removed by the noise cuts.

The effectivity of the noise cuts is visible in Fig. 7.6, which shows a spectrum recorded in a single pad of chamber (0-0-0). At large pulse height above 4000 ADC counts, the spectrum is almost empty (36 counts), thus the noise level was reduced to less than 1 %. The lowest Krypton decay peak at an energy of 9.6 keV because it was polluted by too

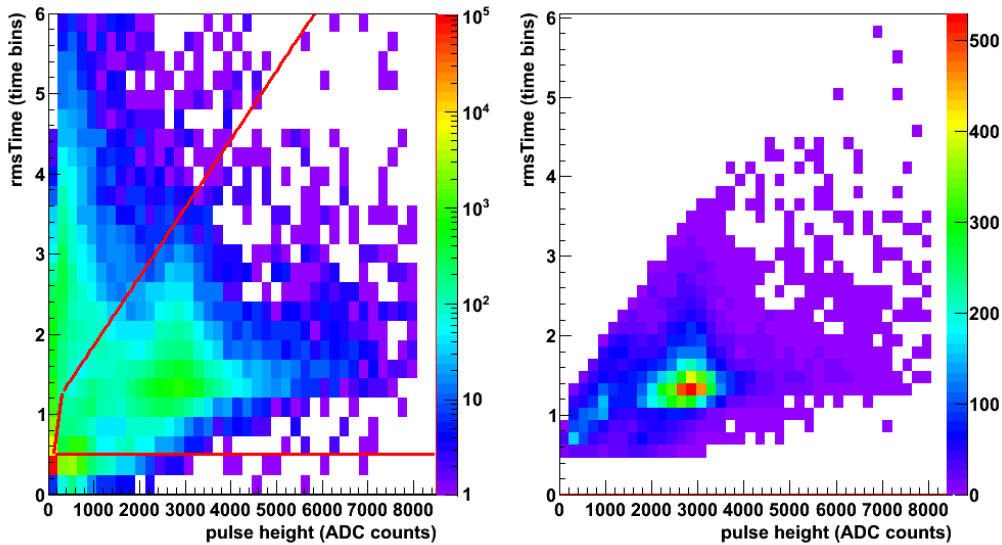


Figure 7.5.: Signal distribution as a function of the root mean square time and ADC counts. After the cuts (red lines) are applied to the data (left), the ^{83}Kr main decay peak at 41.6 keV becomes clearly visible around 2500 ADC counts (right). In addition the 9.4 keV and 12.6 keV peaks are identified around 300 and 900 ADC counts respectively.

much noise. The peak like structure around 300 ADC counts is a relict of the slope of the RMS time cut as a function of pulse height, which leads to increasing number of counts with increasing pulse height. At low pulse height the exponential noise and the pedestal noise below the threshold of 100 ADC were removed. The abscissa was extended to 8000 ADC counts because some chambers showed very high gain, and thus all data appeared within the histogram range.

7.4. Fit Analysis

In the 2010 ^{83}Kr calibration campaign, a Gauss fitting algorithm was used to fit the prominent peak at 41.56 keV of the Krypton spectrum. This method turned out to be rather sensitive to the fitting range and did not specifically treat chambers and pads which were broken or showed low gain, due to reduced anode voltage. In addition, statistics above 1000 Krypton decays in each pad was necessary to perform the Gauss fit, because only the statistics within the fitting range of the main ^{83}Kr decay peak at 41.56 keV was taken into account for the analysis. In the previous calibration [39], about 6000 Krypton decays per pad were found. In the 2011 calibration campaign on average up to 1500 Krypton decays were assigned to the individual pads, however, some pads showed statistics as low as 500 Krypton decays per pad. Therefore a new algorithm, which uses all available information of the spectrum, such as the shape, was developed. If a chamber or pad is identified as broken, not functioning correctly or if the fit did not converge to good results, the specific pad gain factor was set to the chamber average (default), except for the cases where the pad has been calibrated before. In these cases, the gain factor of the previous calibration

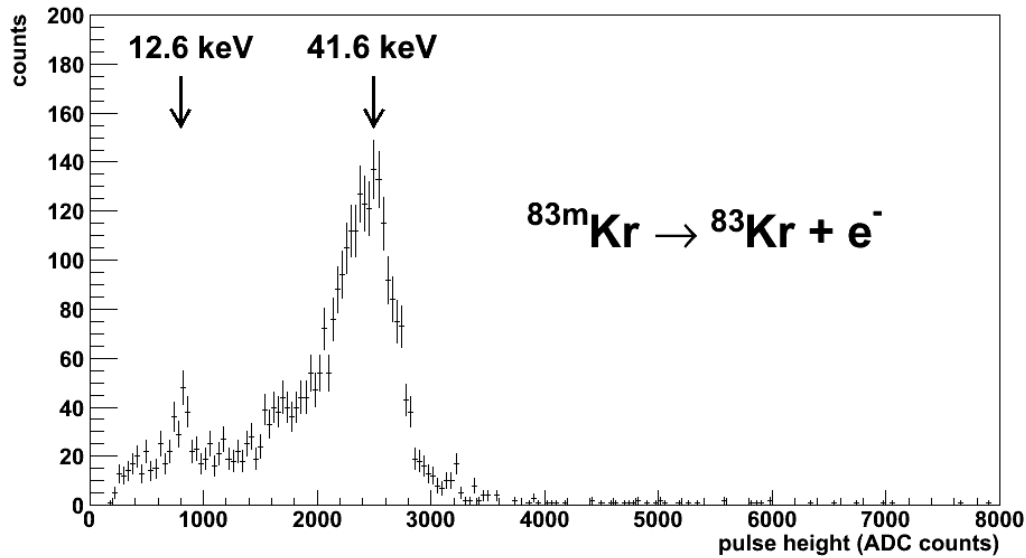


Figure 7.6.: Krypton spectrum reconstructed with the second dataset and assigned to the pad in row 00 column 080 in chamber (0-0-0). Noise was reduced to less than 1 % and two decay peaks are clearly visible around 800 and 2500 ADC counts.

from 2010 was loaded from the offline condition database. Details on chambers and pads not included in the analysis are presented in chapter 7.6.4. The analysis of the pulse height spectra followed the following steps:

1. In a first step broken chambers (chapter 7.6.4) were filtered out for a separate analysis.
2. Identified broken pads (chapter 7.6.4) were set to '0' gain.
3. For the actual fit a reference spectrum with high statistics and a clean spectrum was selected. In this analysis, the reconstructed spectrum of chamber (0-0-0) (Fig. 7.10) was selected, as it is located at the beginning of the gas flow resulting in high statistics and was calibrated before [39].
4. The analysis of pads in chambers which had too little statistics (≈ 400 Krypton decays per pad) were modified such, that the counts of three adjacent pads in a column were summed together. The relative pad gain factor found for this spectrum was then applied to all of these three pads.
5. The reference spectrum was then fit to the individual pad spectra. Before processing, both histograms, the reference and the pad candidate, were normalized and set to similar binning, and two fit parameters were initialized. The first parameter accounts for the change of overall normalization, because the pads showed different amount of entries, whereas the second parameter dilates the pad spectrum to the reference spectrum. This dilation corresponds to the gain factor of the given pad. An example is shown in Fig. 7.9, which is discussed in detail in chapter 7.5.1. The applied fitting algorithm is highly effective because it uses all available information of the decay

spectrum, such as shape, size, position of the decay peaks and especially includes the complete statistics of the spectrum at all ADC counts. To optimally tune the algorithm and to ensure stable fitting conditions, the standard peak finder [49] of the ROOT analysis framework was used to find the main peak of the reference and the candidate spectrum and to determine their ratio as a first estimate of the dilation factor.

- Next, pads with failing fits or which were flagged with '0' gain in step 2, were re-analyzed. Depending on the pad position in the chamber, the pad gain factor was set to the arithmetic mean of its surrounding pads, thus the smoothing algorithm takes the development throughout the geometry of the pad plane into account. The working principle of the smoothing algorithm is shown in Fig. 7.7. Problems arising from differences in the individual pad capacitance cannot be treated specifically, but are corrected through this algorithm as well. This solution by smoothing was also carried out for all pads located in the first three or last three columns within a single pad row, because here the ^{83}Kr cluster finder is not applied, as it would neglect the chamber edges. Thus no counts were assigned to these pads. In order to set them to a meaningful gain value, they were set to the arithmetic mean of the gain factor in the first valid pad column. Pads positioned at the chamber edge in the first and last pad row, were set to the arithmetic mean of the gain factors in valid pads of the adjacent row. If a pad is located anywhere else within the chamber, it is set to the arithmetic mean of its surrounding pads.

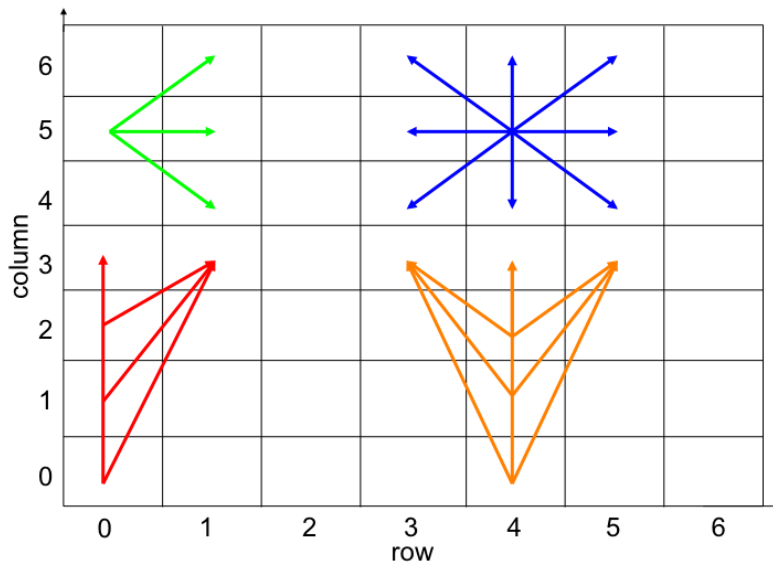


Figure 7.7.: Schematic view of a 7x7 segment of the pad plane, without pad tilt. Depending on the pad location, the gain factor is corrected as follows: Pads located in the first three columns are set to the arithmetic mean of the gain factor in the first valid pad column (red and orange). Pads positioned at the chamber edge, in the first and last row, are set to the arithmetic mean of the gain factors in valid pads of the adjacent row (green). If a pad is located anywhere else within the chamber, it is set to the arithmetic mean of its surrounding pads (blue). The algorithm is correspondingly valid for pads located in the last three columns.

7. Finally, after all applied corrections and smoothing, the average gain factor per chamber was determined as the arithmetic mean of all pads within a chamber. This was chosen since all pads should equally contribute to the chamber average independently of the fit quality.

The final relative gain factor assigned to each pad is defined as $G = \Delta G / G_{\text{Chamber}}$. Relative gain factors outside the region of 0.5 to 1.5, which compares to five times the RMS of typical pad gain distributions in individual chambers, were set to the average gain of the chamber, as they are caused by bad fits or broken pads. Bad fits occurred, because in rare cases the root peak finder was not able to determine the correct position of the main decay peak and thus the initial parameter passed to the fit algorithm was not a good estimate. In these cases the fit did not converge. This approach was chosen, because setting these broken pads to other values would bias the calculation of the chamber mean.

7.4.1. Fit Quality

A first quality check to ensure the goodness of the fit is applied directly after the analysis by evaluating the reduced χ^2 -distribution, which is shown for the analysis of the first dataset in Fig. 7.8. It underlines the high quality of the fitting procedure: The main peak is located around $\chi^2/dof = 1.15$, where the mean number of degrees of freedom was 100. The p-value is ≈ 0.072 , meaning that the difference between compared spectra is not considered as statistically significant by conventional criteria. The p-value is the chance of obtaining a certain finding if the null hypothesis is true. In all fits, data points above 5000 ADC counts were not considered because they would significantly bias the distribution to better values.

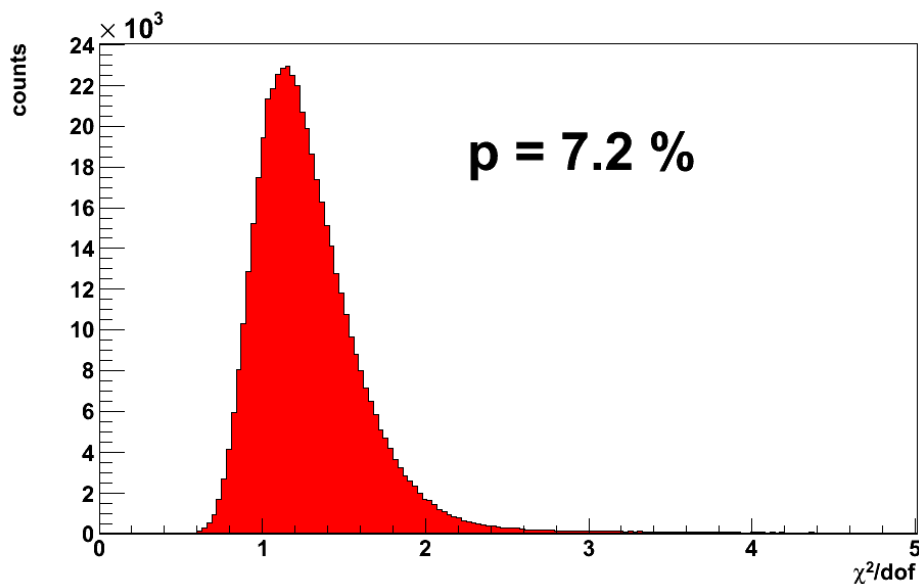


Figure 7.8.: χ^2 -distribution divided by the degrees of freedom (dof) of the fit with the reference spectrum. The peak is located at 1.15.

For the fit algorithm, a statistical uncertainty of better than 1 % was found, despite the

fact that not all available data was available for processing in a single step. However, as determined in chapter 7.7, the fit algorithm returns similar results as a Gauss fitting algorithm on summed pad spectra, which has a statistical uncertainty of the order of 1 %.

7.5. Spectra Analysis

In this chapter the spectra recorded in pads and chambers will be explained with representative examples. In addition, an analysis of the energy resolution, the energy linearity and the gain dependence on pressure changes will be discussed.

7.5.1. Spectra recorded in Pads

A typical Krypton decay spectrum recorded in a single pad with the fitted reference spectrum of chamber (0-0-0) is visible in Fig. 7.9.

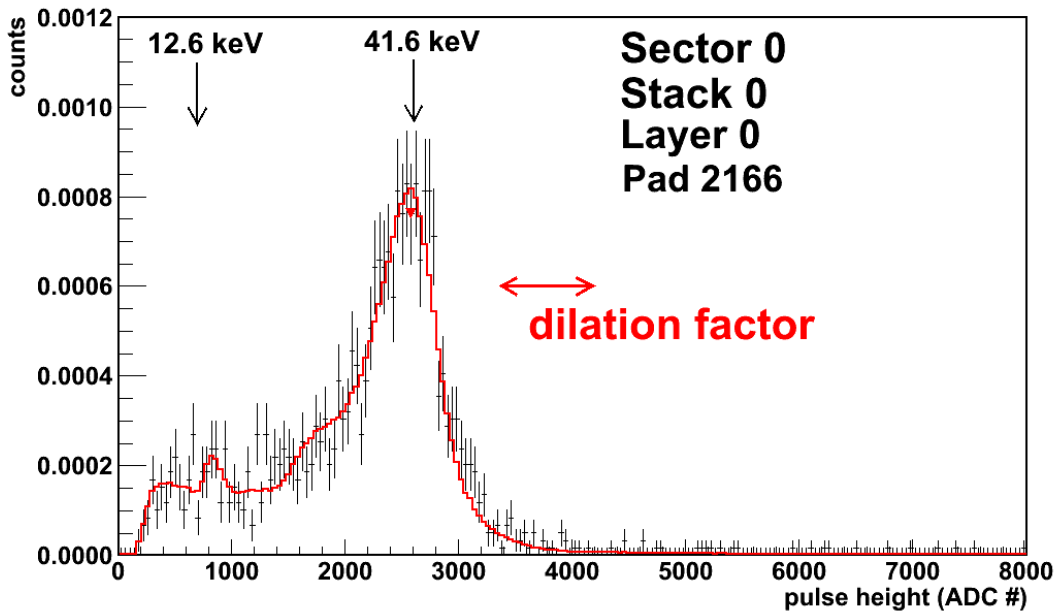


Figure 7.9.: Krypton decay spectrum of chamber (0-0-0) for pad 2166 (row: 15, column: 6). The fit of the the reference spectrum (red) on the data points assigned to the pad (black) using the full information and statistics of the spectra is displayed. Even though there are statistical fluctuation the two spectra compare well with each other. Prior to the fit, the main peak of the reference spectrum was localized around 2500 ADC counts by the standard root peak finder (red triangle).

Here, two Krypton decay peaks are clearly visible around 800 and around 2400 ADC counts, corresponding to the deposited energy of the decay electron of 41.56 keV and 12.6 keV. The 29.0 keV decay peak at 1800 ADC counts is barely distinguishable from the rest of the spectrum, because of too low statistics in this histogram binning. A typical pad spectrum contains about 800-4000 decays, depending on the position of the chamber in the gas cycle of the ALICE TRD. Because of the low statistics in some chambers and to keep the data size for each individual pad at a reasonable size, the 8000 ADC counts

of the abscissa were divided into 200 bins, each bin corresponding to a range of 40 ADC counts. The abscissa range was considered for up to 8000 ADC counts because some pads showed very large gain and thus all data appeared within the histogram range.

Within errors the reference spectrum well describes the pad spectrum in terms of peak position and shape of the rising (around 200 ADC counts) and falling (around 2600 ADC counts) edges of the spectrum. The red triangle around 2400 ADC counts represents the central peak position of the main decay peak found by the ROOT peak finder and was used as a first estimate of the relative peak position when comparing to the reference spectrum.

7.5.2. Spectra reconstructed in Chambers

In Fig. 7.10 a Krypton decay spectrum of one chamber (0-0-0), summed over all pads, is presented. The spectrum was recorded with the second dataset. Because this chamber has been calibrated before [39] the summed spectrum shows sharp peak structures. In addition, chamber (0-0-0) is located at the beginning of the gas flow and thus many decays are recorded, allowing for the identification of four decay peaks around 800, 1200, 1800 and 2400 ADC counts corresponding to a deposited energy of 12.6 keV, 19.6 keV, 29.0 keV and 41.6 keV. To get a better view of the spectrum the abscissa range was reduced from 0-8000 to 0-4000 ADC counts.

This spectrum was used as reference spectrum for the fit described in chapter 7.4. In case of the recorded chamber spectra, statistics would have been high enough for a more detailed binning, however, to keep the total amount of data at reasonable size, the 8000 ADC counts of the abscissa were divided into 400 bins, resulting in a bin width of 20 ADC counts.

7.5.3. Energy Resolution Measurement

The energy spectrum of ^{83}Kr decay is well known with discrete lines, thus the measured Krypton spectrum is convoluted only by the detector resolution. To determine the energy resolution of the ALICE TRD a Gauss distribution was fit to the Krypton main decay peak at 41.6 keV. As done for the method comparison (chapter 7.7), the spectra of three adjacent pads within a single row were added together, because otherwise the statistics in some chambers would not be sufficient for a plausible data handling. On these summed spectra, the standard ROOT peak finder [49] was used to locate the main decay peak and a Gaussian fit was applied. The relative energy resolution was determined from the width σ_{Gauss} of the Gaussian, $\sigma E/E = \sigma_{\text{Gauss}}/\text{mean}_{\text{Gauss}}$. The previously described smoothing was neglected. Fig. 7.11 shows the relative energy resolution of all pads in chamber (16-1-3). The abscissa displays the one-dimensional projection of the two-dimensional pad plane using the following equation:

$$\text{Pad}_{\text{Number}} = \text{Column} + 144 \times \text{Row} \quad (7.1)$$

An oscillating structure dependent on the pad number is observed: Maximum values of the relative energy resolution are located at the chamber edges where the lowest gain is observed, for example at pad numbers 143 or 287. Besides the oscillating structure, a slight decrease in relative energy resolution towards pads at pad number 1200 is observed. This

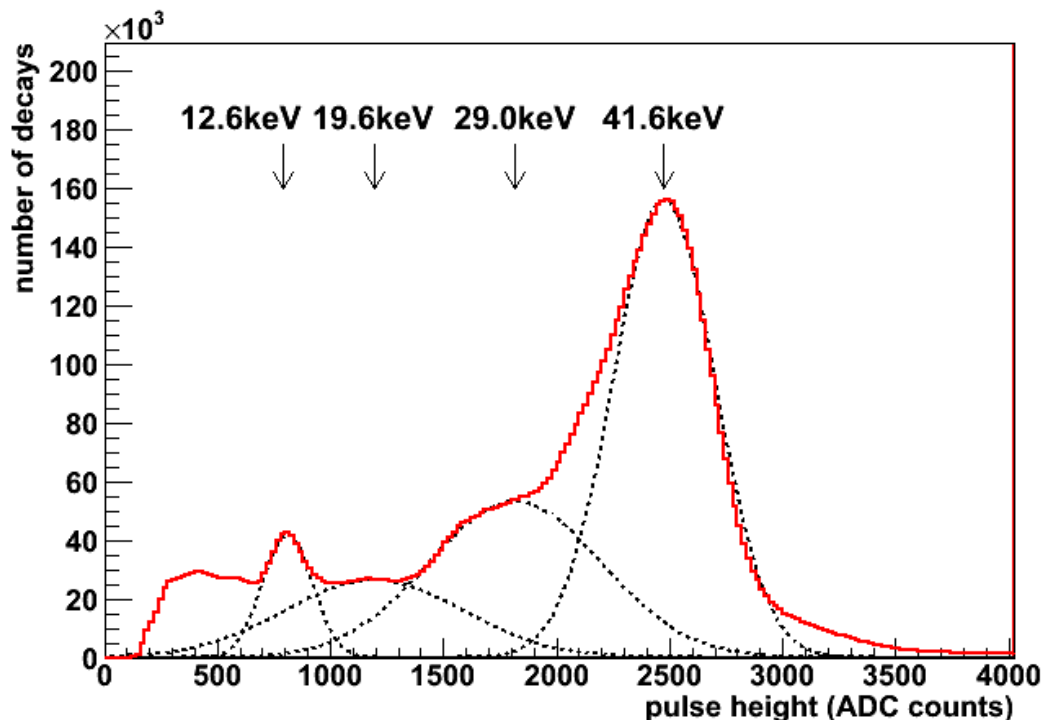


Figure 7.10.: The continuous red line shows the ^{83}Kr decay spectrum reconstructed in chamber (0-0-0). Four decay channels (12.6 keV, 19.6 keV, 29 keV and 41.56 keV) are visible, as emphasized by the Gaussian distributions. This spectrum was used as reference spectrum for the fit analysis.

is understood, because gain and energy resolution correlate with each other. Whenever the gain is highest, the energy resolution improves, because of the corresponding fluctuations in the electric charge.

To estimate the energy resolution of all installed chambers, the arithmetic mean of the relative energy resolution of all pads in each chamber was taken to compute the relative energy resolution of this individual chamber. The mean energy resolution of all chambers is shown in Fig. 7.12, yielding an overall resolution of 10.13 % with a standard deviation of 4.9 %. Single entries are observed around an energy resolution of 16 %. Here, individual broken pads were included in the calculation of the chamber mean, which was strongly affected by these pads, because no smoothing was applied. The found energy resolution meets the design criteria [7] of < 10 %.

7.5.4. Linearity

Another consistency check of the correct functioning of the readout chambers and their electronics is the inspection of the relation between gain and energy of the decay electron. The electronics is designed to have a linear propagation of the signal, proportional to the energy deposition. Thus at least three data points are required for a meaningful fit. From Fig. 7.10 it is visible that three peaks of the Krypton spectrum are easily extractable from the chamber spectra. However, statistics limits the detection of the decay peak at 29.0 keV

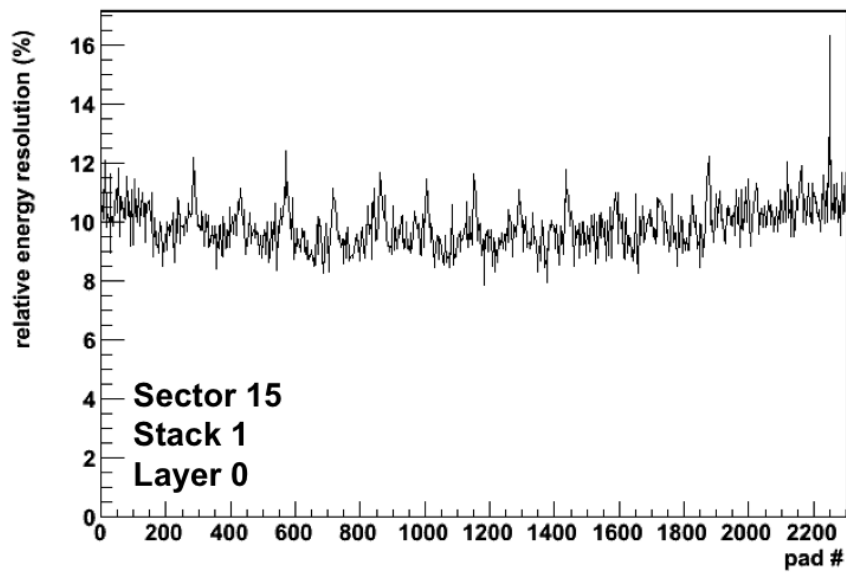


Figure 7.11.: Shown is the relative energy resolution determined with the main decay peak of the Krypton spectrum in chamber (15-1-0) as a function of the pad number. For this purpose, the spectra of three adjacent pads were summed together

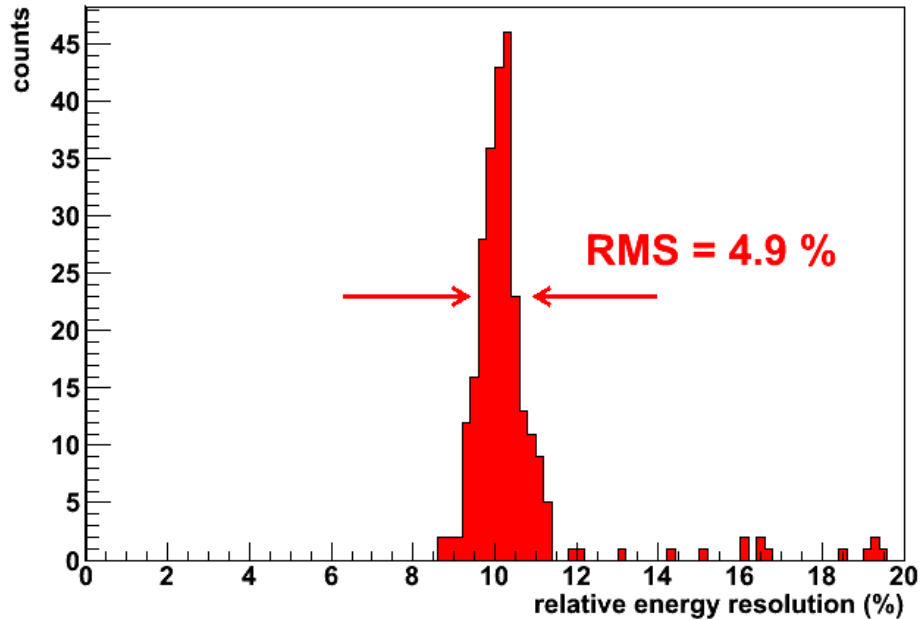


Figure 7.12.: Relative energy resolution of all installed TRD chambers. Each count corresponds to the mean energy resolution of an individual chamber. The overall resolution is 10 % with an RMS of 4.9 %.

in some chambers as well, thus, only chambers in which the peaks at 12.6 keV, 29.0 keV and 41.6 keV were clearly identifiable are used for this analysis. This was the case for about half of the installed chambers. An example recorded with chamber (0-0-0) is presented in Fig. 7.13. The position of the decay peaks was found by fitting with a Gaussian distribution. The pulse height in ADC counts was then assigned to the corresponding electron energy of the decay peak and fit by a first order polynomial function with two parameters, which represent the offset and the slope. In case of the given chamber (0-0-0) the offset and slope were found to be

$$84.98 \pm 0.52 \text{ ADC counts} \quad (7.2)$$

and

$$57.42 \pm 0.02 \text{ keV/ADC counts.} \quad (7.3)$$

Uncertainties are propagated from the fit. As visible in the lower plot, linearity is confirmed better than 6 ‰.

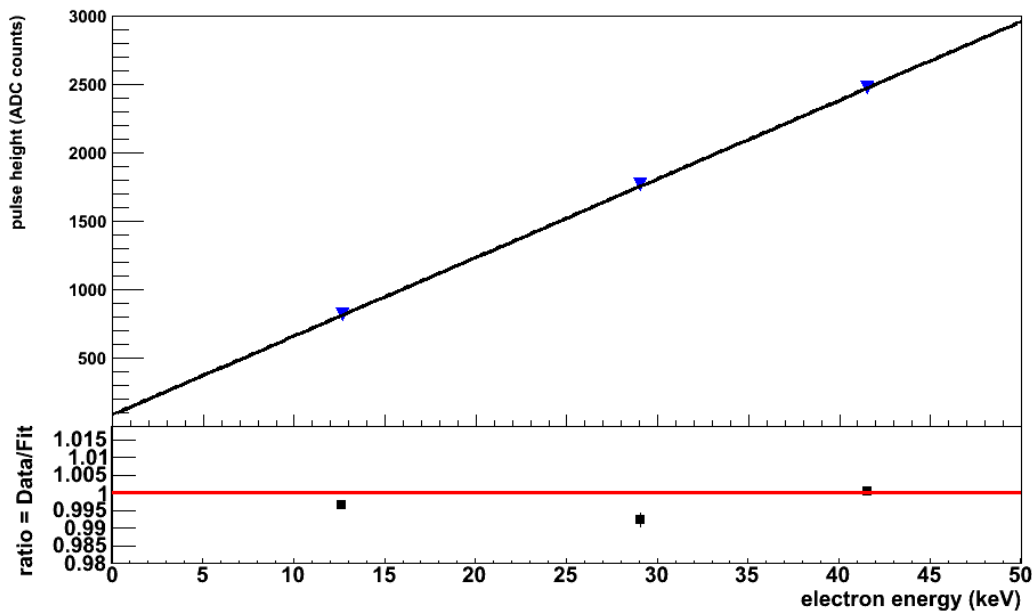


Figure 7.13.: Linear relation between gain and electron energy in chamber (0-0-0), where x corresponds to the decay energy of the electrons in keV. The pulse height was found by a Gaussian fit to the specific decay peak and assigned to the corresponding energy. The errors are propagated from the fit but are negligible small. The black line is the fit result of a linear function to the data points. In the lower plot the ratio of data and fit values is presented. Thus linearity is shown within 6 ‰.

For the 139 chambers included in the analysis, the linear signal processing was confirmed, with an average offset and slope of

$$97.71 \pm 0.64 \text{ ADC counts} \quad (7.4)$$

and

$$67.77 \pm 0.26 \text{ keV/ADC counts.} \quad (7.5)$$

This result shows that the reconstructed signals have linear proportionality to the energy deposition in the chamber medium, and that the electronics correctly propagate this signal without distortions (chapter 4.2.3) in the tested region of 0 to 50 keV, within 6 ‰.

7.5.5. Gain Variations due to Pressure Changes

As already discussed in chapter 2.3.3 the gain has an inverse dependence on relative density changes $d\rho/\rho$ of the gas composition. With equation 2.13 the expected variation of the gain due to changes of the atmospheric pressure is calculated as follows. For this purpose the linear charge density λ needs to be computed, considering the detector parameters given in table 7.3:

$$\lambda = \frac{\epsilon_0 s V_0}{z} = 1.935 \cdot 10^{-8} \text{ C/m.} \quad (7.6)$$

| TRD Parameters | |
|--|--------|
| Distance between Anode Wires s | 5 mm |
| Distance between Anode Wires and Cathode Plane z | 3.5 mm |
| Nominal Anode Potential V_0 | 1530 V |

Table 7.3.: Processed runs with nominal and reduced high voltage settings. For the analysis of the reduced high voltage settings a smaller number of runs was used. In the table, one chunk corresponds to 10k events per run, which are equivalent to 12.6k Krypton decays.

Subsequently, the change of amplification due to relative pressure changes is calculated to be

$$\frac{dG}{G} = -6.03 \frac{dp}{p}. \quad (7.7)$$

Here, the Diethorn parameter ΔV for the gas mixture Xe-CO₂ [85-15] was estimated with 40 V [23]. Fig. 7.14 shows the atmospheric pressure measured in the ALICE cavern as well as the pulse height of the main decay peak in the Krypton spectrum in chamber (0-0-0), as a function of the time they were measured. The cavern pressure was multiplied by negative one for comparability. A Gaussian function was fit to the decay peak of the spectrum reconstructed in chamber (0-0-0) for each run, because it directly yields the gain in ADC counts. Both datasets were used for this analysis (see chapter 7.1). The inverse relation between gain and gas density, which is proportional to the atmospheric pressure, is clearly visible (equation 2.13). Even fine peak structures in the atmospheric pressure distribution, for example between February 6th and 7th, are reproduced by the gain variation. From the plot, the relative pressure changes are estimated, giving: $dp/p = \pm 0.71 \%$. Using equation 7.7, these fluctuations are expected to cause a relative change of gas gain of

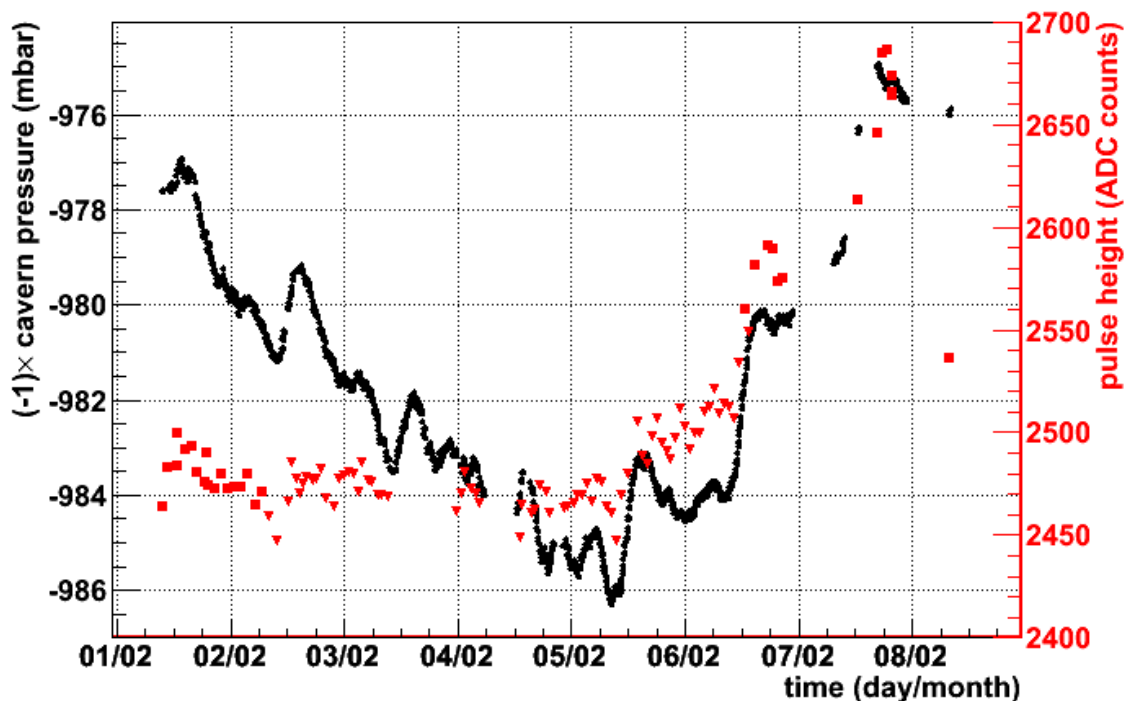


Figure 7.14.: Peak position of the ^{83}Kr main decay peak in chamber (0-0-0) as a function of the time the run was recorded. The red squares were produced with the first dataset. The red triangles display the second set of analyzed runs, for which the newly calibrated gains were loaded. The black circles represent the cavern pressure.

$\mp 4.3\%$. An actual gain variation of approximately $\mp 4.4\%$ is visible in Fig. 7.14, which is in excellent agreement with the predictions.

Even though the gain visibly fluctuates over the time period of the data taking, the change of pressure does not contribute to the systematic error in this analysis. By merging the data recorded in many runs, spread over a long period of time, a smearing of the resulting ^{83}Kr spectrum is visible in the pad and thus the chamber spectrum. However, because the pad gain factors are calculated relative to the chamber average these pressure changes cancel out, because they equally contribute to the numerator and denominator of the calculation respectively and because they are similar for all pads. Even in the case that the actual decay spectrum would be distorted in a way that all decay peaks are shifted by atmospheric pressure changes to lower (or higher) gains for example such, that a single decay peak appears for two pulse heights, would not lead to uncertainties in the fitting algorithm. Again, this is because the reference spectrum and the individual pad spectra are affected in a similar way and would both show this distortion.

7.6. Gain Factor Analysis

In this chapter the distribution of the relative pad gain factors will be discussed in more detail. At first the overall distribution of the relative pad gain factors for all installed

chambers is examined. A close look at the pad-by-pad evolution of the distribution for single chambers with the iterative procedure is presented in the subsequent section. In addition, the relative pad gain factor distribution in single chambers will be discussed.

7.6.1. Gain Factor Distribution of all installed Chambers

The relative gain factor distribution determined with the first dataset as a function of the readout chamber number is shown in Fig. 7.15. Here, for better visibility, the bin width on the abscissa corresponds to the summed distribution of 15 chambers. The color-coding displays the number of pad entries for each gain factor. In each bin of the abscissa, a symmetric Gaussian distribution with the mean at unity is observed. The mean is indicated by the black dots and serves as a cross-check of the correct normalization of the pad gain factors to the chamber mean, which should be unity a priori. The white areas between chamber number 60-209 and 360-449 indicate not yet installed chambers.

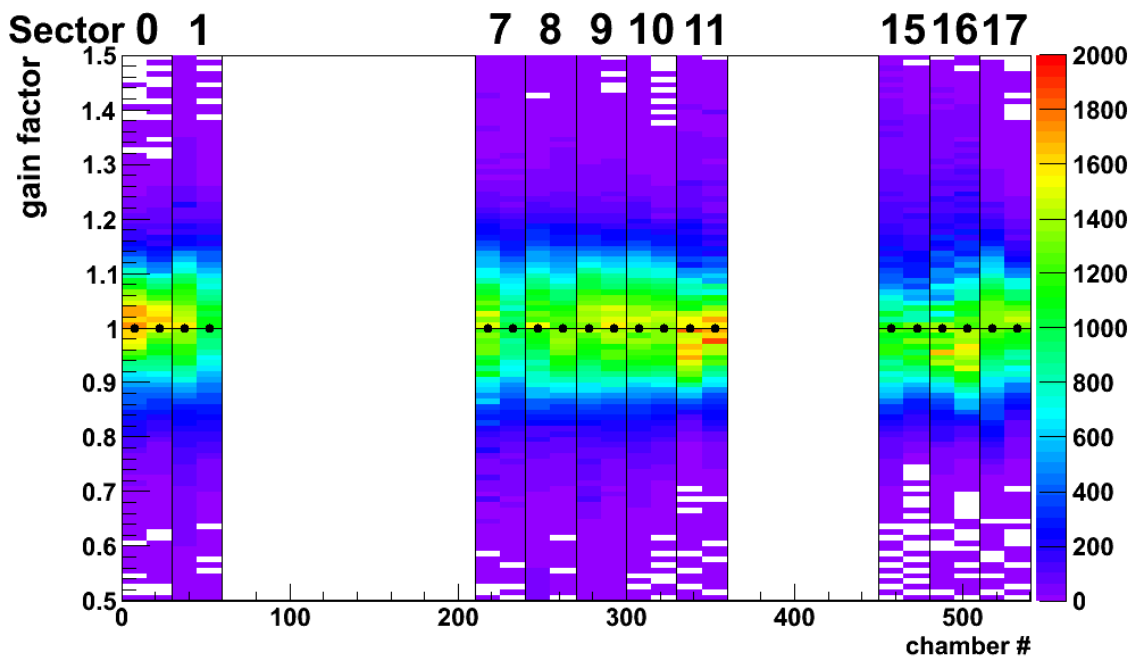


Figure 7.15.: Gain factor distribution in all chambers. The mean of each chamber is drawn as black dots. White areas indicate chambers which are not yet installed.

In Fig. 7.16 the distribution of all pad gain factors from all installed chambers, as determined from the second dataset, is shown. Even though individual chambers show non-symmetric distributions (see chapter 7.6.2), the distribution is symmetric around unity, because the asymmetric distribution are random and thus, even out. Relative pad gain factors outside the region of $0.5 < \text{gain} < 1.5$, which are not presented, are set to default. As mentioned in chapter 4.2.2 gain variations of the order of $7 \pm 3\%$ are expected from the chamber design. With a single standard deviation of 9.1% the design criterium of a maximal gain variation of 15% [7] is met by 91% of all installed pads. 9% of all installed pads are not in the design range. This effect is partially explained with pads located at

the chambers edges, dropping to low gain values so they are not within the desired range. Further deviations are still under investigation.

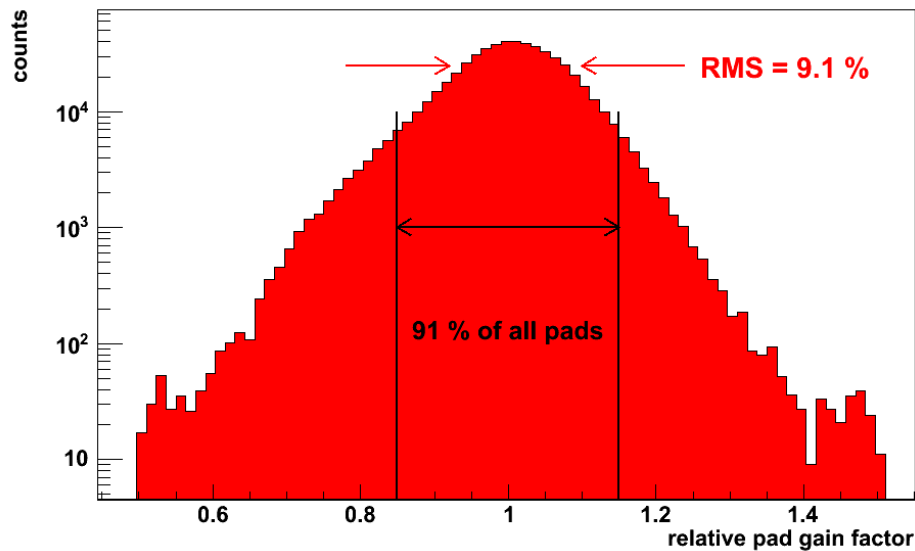


Figure 7.16.: Gain factor distribution of all pads in all installed chambers, except for those with a gain outside the region of $0.5 < \text{gain} < 1.5$, which were set to default and are not shown here. With an RMS of 9.1 % the design criteria [7] are met by 91 % of all installed pads.

7.6.2. Iterative Analysis Steps

Representing all other installed chambers, the iterative development of the relative pad gain factors recorded in chamber (7-0-2) is analyzed for the second dataset. In this context, 'first step' means the total correction, which was already in place prior to the analysis, based on non-calibrated chambers. The 'second step' represents the correction of this previous calibration, found in the ongoing analysis. In Fig. 7.17 the development of the pad gain correction is shown. The distribution of the 'second step'-gain factors was scaled by a factor of 0.1 for good visibility.

Whereas the gain factor distribution of the first step has a single standard deviation of 11.3 % the gain uniformity of the pad gain correction improved to 1.4 % in the second step. The final applied relative pad gain factors are a product of the two values for each individual pad. This chamber is a typical example of the development of the pad gain uniformity. After an iterative step the gain uniformity of all chambers is of the order of 1 %. Further on, it was observed that chambers which were calibrated before in the previous calibration campaign in 2010 showed no significant deviations of the relative pad gain factors. That means, that they were well calibrated and that the calibration is stable at least over a time period of one year. In addition, broken pads and FEE channels are identified.

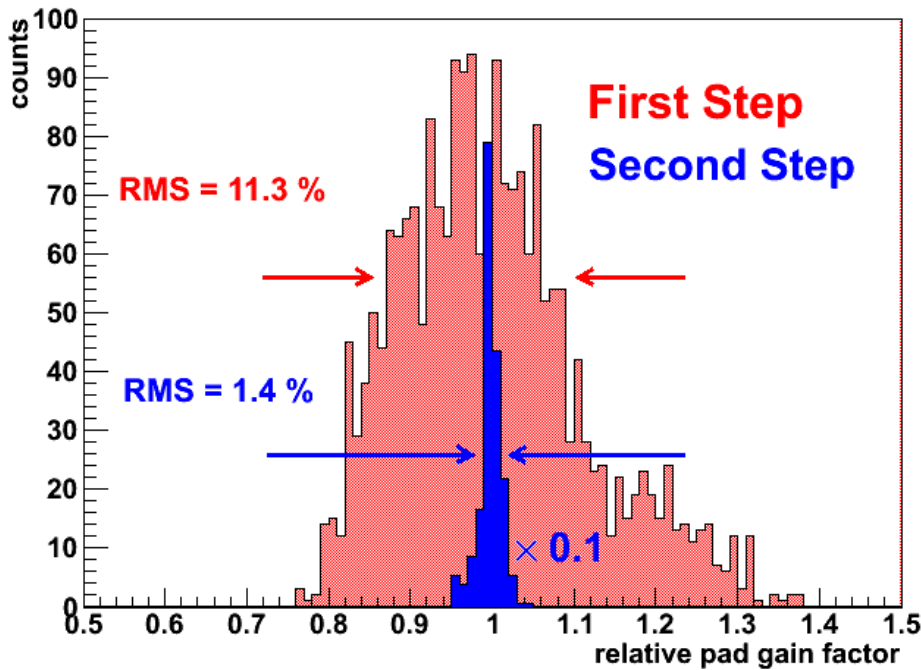


Figure 7.17.: Evolution of the pad gain correction in a chamber. The broad distribution (red) represents the relative pad gain distribution based on a non-calibrated chambers. The distribution of the pad gain correction relative to the previous calibration improves to an RMS of 1.4 % after a second iteration, shown in blue. The distribution of the second iteration step was scaled by 0.1.

7.6.3. Gain Maps of single Chambers

With the analysis of so called *gain maps*, which display the different gain factors for each pad within a chamber, chamber type-specific structures in the pad gain distribution are identified. As described in table 4.1 the pad planes of different chamber types vary in their length and width, and thus for larger chambers a larger sag of the pad plane in the middle is expected. As shown in chapter 2.3.3 slight pressure gradients or small geometrical distortions, such as an outward bending of the pad plane due to overpressure inside the chamber, have strong effects on the gain (see table 2.1). The installation of chambers in the supermodule and eventually the installation of supermodules into the ALICE space frame lead to mechanical stress, which results in small twists and torsions of the initial chamber geometry. Thus, gain variations with smooth variation over the whole chamber geometry is expected. On the other hand the capacitance of single pads and their connected electronics can be different from one another and influence the size of the readout signal, too. This leads to random pad-by-pad fluctuations in the gain.

As not all analyzed chambers can be described within the scope of this thesis, some typical examples are presented in the following, with the main focus on the newly installed supermodules in sectors 11, 15 and 16. All gain maps presented are produced with the second dataset (chapter 7.1). In Fig. 7.18 the gain map of chamber (16-4-2) is shown. The axis are labeled according to the global ALICE TRD coordinate system with respect to

the global ALICE coordinates (chapter 4.4). The color-coding represents the relative pad gain factors. In the pad gain distribution of this chamber of type L2C1 (see table 4.1), a peak in the relative pad gain distribution in the middle of the chamber is observed, which is falling off to the chamber edges. Especially at the high and low end of the ordinate $r\phi$ -axis the gain drops to lower values, however as the wires are mounted parallel to the axis, this decrease is explained by the inhomogeneous electric field at the end of the wire. In addition, the smoothing (see Fig. 7.7) of the pad gain factors at these chamber edges is visible as well. This edge effect is typical for all installed chambers. The central peak structure was commonly found in chambers of the L2C1 type, which indicates that this topology is related to the design and manufacturing process (chapter 7.8). Except for individual pads, i.e. around $z = 20$ cm and $r\phi = 0$, the design criteria of gain variations of less than ± 15 % over the whole chamber are met.

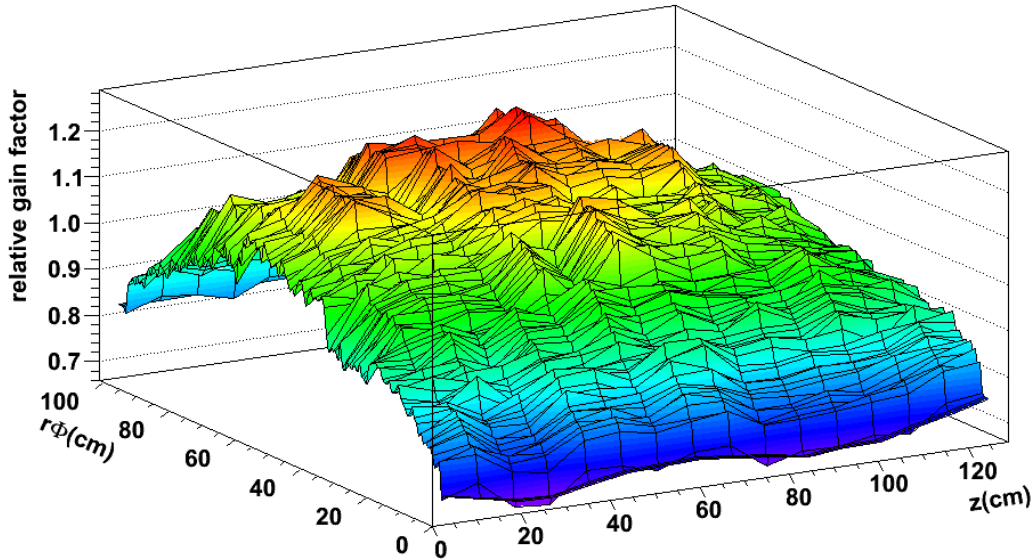


Figure 7.18.: Gain factor distribution of all pads in chamber (16-4-2). A peak of the gain factor distribution in the middle of the chamber is observed, decreasing smoothly towards the chamber edges. The topology is common for chambers of type L2C1.

In Fig. 7.19 the gain distribution of chamber (15-1-0) is presented. In contrast to the previously shown gain map, an asymmetric structure is observed. Pads around $z = 80$ cm and $r\phi = 25$ cm have the lowest gain within the chamber, whereas the highest gains are observed in the rows around $z = 10$ cm. Generally, no common structure was observed for chambers of similar type (L0C1). However, as presented in the comparison to measurements performed during chamber construction (chapter 7.8), good agreement was found between the two measurements, indicating that the chamber geometry was not influenced by outside effect, i.e. from the installation in the supermodule and the orientation of the supermodule in the space frame. These variations are caused by the mechanical tolerances of the chamber construction and by a pressure gradient within the chamber.

These two examples already show, that there is no global structure in the gain maps for all

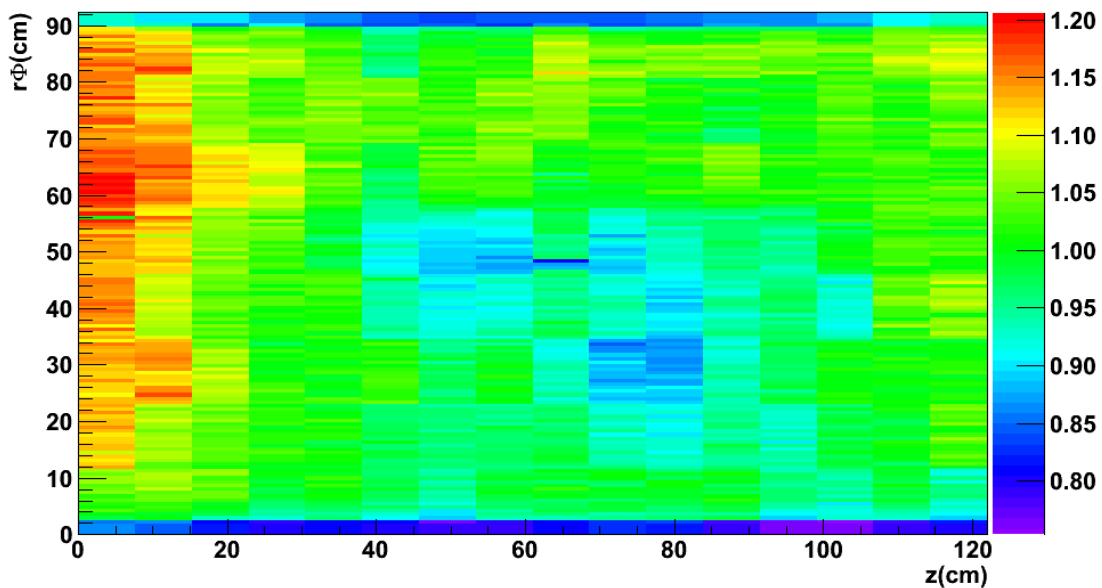


Figure 7.19.: Gain map of chamber (15-1-0). The topology does not appear symmetric. However, as a similar distribution was observed in measurements performed during the chamber construction, these variations are caused by the slight imperfections of the chamber construction as well as a pressure gradient within the chamber.

chambers. Depending on the chamber type, different topologies were observed. However, for some chamber types common structures are found, i.e. chambers of type L3C1 show lower gain factors in the middle of the pad plane of the chamber (chapter 7.8).

7.6.4. Chambers and Pads excluded from the Analysis

Some of the installed chambers showed problems, such as large currents or frequent high voltage trips and were excluded from the data recording. A summary of known broken chambers flagged in the offline condition data base is presented in table 7.4. These chambers showed very low gain or additional noise. The anode high voltage for these chambers was either turned off or reduced. In addition chambers, which did not record a valid and clean Krypton spectrum and were excluded from the Krypton calibration are listed.

| Chamber Status | Number of Chambers Affected | % |
|--|-----------------------------|------|
| Flagged as broken in offline condition data base | 18 | 6.12 |
| Additionally excluded from Calibration | 7 | 2.38 |
| Total number of excluded chambers | 25/294 | 8.50 |

Table 7.4.: Number of chambers excluded from the analysis because they are either flagged as broken in the offline condition data base or no usable Krypton spectrum was obtained.

A detailed list of chambers (not) used in the analysis is given in A.2. Whereas chambers flagged in the offline condition data base were considered broken, the reason for exclusion of

the other seven chambers was found to be either caused by additional noise or too low gain settings, corresponding to reduced high voltage settings.. Fig. 7.20 shows the spectrum recorded in chamber (1-3-2), which was excluded from the analysis. Here, the main decay peak is visible at a pulse height of 2500 ADC counts, but it only contains a few hundred counts. Considering that these counts are distributed over all pads in the chamber, single pads have on average less than one count in the main decay peak and are therefore not suitable for any fit.

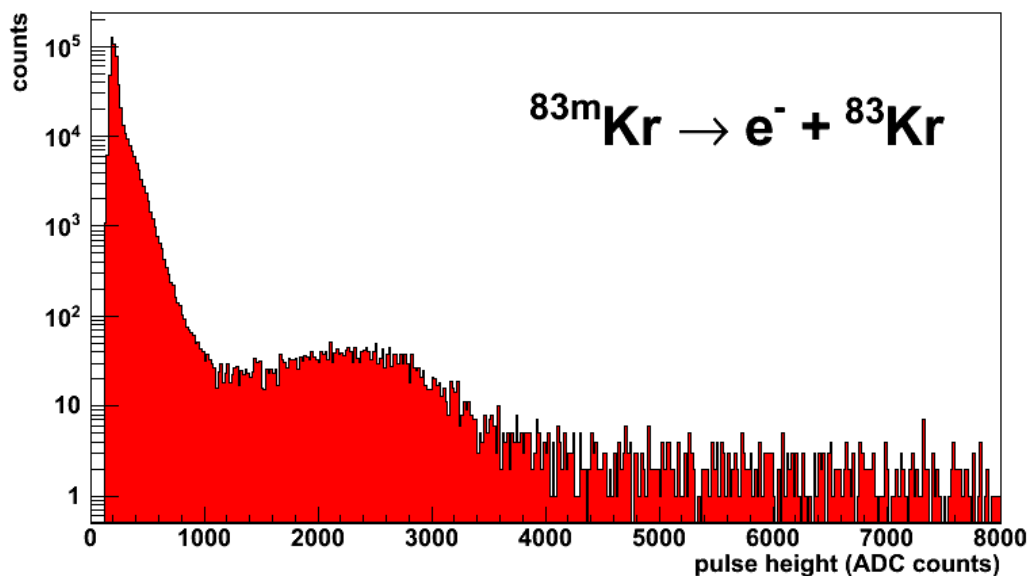


Figure 7.20.: Shown is the spectrum recorded in chamber (1-3-2) which is polluted by noise. Even though a peak around 2500 ADC counts is visible, the spectrum is dominated by noise around 200 ADC counts. The chamber cannot be calibrated, because the individual pads did not record enough statistics in the regime of the main decay peak and additional noise was observed at high pulse heights above 5000 ADC counts.

In addition to the broken chambers there are single broken pads. These pads collected either less than 100 counts or permanently collected large amounts of data which seems not to belong to the Krypton decays. The reason for this behavior is still under investigation. A possible explanation are broken FEE. These pads were excluded from the analysis. A total of 3353 readout pads were excluded from the analysis, which corresponds to 0.52 % of all readout pads in the installed chambers. In this context chamber (15-1-2) is an interesting example. The chamber spectrum is polluted by three floating readout pads, which show strange oscillations at higher ADC counts, as presented in Fig. 7.21. After exclusion of these three pads the chamber was included in the normal analysis strategy.

7.7. Comparison to the previous Method

In order to determine systematic uncertainties, a second analysis based on the old fit algorithm [39] was performed. Here, instead of fitting the reference spectrum to the pad

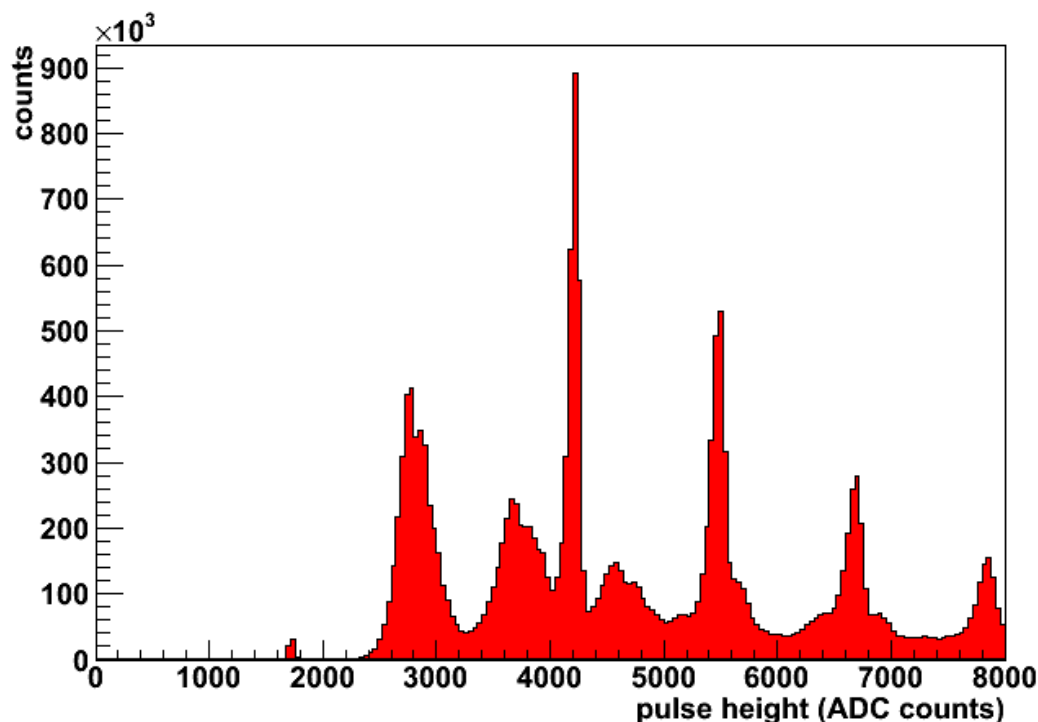


Figure 7.21.: Recorded spectrum of the readout pad in row 09 column 056 of chamber (15-1-2). The pad shows a very high amount of counts, so it can be excluded from the analysis via cut on the maximum number of entries in the spectrum. The origin of the oscillating structure of the noise is under investigation.

spectrum, a Gaussian distribution was fit to the main decay peak in the pad spectrum and the mean determined. The relative gain factor was then calculated by normalizing the mean to the arithmetic mean of the chamber. The spectra of three adjacent pads were summed to achieve a stable fit with high enough statistics 6.4.1. A comparison of the relative pad gain factors in chamber (15-0-3) can be seen in Fig. 7.22. The statistical uncertainty of the Gauss fitting algorithm is of the order of 1 %.

In the upper part of the plot the relative gain factor for each pad is presented as a function of pad number for the old Gauss fitting method (red) and the new spectra fitting method (blue). The oscillating structure originates from the lowered gain values near the chamber edges at the beginning and end of each pad row, because the pad number on the abscissa is a projection of the two-dimensional pad plane of the chamber on the one-dimensional axis, using the equation 7.1.

In the lower plot, the ratio of both fitting methods is presented. Unity is indicated by the red horizontal line. Except of a few outliers at the chamber edges, i.e. around pad number 1800, the two methods quantitatively agree within ± 2 %. A distribution of the obtained ratio from all pads in all chambers is shown in Fig. 7.23.

The distribution is centered around unity with a single standard deviation of 1.8 %. The single standard deviation is used as an estimate of the systematic error for the spectra fitting analysis, which essentially shows that both methods return similar results. Thus, for the new analysis a statistical error of better than 2 % is assumed. For the Gauss fitting

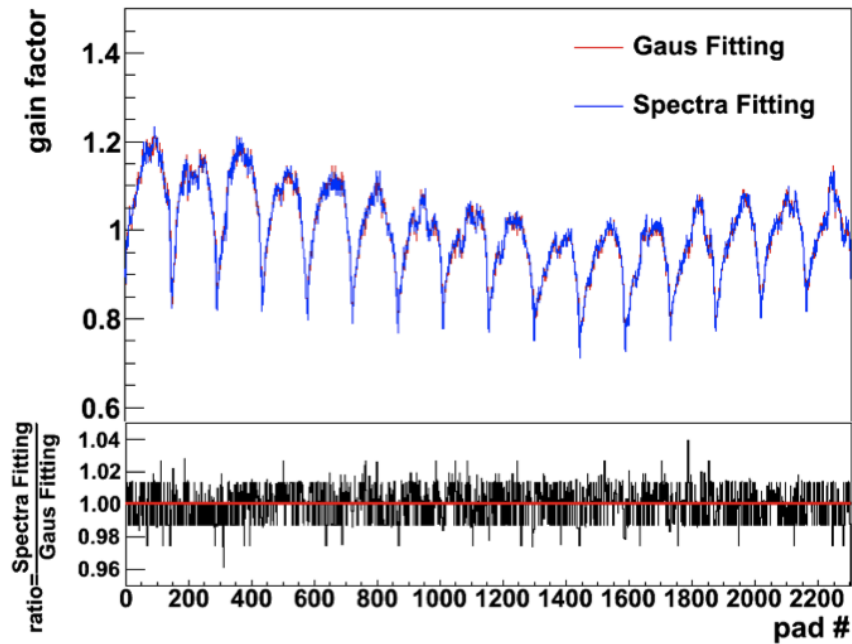


Figure 7.22.: Comparison of the relative pad gain factors found with the spectra fitting (blue) and the Gauss fitting (red) algorithm. The ratio between the obtained fit results is presented for each pad number in the lower plot. Unity is indicated by the red horizontal line. Agreement was found within 2 %.

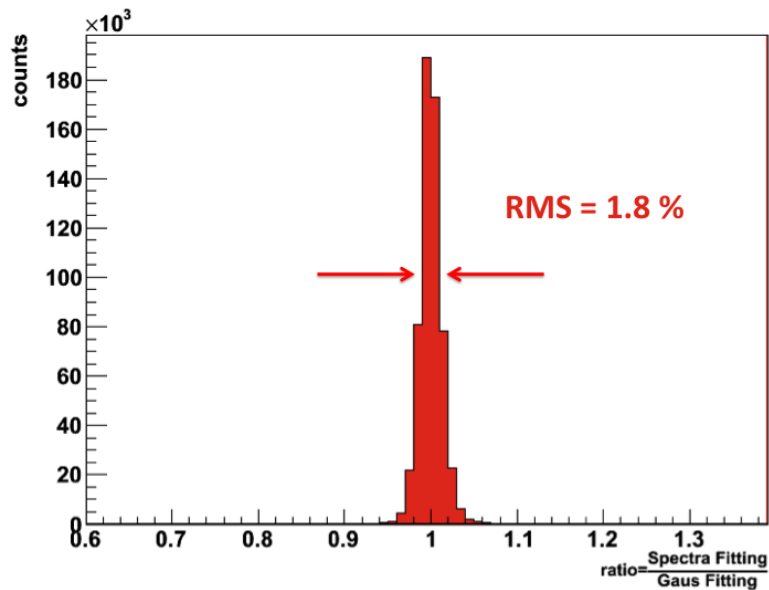


Figure 7.23.: Profile of the ratio of the relative gain factors found with the two algorithms. With the mean at unity, the RMS is 1.8 %.

method the statistical uncertainty is slightly higher than for the Spectra fit. Considering the high fit quality of the new method, as shown in chapter 7.4.1, the new algorithm is

able to deliver good results on pad-by-pad resolution, compared to the 3-pad-resolution of the old algorithm. However, if high enough statistics is available both approaches return consistent pad gains.

7.8. Comparison to Gain Uniformity Measurements

Another useful tool to understand observed topologies and to cross-check the Krypton analysis is the comparison to the standard TRD chamber testing procedure performed during construction [50]. In these tests the chamber is mounted in vertical position and irradiated by a radioactive source. As presented in table 7.5, depending on the construction site, the chambers were irradiated with different probes and the anode current was measured. Individual chamber types were produced and tested at specific manufacturing and testing facilities, which are LHEP Dubna, PI Heidelberg, NIHAM Bucharest and GSI Darmstadt.

| Chamber type | constructed at | Test source | Comparison: Krypton and Test Measurement | | |
|-----------------------------------|----------------|-------------------|--|----------------|----------------|
| | | | no data | poor agreement | good agreement |
| L0C0 | LHEP | X-ray Tube | 2 | 2 | 5 |
| L0C1 | n/a | n/a | 31 | 1 | 8 |
| L1C0 | LHEP | X-ray Tube | 2 | 4 | 3 |
| L1C1 | PI | ^{109}Cd | 5 | 2 | 33 |
| L2C0 | LHEP | X-ray Tube | 1 | 0 | 8 |
| L2C1 | NIHAM | ^{238}Pu | 8 | 19 | 13 |
| L3C0 | LHEP | X-ray Tube | 1 | 0 | 8 |
| L3C1 | NIHAM | ^{238}Pu | 4 | 3 | 33 |
| L4C0 | LHEP | X-ray Tube | 1 | 3 | 5 |
| L4C1 | GSI | n/a | 7 | 12 | 21 |
| L5C0 | LHEP | X-ray Tube | 2 | 0 | 7 |
| L5C1 | GSI | n/a | 3 | 9 | 28 |
| Total (of 294 installed chambers) | | | 67 | 55 | 172 |

Table 7.5.: Shown is a list of chamber types, the location of the chamber construction, the used radioactive source, and comparison results from the two measurements. Note that 'n/a' means that no data is available in the database.

Each chamber was surveyed in a grid of 10 by 10 data points recorded equidistantly over the active detection area. Environmental variables such as atmospheric pressure p , temperature T , anode voltage and gas mixture were set to comparable settings ($p = 1$ atm, $T = 20$ °C) as in the final location in the ALICE experiment. Even though this measurement of the gain uniformity is not carried out with high granularity, it is possible to compare the found gain maps with the ones from the ^{83}Kr calibration. For comparison, the measured anode currents were normalized to the arithmetic mean of the data. Thus not the absolute but the relative gain maps were compared. The results of the measurement performed during construction were extracted from the TRD database.

The three sequential Figures 7.24, 7.25 and 7.26 show gain maps from the two measurements of chamber (16-1-3) of type L3C1 as well as their respective projected profiles.

Fig. 7.24 displays the data points from the measurement performed during construction. ALICE TRD coordinates are used. The color-coding represents the relative gain. As mentioned before, all chambers of type L3C1 have the lowest gain in the middle of the chamber and show the highest gain around $z = 10$ cm and $z = 130$ cm. A sudden drop of the gain at larger values of $r\phi$ at the chamber edge is observed, due to inhomogeneous electric field.

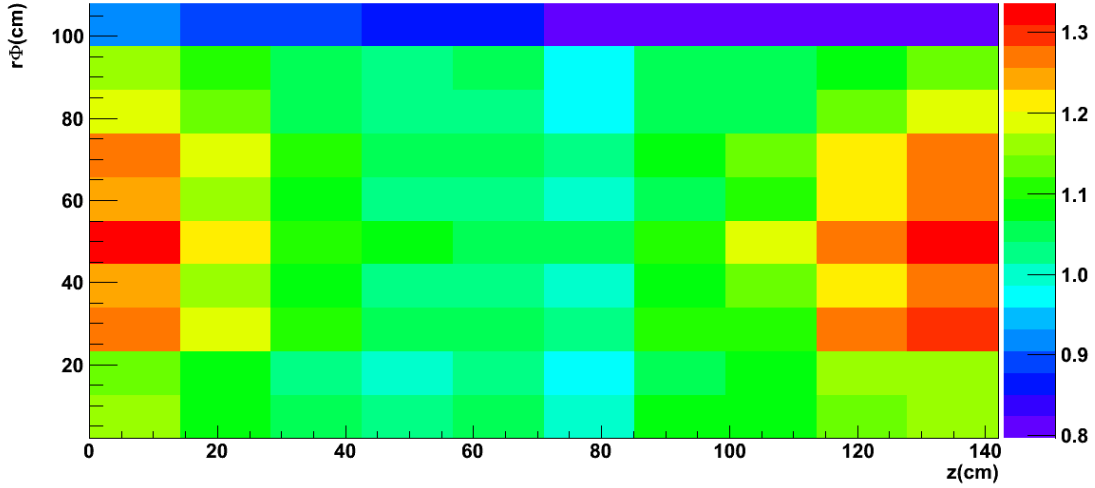


Figure 7.24.: Gain uniformity measurement of the anode current of chamber (16-1-3) performed during construction. The chamber was irradiated with a ^{238}Pu source in a 10×10 mesh. For comparability, the anode current was normalized to the arithmetic mean of all data points in the chamber.

In Fig. 7.25 the relative pad gain measurement of the Krypton calibration is shown for the same chamber. Again, a drop of gain at the high end of the $r\phi$ -axis is observed, and a similar structure is seen at the low end of the $r\phi$ -axis, which was not observed in the other measurement. This is explained by the reduced resolution of the latter one, which does not precisely describe all structures. However, the overall distribution of the gain of the chamber shows good agreement with the other measurement, even though fluctuations in individual pads are observed as well, i.e. at $z = 125$ cm and $r\phi = 40$ cm.

Fig. 7.26 displays a projection of the gain factors in a central slice ($55 \text{ cm} < r\phi < 66 \text{ cm}$) of the $r\phi$ -axis onto the abscissa. For this purpose the $r\phi$ -axis in the Krypton measurement was divided into 10 slices of ~ 11 cm length, to fit the resolution of the standard measurement, which is referenced as from database. The profile extracted from the Krypton measurement, appears to be slightly shifted to lower gain values, but the trend of the relative gain along the abscissa is similar for both measurements.

Even though this example shows very good agreement between the two measurements large deviations in the gain distribution between the measurement were observed as well, i.e. for chambers of type L2C1. As shown in table 7.5 these observations are highly dependent on the chamber type. In the fourth column of table 7.5 it is visible, that data on the gain uniformity measurement on 67 installed chambers is missing in the data base. The fraction of chambers with missing information depends on the chamber type, i.e. for chambers of type L0C1 the information on the gain uniformity measurement is missing for 31 chambers.

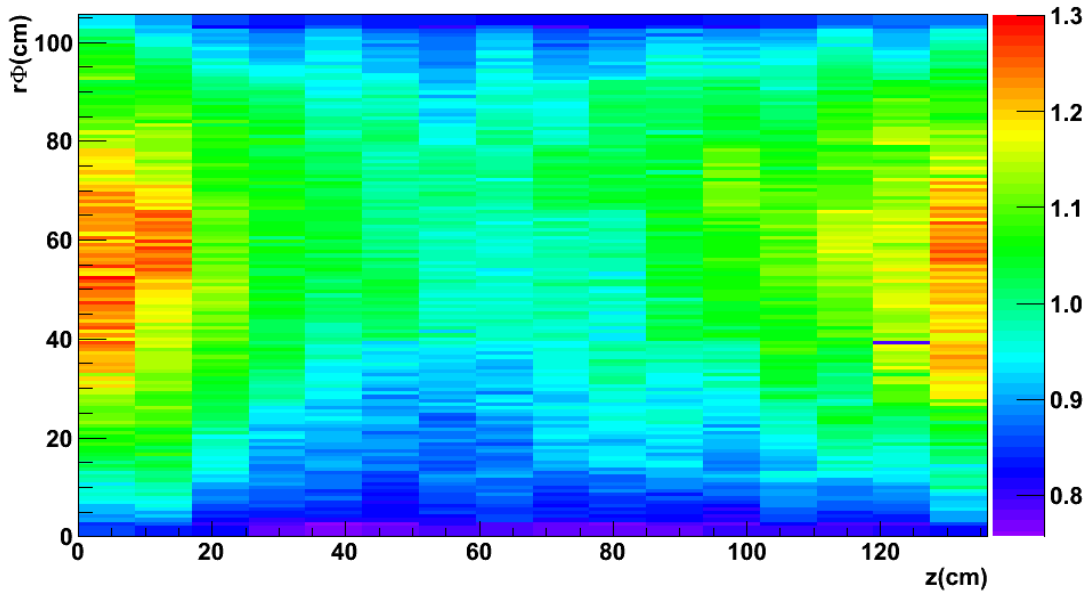


Figure 7.25.: Gain map of chamber (16-1-3) as extracted from the ^{83}Kr calibration. The topology it similar to the one shown in Fig. 7.24, showing a two-peak structure.

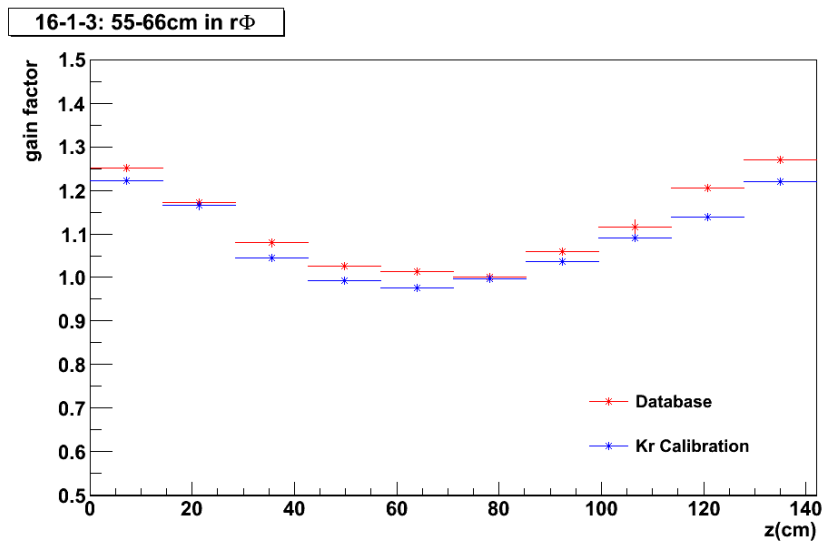


Figure 7.26.: Profile of the topologies acquired in the two measurements with $55 < r\phi < 66\text{cm}$. Data from the standard chamber testing is referred to as from database (red stars), data from the ^{83}Kr calibration is shown in blue. Despite small differences in the normalization the profile shows the same relative trend.

Given this large amount of missing data, only for 172 of all installed chambers moderate or good agreement was found between the two measurements. All gain maps were judged by eye. For 55 chambers, the relative gain distributions did not show similar trends. For chambers of the type L1C1, L3C0 and L3C1 excellent agreement was found. Especially L3 chambers showed a similar gain distribution in all chambers. Topologies for chambers of

type L2C1 could not be reproduced by the ^{83}Kr calibration.

The reasons for the remaining deviations are not yet fully understood. It is not related to the testing site, because good and bad agreement was found for chambers tested at single sites, i.e. L2C1 and L3C1, both tested at NIHAM. No connection to the used radioactive source was found either. A possible explanation for deviations could be the development of the testing procedure. For some chambers the gain uniformity appeared mirrored along the z - or the $r\phi$ -axis. This can be understood, considering that the ALICE coordinate system was introduced to the procedure three month after the testing was first documented and thus possible misunderstandings in the definition of the coordinate system are plausible. In addition, chambers were mounted vertically in the test stand, and not tested in a similar position as they have installed in the ALICE experiment.

7.9. Correlation between Gain and Anode Voltage

Studying the correlation between anode high voltage and gain allows the online adjustment of the high voltage such that gain variations due to changes in the atmospheric pressure are compensated. If the electric field is larger than the ionization threshold, the ionization cross-section increases with increasing electric field (described in chapter 2.3).

Thus, for the adjustments only the relative changes of the correlation are of major interest. Is the electric field in the vicinity of the wire large enough, the ionization cross-section increases with increasing electric field (described in chapter 2.3). Thus at the end of the 2011 Krypton calibration campaign, datasets with different high voltage settings (see table 6.3) were recorded to study the relationship between gain and anode high voltage. The analysis strategy and results will be explained in the following. Subsequently a comparison to previous studies is done.

7.9.1. Analysis Strategy and Results

In this analysis the dilation of the Krypton spectrum as a function of the anode high voltage setting will be examined. This study is carried out at the chamber basis, because the high voltage setting can only be adjusted for individual chambers. At the chamber basis, the Krypton decays of all pads in a chamber are considered, thus not many runs had to be recorded for these studies. Fig. 7.27 shows three reconstructed spectra for chamber (0-0-0), recorded with different anode high voltage settings. For comparison the maxima of the histograms were scaled to similar values. It is visible, that the spectra obtained for lowered anode voltage settings are dilated to lower ADC counts. However, as visible in Fig. 7.27, the energy resolution improves with lowered high voltage settings. For example, for the given chamber (0-0-0) the energy resolution measured at the main decay peak, improved from 10.4 % for the nominal high voltage setting (1530 V), to 7.2 % for the lowest high voltage setting (1450 V), which meets the design criteria of an energy resolution better than 10 %.

To quantify the dilation of the spectra, for each high voltage setting a Gaussian fit was performed to the decay peak at 41.6 keV and the position in ADC counts determined. This information was then further processed together with the exact high voltage setting of the chamber, which was read out from the offline condition database for the relevant runs. After all, three data points were obtained for each chamber.

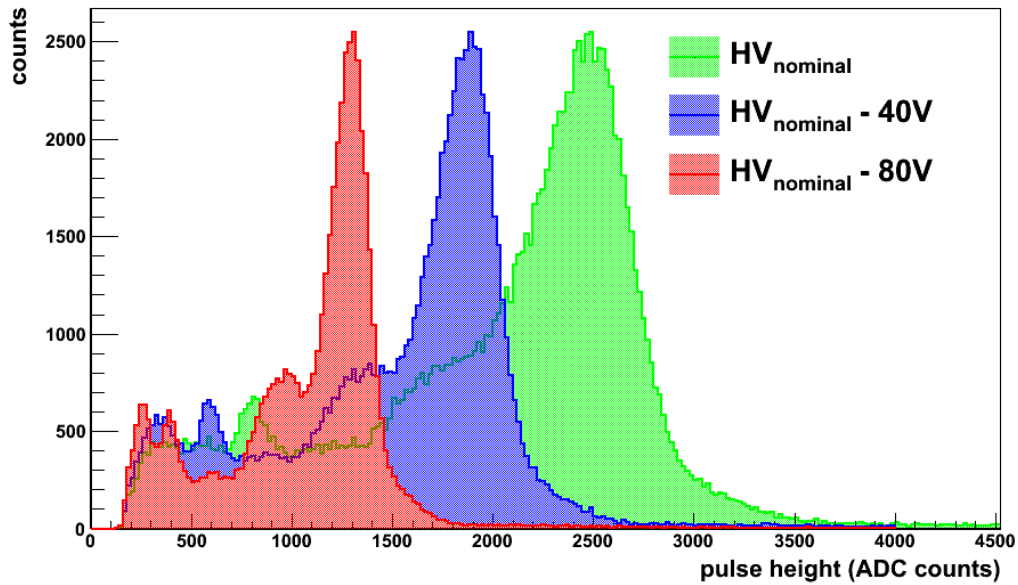


Figure 7.27.: Decay spectra of chamber (0-0-0) for different anode high voltage settings. The dilation to lower ADC counts for the reconstructed spectra at reduced high voltage settings is clearly visible.

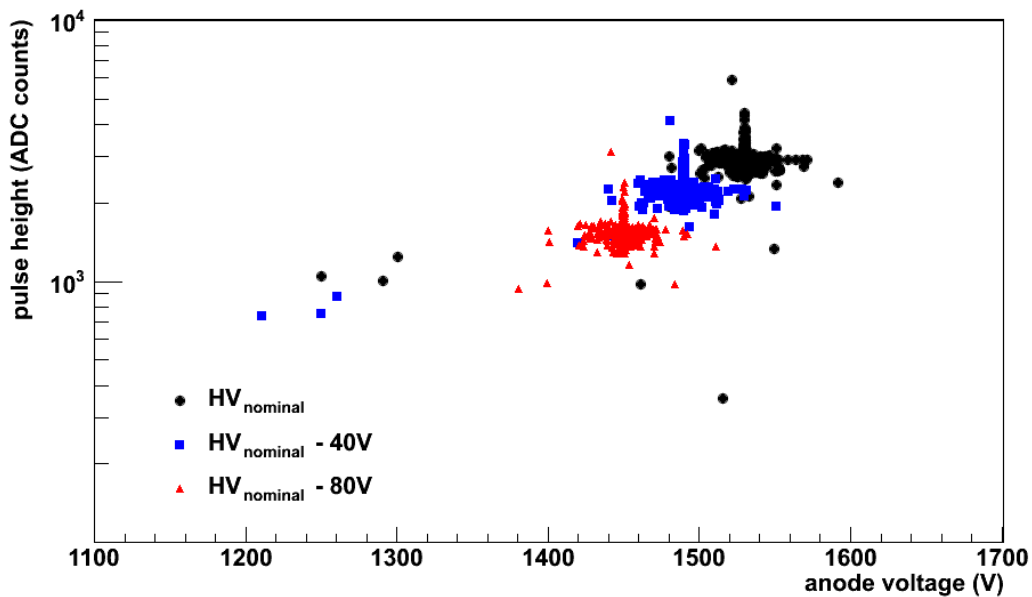


Figure 7.28.: Mean of the main decay peak plotted as a function of anode voltage for the three different settings. Chambers which were adjusted to uniform gain are scattered horizontally around the voltages at 1450 V, 1490 V and 1530 V whereas newly installed chambers have different gain at the same anode voltage setting and scatter vertically around the default voltages.

Fig. 7.28 shows the peak position versus the corresponding high voltage setting. For each chamber the pulse height of the reconstructed decay peak is presented as a function of the corresponding high voltage setting. Chambers, which were calibrated before, were adjusted to have uniform gain and thus their anode voltage setting was modified from the nominal values. Data points belonging to these chamber scatter horizontally around the three nominal anode voltage settings at 1530 V, 1490 V and 1450 V. The voltage settings of chambers, which were installed prior to the Krypton calibration campaign in the winter of 2011, were not modified. Thus the measured pulse height scatters vertically around the nominal high voltage settings.

From equation 2.10, an exponential relation between gain and anode voltage is expected. For this reason, an exponential function with two parameters, amplitude and slope, was fit to the three data points for each individual chamber. From the distribution of slope values from each chamber fit, shown in Fig. 7.29, an average slope of

$$S_{Kr} = 7.804 \pm 0.31 \times 10^{-3} \frac{1}{V} \quad (7.8)$$

was determined.

The amplitude

$$A_{Kr} = -3.959 \pm 0.037 \text{ ADC counts} \quad (7.9)$$

was determined in a similar way. However, actual value of interest is not the absolute but the relative change of gain in percent, α , when the anode voltage is changed by 1 V. Amplitudes will only be presented for completeness. From the slope, the percentage change of gain per 1 V change, α_{Kr} is calculated via

$$\frac{\Delta G}{G} \text{ per 1V} : \alpha = (e^s - 1) \times 100 \text{ [\%]} [51], \quad (7.10)$$

where s is the found slope. Thus

$$\alpha_{Kr} = 0.783 \pm 0.031 \text{ \%} \quad (7.11)$$

per 1 V change. The systematic uncertainty was propagated via Gaussian error propagation.

Comparison to previous Studies

Similar measurements were performed with small-sized prototype TRD chambers [7].

Fig. 7.30 displays the results from these measurements on the correlation between gain and anode high voltage. The exponential correlation, extracted with a fit, is currently used for adjusting the anode voltage of individual installed chambers in the ALICE experiment.

From the fit, an amplitude of

$$A_{Pr} = -5.828 \text{ ADC counts} \quad (7.12)$$

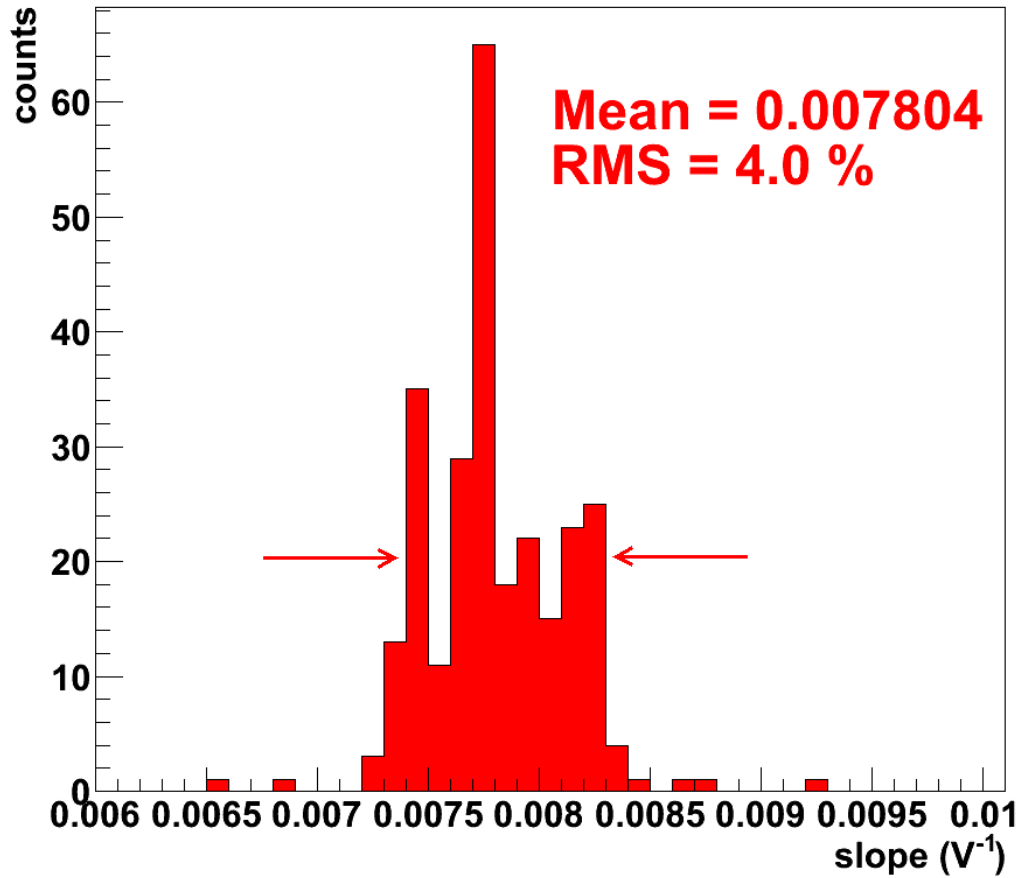


Figure 7.29.: Distribution of the slope parameters of all installed chambers.

and a slope

$$S_{Pr} = 9.095 \times 10^{-3} \frac{1}{V} \quad (7.13)$$

were determined. The slope corresponds to a percentage change of gain per 1 V of

$$\alpha_{Pr} = 0.914 \% \quad (7.14)$$

per 1 V change. Comparing to the mean slope of all chambers found in the Krypton calibration campaign, the two values do not agree. However, this is understood because the prototype chambers do not have the exact same geometry as the TRD readout chambers installed in the experiment. Thus, as explained in chapter 2.3.3, the gain properties of the devices are different. However, in the current experimental setup the high voltage is adjusted to pressure changes according to the data collected in the prototype measurement. This information has to be updated to the values obtained in the Krypton calibration, because they are more representative for the actual experimental setup, and will be available before the start of the next pp run in March 2012.

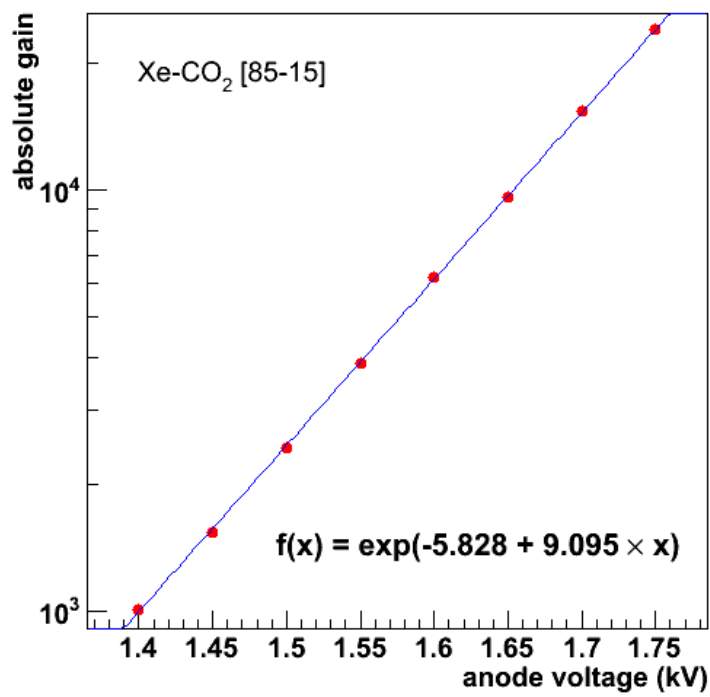


Figure 7.30.: Correlation between gain and anode high voltage for small-sized prototypes of the ALICE TRD readout chambers. The blue line represents the exponential relation fitted to the data points.

8. Alignment of the ALICE TRD

During the construction of the individual supermodules and chambers, strong mechanical constraints are imposed on the TRD design [7], to reduce deviations from the ideal position of the detector components. However, time driven deformation and mechanical tolerances during assembly lead to deviations for individual sectors and the detector elements have to be realigned. This alignment procedure strongly improves the spatial resolution and thus the track reconstruction [9] in the central barrel of the ALICE detector. It essentially improves the momentum resolution as well, because the transverse momentum of the charged particles produced in particle collisions is measured by the deflection of these particles in the magnetic field of the L3 magnet. An iterative analysis procedure is tuned to specifically correct the misalignment of the TRD supermodules, which is of the order of centimeters along the z-direction, and of the TRD readout chambers, which is of the order of millimeters.

In this chapter the basic concepts of alignment of the ALICE TRD will be briefly summarized. At first, a short motivation of the recent alignment is presented. In the following, the strategy and theory of the alignment procedure with comics tracks and particles from collisions is sketched, followed by an explanation of the possibilities for correcting the position of the misaligned objects. In the end the results of the recent alignment are presented.

8.1. Motivation

During data analysis in October 2011 it was realized that the individual sectors of the Transition Radiation Detector (TRD) showed an unexpectedly large mismatch in terms of position reconstruction of particle trajectories relative to the Time Projection Chamber (TPC). In the past these mismatches were explained by the installation of additional supermodules in different sectors, because the ALICE space frame, in which the TRD is mounted, was shifted by the additional weight in the order of centimeters. As alignment is an iterative procedure, these effects were corrected stepwise, with *manual alignment* [52] and an *offline alignment analysis* [53]. However, in this case no geometrical distortion was identified, but the reason was identified by an updated alignment of the TPC relative to the Inner Tracking System (ITS). As the TRD is aligned with respect to the TPC, new alignment between these detectors was necessary prior to the data taking of PbPb collisions in November 2011.

8.2. Analysis Strategy and Theory

To keep the deviation of the individual detector system from the ideal geometry as small as possible, the alignment procedure is divided into two steps. In the first step, the manual alignment, the chambers are mounted as precisely as possible into their assigned position

in a supermodule. For this purpose the supermodules have rods on the inside, with which the chambers are screwed together. High precision drilling of the screwing holes reduces the deviation from the ideal geometry to a few tenths of millimeters along the z -axis, and better than a millimeter in $r\phi$ -direction. In turn the supermodules are then accurately installed in the experiment, however deviations in the order of centimeters along the z -direction are caused by the insertion of the supermodules into the space frame. Readout pads in individual chamber are installed with a precision of better than $500\ \mu\text{m}$ [7] and are considered as ideally placed, because the alignment procedure is not as precise [53].

In the second step of the alignment procedure, the detector is aligned in an offline analysis with particle trajectories, either coming from cosmic or collision events (chapter 8.2.2). As a reference, the ideal geometry is saved in the offline condition data base.

In this thesis, the available analysis software was used to perform the second step and thus attention was given to the explanation of the alignment procedure with particle trajectories. Further details on the principles of the analysis can be found in [53].

8.2.1. Alignment Parameters

In correspondence to the ALICE coordinate system, a total of six parameters is used for alignment, shifts along the x -, y - and z -axes and tilts around these axes, parametrized with three Euler angles Ψ , Θ and Φ . The alignment of the TRD is performed in the local coordinate system (chapter 4.4), which transforms the global alignment parameters into shifts along the $r\phi$ -, z - and r -axes with the corresponding rotations. Fig. 8.3 shows a schematic drawing of the possible misalignment of an individual chamber from different perspectives.

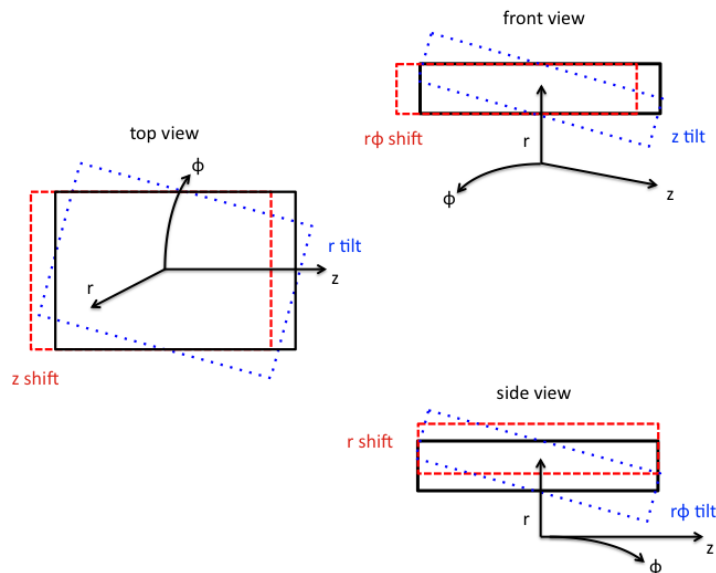


Figure 8.1.: Possible misalignment of a TRD readout chamber. Deviations from the ideal geometry (black, solid line) are expressed in shifts (red, dashed line) and tilts (blue, dotted line) along the axis. The figure was inspired by [53].

If the TRD is misaligned, the alignment procedure of the six parameters needs to follow

the TRD geometry hierarchy. On the highest level are the supermodules which have to be aligned relative to the TPC prior to other detector elements, because here the largest deviations of the order of centimeters from the ideal geometry are found. For the supermodule alignment, the arithmetic mean of the determined parameters of the two most central chambers in a module is taken to calculate the corresponding deviations for all chambers. In case of modules installed in sectors 13, 14 and 15, which do not have a central stack, the arithmetic mean of the parameters of the two most central chambers in stacks one and three respectively is taken. On the next level, individual stacks are aligned. In terms of alignment, the smallest volumes are the individual readout chambers.

8.2.2. Alignment with Particle Trajectories

In the following the working principle of reconstruction of particle trajectories in the central barrel of the ALICE detector is summarized in order to understand the alignment of the individual TRD volumes. The global tracking algorithm is based on a *Kalman-Filter Approach* [54], as shown in Fig. 8.2.

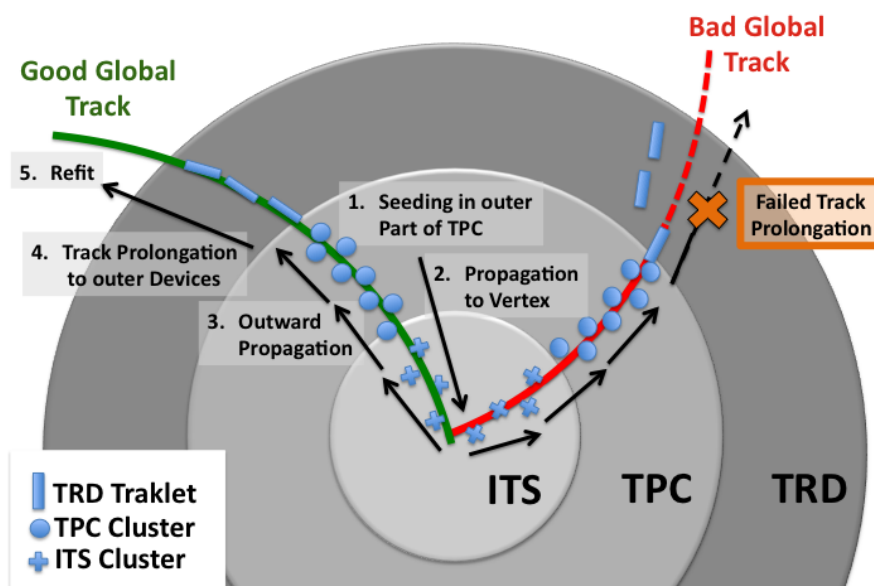


Figure 8.2.: Schematic view of the working principle of the global tracking algorithm for two tracks, one in an ideal geometry (left track) and one with strongly misaligned TRD chambers (right track). The figure was inspired by [9].

In the following, the working principle of the global tracking algorithm is outlined for an ideal geometry (left track in Fig. 8.2). Beginning at the outside surface of the TPC, the algorithm searches for clusters which are assumed to belong to the same track coming from the collision region (1). These clusters are combined to track segments, and the algorithm searches for more clusters in the inner part of the TPC. Clusters, which fit to the propagation of the track segment are added consecutively, until the track is prolonged

to the surface of the ITS. The same operation is carried out in parallel inside the ITS. After the track segments in the TPC and ITS are determined the algorithm tries to connect the two segments to a single complete track (2). In a second reconstruction step, the Kalman-Filter algorithm starts at the collision points and propagates the track outward to the outer wall of the TPC (3). Using the a prediction of the Kalman filter, an acceptance window for clusters in the TRD readout chamber located in the layer closest to the interaction region is opened. Clusters located in this acceptance window, the so called *road*, are assigned to this track. These clusters are called *associated clusters*. In turn, a *tracklet*, which is a linear approximation of the track on the TRD clusters, is constructed for the chamber and added to the track. Subsequently, the reconstruction continues with the next TRD layer. Essentially the global tracking algorithm searches for clusters in all central barrel detectors and aims to connect them into a corresponding global track (4). In the last step, a refit of the track is performed backwards (5), and all relevant information, such as the momentum, are stored. A more detailed explanation of the tracking reconstruction is found in [9].

In case TRD readout chambers show large misalignment with respect to the TPC, the tracking resolution declines or, in the worst case, the track is not prolonged to outer detectors of the central barrel. This scenario is shown for the right track in Fig. 8.2, where two tracklets reconstructed in the TRD are not associated to the global track.

The working principle of the alignment relative to the TPC is shown Fig. 8.3. For a uniform treatment in the alignment procedure, TPC clusters and TRD tracklets are referred to as *track points*.

In Fig. 8.3 the effect of a shifted readout chamber into negative y -direction is shown. If the global track algorithm assumes an ideal geometry, the track point is shifted by the same amount into negative y -direction as well. Connecting all equally-weighted track points to a single track, the complete track would be shifted and thus the position resolution reduced. In the worst case, the track point is not assigned at all to the track, and thus the track suddenly "ends". To correct the location of the mispositioned chamber, a track fit is performed on the reference track points, in this case recorded in the inner and outer readout chambers of the TPC. Here, three different fitting algorithms are available [55]: *FitLinear*, which is a linear approximation of straight trajectories, *FitRiemann*, which is based on Riemann circles and *FitKalman*, a simple version of the Kalman-Filter. The fitted track is then prolonged into the TRD and compared to the track points in each chamber. Their difference is the residual in that specific coordinate. The alignment procedure of the individual chambers is of statistical nature, thus the residuals are Gaussian distributed. A Gaussian function is fitted to the residuals of the six alignment parameter and the mean is identified as misalignment in that individual coordinate. The procedure is either using a *fast minimizer* or *linear minimizer*, which are based on a linear χ^2 minimization, or a χ^2 *minimizer*, based on χ^2 minimization [56]. For this analysis, the *FitRiemann* approximation together with the fast minimizer was used as it is the most sharp and fast combination. Further information is found in [53].

8.2.3. Alignment with Collisions from 2011

The final alignment of the TRD can be performed either with cosmic tracks or tracks coming from particle collisions. Ideally cosmic tracks momentum are used when the L3 magnet is turned off ($B = 0$ T). With this configuration the comic particles, which typically

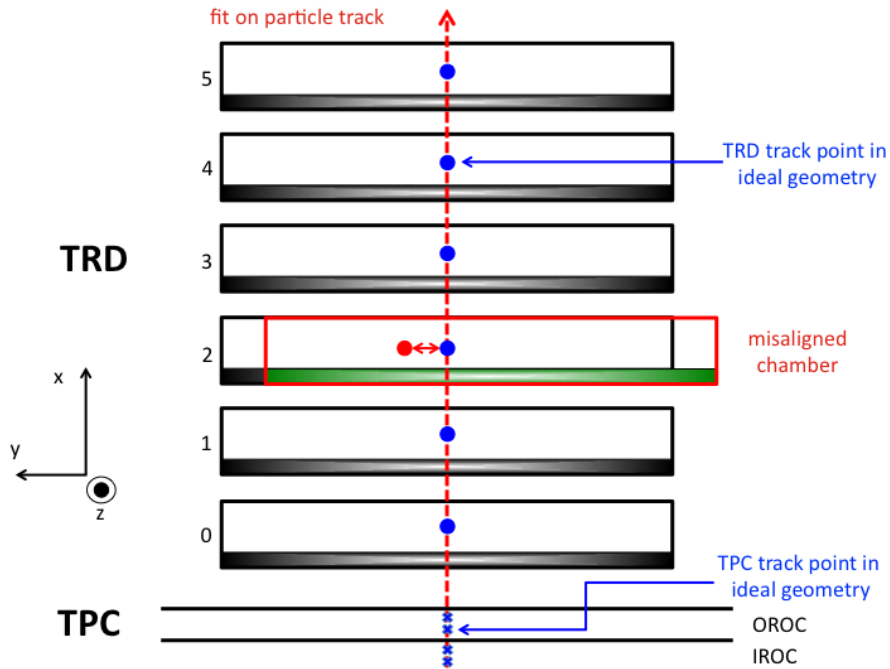


Figure 8.3.: Shown is a stack of six TRD readout chambers, with the third chamber shifted from the ideal geometry. The global tracking algorithm assumes all chambers ideally positioned, and thus the tracklet in chamber two is shifted by the same distance as the chamber. This misalignment is corrected after the comparison of the track point in the shifted chamber relative to a fitted track prolonged from the TPC reference track points in the *Inner Readout Chamber* (IROC) and in the *Outer Readout Chamber* (OROC). The figure was inspired by [53].

have a transverse momentum (p_t) between 1 and 10 GeV/c, fly straight through the detector and most precise results are achieved, because the muons only do little multiple scattering. However, because about 3000 track points per alignable volume are needed to rule out statistical effects on the analysis [53], and no high statistics data files were available with turned-off magnetic field, it was decided to use a set of 11 runs recorded during pp collisions at $\sqrt{s} = 7$ TeV in 2011. This set of runs was chosen because it included enough statistics and the TPC and TRD subsystems did not experience problems during the data taking. The magnetic field strength was $B = -0.5$ T. The p_t -range of these positive and negative charged particles extended up to 20 GeV/c, which corresponds to a maximal radius of curvature of ≈ 134 m. As shown in Fig. 8.4, through this approach sufficiently, large amount of track points, which passed the cuts presented in table 8.1, were recorded in the TRD readout chambers. Tracks with low p_t show the strongest curvature in the magnetic field and were considered to ensure good alignment for a wide p_t range.

However, a decrease of the number of track points with the radial position of the chamber is observed, i.e. for chamber number 0 to 5. This is a relict of the global tracking algorithm in the central barrel, searching for track points from the in- to the outside of the TRD. If the algorithm does not find a track point, or has low efficiency in finding them in an inner chamber, the track point finding efficiency in the following chamber is reduced, and so on. A projection in the xy-plane of the distribution of track points produced for the alignment of the TRD is shown in Fig. 8.5. From the inside to the outside the ITS, the IROC and

| Threshold Cut | | Amount of Data Kept | |
|------------------------------------|---------|---------------------|----------|
| Total amount of track points | - | 1.30×10^9 | 100.00 % |
| Minimum p_t | 0 GeV/c | 1.27×10^9 | 98.03 % |
| Minimum number of TPC track points | 100 | 3.26×10^7 | 2.51 % |
| Minimum number of TRD track points | 4 | 7.34×10^5 | 0.06 % |

Table 8.1.: Cuts imposed on the track points used for alignment. 0.06 % of the track points passed the cuts and were used for the alignment analysis.

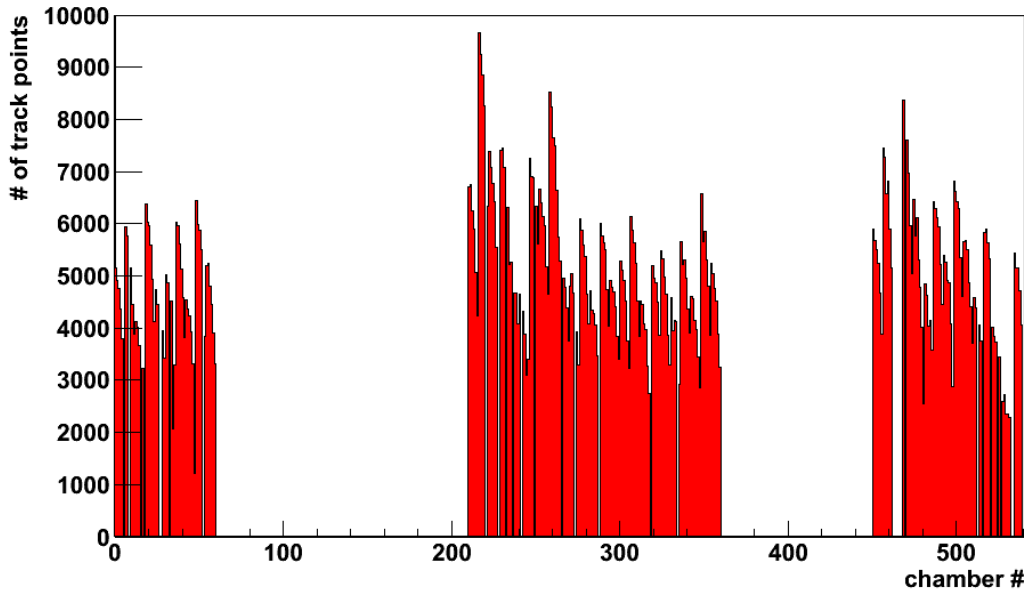


Figure 8.4.: Shown is the number of track points recorded in the individual TRD readout chambers and used for alignment.

OROC of the TPC, and finally the installed TRD readout chamber and some elements of the TOF subsystem of the ALICE experiment are visible through their population with track points. Here, only track points passing the criteria in table 8.1 are considered. Single TPC pads and TOF detectors located around $x = 0$ cm and $y = -400$ cm or $y = 400$ cm are not populated with track points because no valid tracks pass the installed TRD readout chambers and enter into this region.

8.3. Results

With the selected dataset, the misalignment of the TRD readout chambers relative to the TPC was significantly reduced. Fig. 8.6 through Fig. 8.8 display the previous and the updated alignment parameters for supermodules and chambers respectively. The green bars and black crosses represent the parameters for the supermodules and chambers taken from the offline condition data base, found in the previous alignment. The red bars and blue diamonds show the updated factors for the supermodules and chambers determined in the

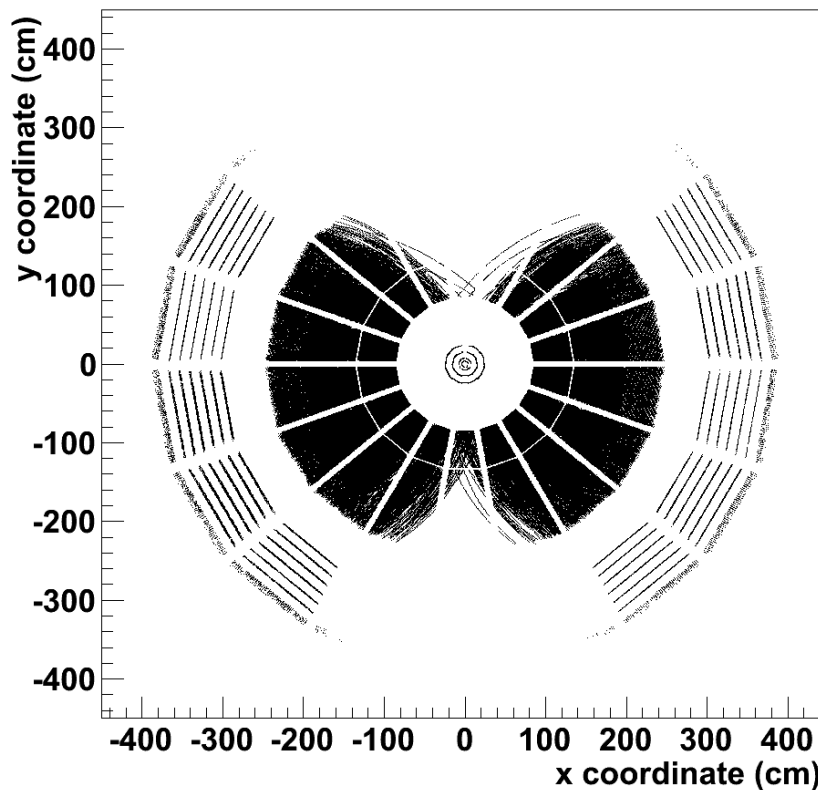


Figure 8.5.: 2-dimensional view of the track points used for the TRD alignment relative to the TPC. Going from the in- to the outside, the 6 layers of the ITS, the IROC and OROC of the TPC, the six layers of the installed TRD readout chambers and the some detectors of the TOF subsystem are visible through their population of track points.

current alignment analysis. All updated values shown here are relative to the parameters of the previous alignment in 2011. However, as the TPC was realigned relative to the ITS in the course of 2011, the TRD alignment parameters relative to the TPC had to be updated as well.

In Fig. 8.6 shifts and tilts around the $r\phi$ -coordinate are presented as a function of the chamber number in the upper and lower plot respectively. In the parameters from the previous alignment, large shifts in $r\phi$ of up to 1.7 cm are observed for all supermodules (green bars), i.e. supermodule 10 (corresponds to chamber numbers 300 to 329). It is visible, that supermodules 0 and 1 (corresponding to chamber numbers 0-59) and 15 to 17 (corresponding to chamber numbers 450-539) are all shifted to lower values of $r\phi$. The remaining supermodules, which are located on the other side of the space frame (left side of Fig. 8.5) are shifted to higher values of $r\phi$. The $r\phi$ -coordinate describes the local vertical axis for each sector, thus a downshift of the space frame caused by gravitation is observed. The updated $r\phi$ -parameters found in the alignment for the supermodules (red squares) are comparably small. $r\phi$ -shifts for individual chambers, which were extracted from the offline condition data base (black crosses) or found in the current alignment analysis (blue

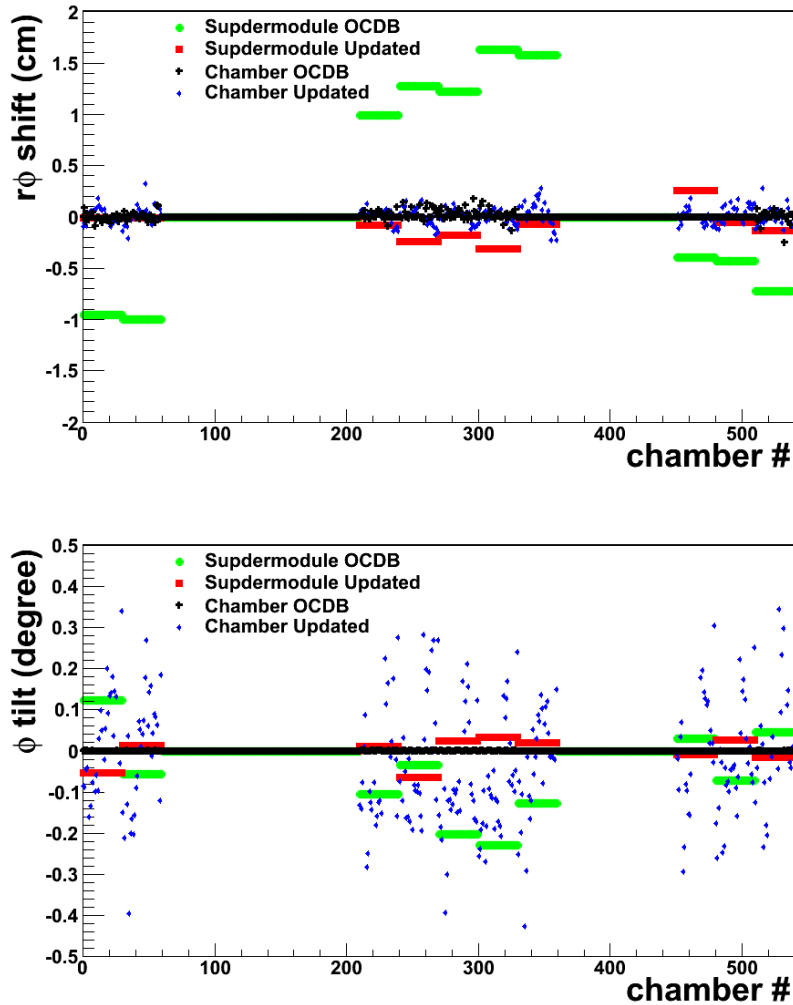


Figure 8.6.: Shown are the $r\phi$ -shifts and -tilts for the individual installed sectors and chambers. Previous alignment parameters are loaded from the offline condition data base and shown in green bars for the supermodules and black crosses for the chambers. The specific corrections found in the new alignment analysis relative to these values are represented by red squares (supermodules) and blue diamonds (chambers).

diamonds), are of the order of 0.2 cm and show no systematic effects. However, within all supermodules, i.e. for supermodule 15 (corresponding to chamber number 450 to 479), a systematic increase from around -0.3 to +0.3 degrees of the $r\phi$ -tilt parameter with increasing chamber number was found in the new alignment (blue diamonds). This indicates a tilt of the space frame of the same order.

Fig. 8.7 shows, that the preceding alignment parameters were corrected on the order of centimeters, even for individual chambers. In addition, decreasing values of the z-residuals are observed with increasing chamber number in all sectors. This is because the drift velocity calibration of the TPC was updated after the previous alignment. The resulting effect is explained in the following: The TPC calculates the z-position of a track through the drift time of the ionization electrons freed by a charged particle coming from collisions.

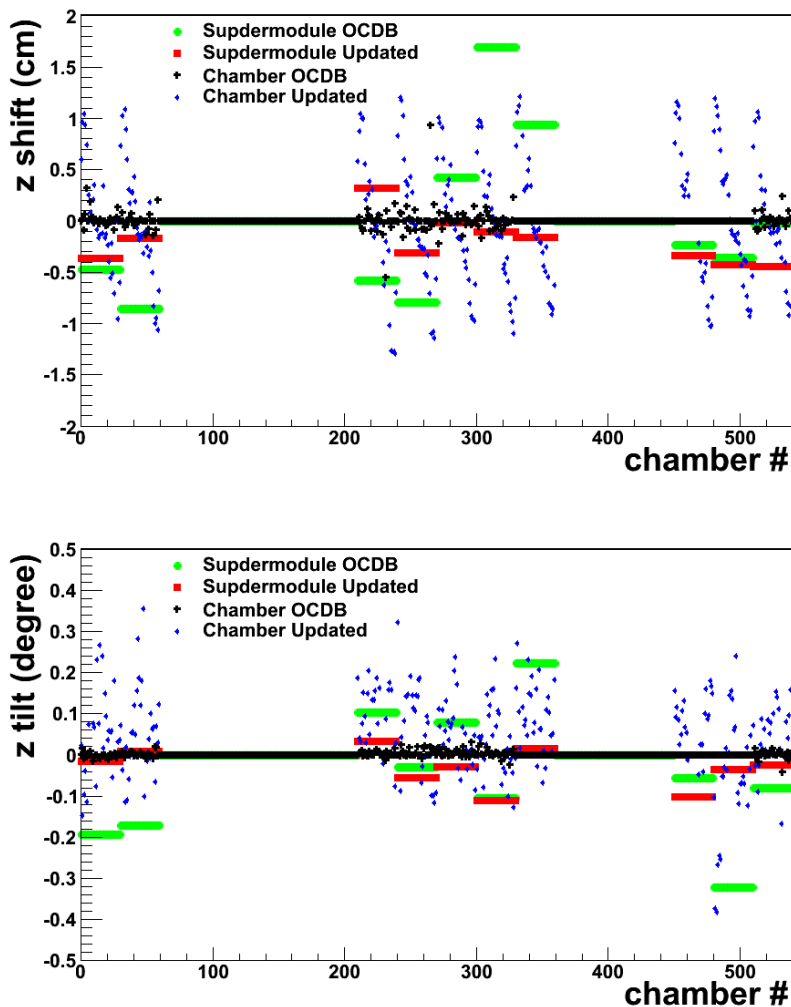


Figure 8.7.: Shown are the z -shifts and -tilts for the individual installed sectors and chambers. Previous alignment parameters are loaded from the offline condition data base and shown in green bars for the supermodules and black crosses for the chambers. The specific corrections found in the new alignment analysis relative to these values are represented by red squares (supermodules) and blue diamonds (chambers).

Thus an update of the drift velocity essentially leads to a shift of the z -position of the tracks. As a consequence, the track prolongation into the TRD is shifted and influences its alignment parameter. As visible in the lower plot of Fig. 8.7, most of the chambers were tilted by up to $+0.3$ degrees, as found in the new alignment analysis. Updated values of the z -tilt parameters of the individual supermodules relative to the previous alignment do not show systematic effects.

As seen for shifts along the z -axis, large systematic shifts along the r -axis were found for all chambers, shown in the upper plot of Fig. 8.8. Considering individual stacks of a supermodule, i.e. supermodule 7 (corresponding to chamber numbers 210-239), the first and last stack are shifted in the order of 0.4 cm into positive r -direction, whereas the shift increases for stacks located more centrally in the supermodule. The most central stack of

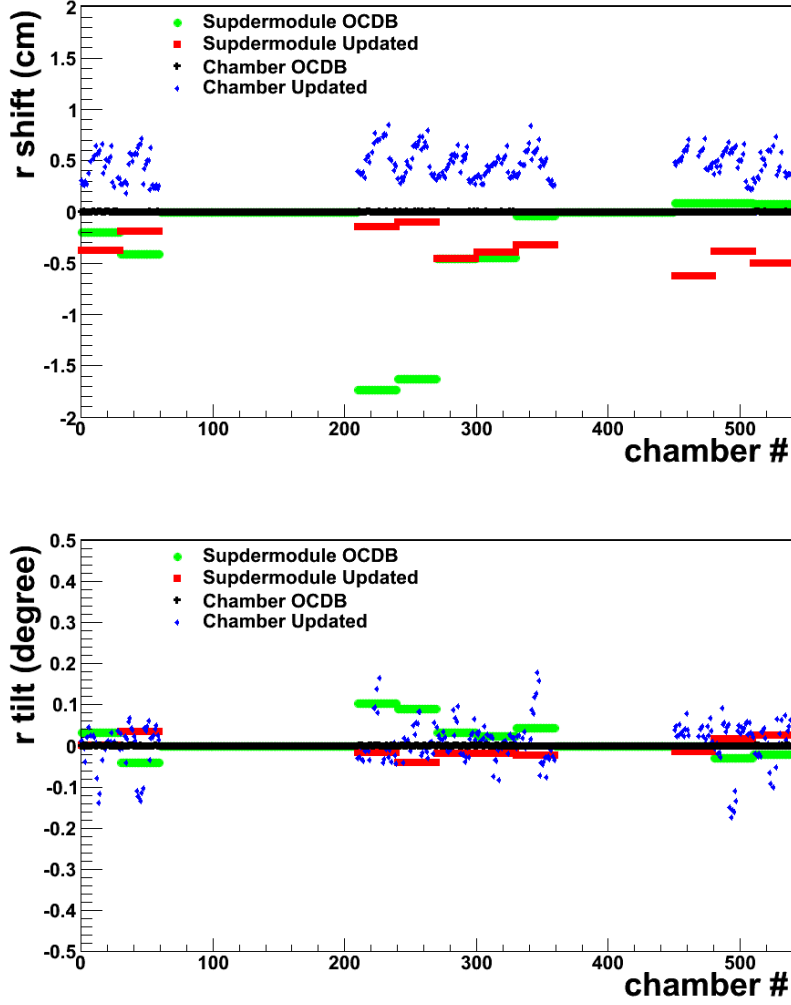


Figure 8.8.: Shown are the r -shifts and -tilts for the individual installed sectors and chambers. Previous alignment parameters are loaded from the offline condition data base and shown in green bars for the supermodules and black crosses for the chambers. The specific corrections found in the new alignment analysis relative to these values are represented by red squares (supermodules) and blue diamonds (chambers).

supermodule 7 (corresponding to chamber numbers 222 to 226) was misaligned by up to 0.8 cm. The alignment in the r -direction of the TRD is of significant importance, because it impacts the measurement of the transverse momentum (p_t) of the particles produced in collisions. Especially particles with low p_t and strong curvature in the magnetic field are affected. Tilts around the r -axis are of the order of 0.1 degrees.

After the alignment was performed, the determined corrections were added to the previous set of alignment parameters and the updated factors were made available in the offline condition data base.

9. Summary and Outlook

Summary

In this thesis the relative pad gain calibration of the ALICE TRD within the scope of the Krypton calibration campaign 2011 was performed. In February 2011, a radioactive Krypton source was installed at the bypass line of the ALICE TRD gas system, distributing the decays in all of the 10 installed sectors of the TRD. In the following 10 days, 153 runs were recorded, corresponding to 158.5 h of data taking and 2.67×10^9 Krypton decays.

In total, 2.3 billion Krypton decays were recorded allowing for the relative gain calibration of all 646,272 pads of the 294 installed TRD readout chambers. A new fitting algorithm was developed, which compares the measured pad spectra with a reference spectrum, and thus uses the complete information and statistics of the recorded Krypton decay spectra. Compared to the previously used method, agreement of better than 2 % is observed. Because the recorded data had to be split into two datasets, the analysis was performed iteratively, and the relative pad gain factors converged to a gain uniformity of better than 2 %. As a result, gain maps for all working chambers were produced and their structure was analyzed and compared to measurements performed during chamber construction. Good agreement between both measurements was found for 172 chambers out of 227. In addition, an energy resolution of 10 %, with a single standard deviation of 4.9 %, was determined for all installed chambers. A study on the chamber linearity of the measured signal compared to the deposited energy was performed, and the linear relation was confirmed better than 6 ‰.

At the end of the data taking period, the anode voltage settings of the installed TRD chambers were lowered stepwise by 40 V and 80 V. 386 million decays were recorded to study the relation between gain and anode high voltage. The gain as a function of voltage is described by an exponential function with a slope of $s_{Kr} = (7.861 \pm 0.025) \times 10^{-3} \frac{1}{V}$ and an amplitude of $A_{Kr} = -3.959 \pm 0.037$ ADC counts. These results were compared to measurements with smaller-sized prototype chambers. Differences of 14 % could be attributed to the slight differences in the geometry and gas mixtures in both measurements. However, both predict similar gains for the three considered high voltage settings at 1530 V, 1490 V and 1450 V. The work is still ongoing.

A smaller part of this thesis was an update of the alignment parameters of all installed supermodules with particles coming from pp collisions at a center-of-mass energy $\sqrt{s}=7$ TeV. Prior to the PbPb data taking in 2011, this update was necessary due to realignment of the ALICE TPC to the ALICE ITS, and therefore to ensure high performance of the ALICE detector. Especially large deviations were observed for the shifts and tilts around the z-axis. These were the result of miscalibration of the drift velocity in the TPC, which led to wrong positioning of the particle trajectories in the z-coordinate. As a consequence, tracks were not correctly prolonged to the TRD sectors. As the calibration of the TPC and TRD keep improving and are gradually updated, the work on the alignment of the

ALICE TRD is considered ongoing. Despite this ongoing work, the alignment of the TRD will be performed after the planned installation of three more sectors of the ALICE TRD in the winter shutdown 2011. Also the space frame might be further pushed down due to the increasing weight.

Outlook

The analysis of the data collected for the Krypton calibration turned out to be rather complex, because very large amounts of data had to be recorded to ensure that each pad in the installed chambers collects enough decays to be well calibrated. With the random trigger configuration, 1 to 2 Krypton decays were recorded per event, whereas most of the data was containing noise. In addition, at the end of 2012 the ALICE TRD is expected to be completely installed in the ALICE experiment, so the data taking period for the gain calibration will be much longer in order to collect enough statistics. There are several approaches to this challenge. On the experimental side, a freshly produced Krypton source with an higher activity than the one for the 2011 calibration campaign should be used, i.e. an activity of 3 MBq would already decrease the necessary amount of data by a factor of six, because then up to 6 Krypton decays per event are recorded. This directly reduces the necessary amount of data and thus the data size to be analyzed, as well as the data taking period. Another approach is to implement the Krypton cluster finder in the high level trigger of the TRD. In principle this could be implemented such, that the the output file with all histograms containing the decay spectra for the chambers and pads respectively, is directly produced online. This implementation at the high trigger level reduces the necessary analysis to the fitting stage and increases the data quality monitoring. In case this is not possible, for example because the trigger processing would be too slow, it is highly advisable to translate the current Krypton cluster finder into an *AliAnalysisTask*, which has a preferable format for analysis on the CERN GRID and would allow straight forward processing and merging of the data.

A possible improvement of the fitting algorithm would be the implementation of convolution of single spectra with the energy resolution of the individual readout pads as another free parameter.

In terms of data analysis, the correlation between gain and anode high voltage should be further studied. If more high-statistic data with the same gas admixture is collected, the actual differences between the Krypton and the prototype measurements could be further analyzed. If the actual differences in the slopes of the exponential functions prevail, the high voltage adjustment tables of the TRD for gain uniformity on chamber level would have to be updated.

Another proposal is to load the results of the gain uniformity measurement performed during chamber construction into the offline condition data base as a first estimate for relative pad gain corrections. For this, a further feasibility study on differences compared to the gain maps from the Krypton measurement would be necessary. It may also be useful to perform the Krypton calibration on single supermodules as a first test prior to their installation in the ALICE cavern, for example at the CERN testing site. Through this measurement individual broken pads and chambers could be classified as well.

A. Appendix

A.1. Acronyms and Technical Terms

| | |
|--------------|--|
| ADC | A nalog-to- D igital C onverter |
| ALICE | A L arge I on C ollider E xperiment |
| ATLAS | A T oroidal L H C A pparatus |
| CERN | C onseil E uropéen pour la R echerche N ucléaire |
| CMS | C ompact M uon S olenoid |
| DAQ | D ata A cquisition |
| DCS | D etector C ontrol S ystem |
| FEE | F ront- E nd E lectronics |
| FSM | F inite- S tate M achine |
| GTU | G lobal- T racking U nit |
| HLT | H igh- L evel T rigger |
| HMPID | H igh M omentum P article I Dentification D etector |
| IROC | I nnner R eadout C hamber |
| ITS | I nnner T racking S ystem |
| LEP | L arge E lectron P ositron C ollider |
| LHC | L arge H adron C ollider |
| LHCb | L arge H adron C ollider b eauty |
| MCM | M ulti C hip M odule |
| OCDB | O ffline C ondition D ata B ase |
| OROC | O uter R eadout C hamber |
| PHOS | P H O ton S pectrometer |
| QGP | Q uark- G luon P lasma |
| RAM | R andom- A ccess M emory |
| ROB | R ead O ut B oard |
| ROC | R ead O ut C hannel |
| SM | S uper M odule |
| TOF | T ime O f F light D etector |
| TPC | T ime P rojection C hamber |
| TRAP | T racklet P rocessor |
| TRD | T ransition R adiation D etector |
| TRG | T rigger S ystem |

A.2. Chambers used in the Analysis

| Chamber # | Type | $HV_{nominal}$ (V) | Mean(ADC counts) | Used in the Analysis |
|-----------|------|--------------------|------------------|----------------------|
| 000 | L0C1 | 1532.0 | 2511.03 +/- 0.85 | yes |
| 001 | L1C1 | 1533.4 | 2933.42 +/- 2.35 | yes |
| 002 | L2C1 | 1571.4 | 2932.39 +/- 1.10 | yes |
| 003 | L3C1 | 1525.7 | 2670.70 +/- 1.85 | yes |
| 004 | L4C1 | 1532.3 | 2607.96 +/- 0.66 | yes |
| 005 | L5C1 | 1550.7 | 2364.15 +/- 2.93 | yes (x) |
| 006 | L0C1 | 1544.2 | 2960.93 +/- 1.15 | yes |
| 007 | L1C1 | 1538.3 | 2983.32 +/- 1.93 | yes |
| 008 | L2C1 | 1512.5 | 2893.09 +/- 1.12 | yes (x) |
| 009 | L3C1 | 1517.3 | 3216.78 +/- 2.41 | yes |
| 010 | L4C1 | 1527.9 | 1787.45 +/- 0.04 | yes |
| 011 | L5C1 | 1502.5 | 2697.21 +/- 1.87 | yes |
| 012 | L0C0 | 1516.6 | 2960.70 +/- 1.18 | yes |
| 013 | L1C0 | 1545.5 | 2901.04 +/- 1.95 | yes |
| 014 | L2C0 | 1530.0 | 4490.38 +/- 4.14 | yes |
| 015 | L3C0 | - | - | no (x) |
| 016 | L4C0 | 1520.8 | 2962.25 +/- 1.34 | yes |
| 017 | L5C0 | 1542.2 | 2805.60 +/- 2.69 | yes |
| 018 | L0C1 | 1528.4 | 3079.12 +/- 1.38 | yes |
| 019 | L1C1 | 1543.9 | 2898.88 +/- 1.99 | yes |
| 020 | L2C1 | 1531.2 | 3023.26 +/- 1.54 | yes |
| 021 | L3C1 | 1550.9 | 3231.68 +/- 1.71 | yes |
| 022 | L4C1 | 1543.9 | 2966.29 +/- 1.37 | yes |
| 023 | L5C1 | 1530.4 | 3128.59 +/- 2.44 | yes |
| 024 | L0C1 | 1508.9 | 2823.54 +/- 1.34 | yes |
| 025 | L1C1 | 1541.2 | 2608.16 +/- 1.22 | yes |
| 026 | L2C1 | 1529.9 | 3020.63 +/- 1.77 | yes (x) |
| 027 | L3C1 | - | - | no (x) |
| 028 | L4C1 | 1553.1 | 2675.03 +/- 1.05 | yes |
| 029 | L5C1 | 1543.3 | 2988.65 +/- 1.67 | yes |

Table A.1.: Overview of the settings of the chambers in supermodule II installed in TRD sector 00. The mean describes the position in ADC counts found by fitting a Gaussian to the ^{83}Kr main decay peak. Chambers which were masked in the OCDB because of low gain or other reasons, are marked with an (x) in the 'Used in the Analysis' column. Details are discussed in Chapter 7.6.4.

| Chamber # | Type | $HV_{nominal}$ (V) | Mean(ADC counts) | Used in the Analysis |
|-----------|------|--------------------|------------------|----------------------|
| 030 | L0C1 | 1529.0 | 2781.38 +/- 1.93 | yes |
| 031 | L1C1 | 1536.8 | 2982.68 +/- 5.04 | yes |
| 032 | L2C1 | 1250.0 | 1051.89 +/- 0.11 | yes |
| 033 | L3C1 | 1553.0 | 2683.94 +/- 1.73 | yes |
| 034 | L4C1 | 1515.0 | 2863.14 +/- 0.93 | yes |
| 035 | L5C1 | 1540.1 | 3015.92 +/- 3.79 | yes |
| 036 | L0C1 | 1534.7 | 2931.92 +/- 1.38 | yes |
| 037 | L1C1 | 1534.4 | 2989.39 +/- 3.49 | yes |
| 038 | L2C1 | 1535.1 | 2960.82 +/- 1.30 | yes |
| 039 | L3C1 | 1534.9 | 3008.93 +/- 2.07 | yes |
| 040 | L4C1 | 1514.8 | 2965.42 +/- 1.11 | yes |
| 041 | L5C1 | 1519.6 | 2721.95 +/- 1.76 | yes |
| 042 | L0C0 | 1500.6 | 2629.24 +/- 0.96 | yes |
| 043 | L1C0 | 1519.4 | 3123.19 +/- 4.52 | yes |
| 044 | L2C0 | 1524.9 | 2924.60 +/- 1.33 | yes |
| 045 | L3C0 | 1529.1 | 3096.91 +/- 2.21 | yes |
| 046 | L4C0 | 1527.4 | 3089.91 +/- 1.51 | yes |
| 047 | L5C0 | 1516.7 | 3020.30 +/- 3.23 | yes |
| 048 | L0C1 | 1522.2 | 2873.59 +/- 1.53 | yes |
| 049 | L1C1 | 1530.7 | 2926.25 +/- 2.71 | yes |
| 050 | L2C1 | - | - | no - NOISE |
| 051 | L3C1 | - | - | no - GAIN TOO LOW |
| 052 | L4C1 | - | - | no - GAIN TOO LOW |
| 053 | L5C1 | 1503.3 | 2727.07 +/- 1.27 | yes |
| 054 | L0C1 | 1536.0 | 2839.93 +/- 1.99 | yes |
| 055 | L1C1 | 1517.9 | 2910.67 +/- 2.12 | yes |
| 056 | L2C1 | 1508.6 | 3030.66 +/- 1.37 | yes |
| 057 | L3C1 | 1513.7 | 2992.71 +/- 1.51 | yes |
| 058 | L4C1 | 1516.0 | 2953.60 +/- 1.39 | yes |
| 059 | L5C1 | 1481.6 | 2751.24 +/- 0.95 | yes |

Table A.2.: Overview of the settings of the chambers in supermodule VI installed in TRD sector 01. The mean describes the position in ADC counts found by fitting a Gaussian to the ^{83}Kr main decay peak. Details are discussed in Chapter 7.6.4.

| Chamber # | Type | $HV_{nominal}$ (V) | Mean(ADC counts) | Used in the Analysis |
|-----------|------|--------------------|------------------|----------------------|
| 210 | L0C1 | 1532.2 | 3050.11 +/- 1.29 | yes |
| 211 | L1C1 | 1512.4 | 2969.23 +/- 1.96 | yes |
| 212 | L2C1 | 1290.0 | 1014.08 +/- 0.10 | yes |
| 213 | L3C1 | 1553.7 | 2671.40 +/- 2.01 | yes |
| 214 | L4C1 | 1508.1 | 2870.98 +/- 0.78 | yes |
| 215 | L5C1 | 1525.9 | 2528.23 +/- 2.06 | yes |
| 216 | L0C1 | 1542.3 | 2890.19 +/- 1.32 | yes |
| 217 | L1C1 | 1524.0 | 2999.76 +/- 2.71 | yes |
| 218 | L2C1 | 1537.4 | 2806.10 +/- 1.14 | yes |
| 219 | L3C1 | 1551.7 | 2664.24 +/- 1.95 | yes |
| 220 | L4C1 | 1539.0 | 2884.61 +/- 1.11 | yes |
| 221 | L5C1 | 1524.8 | 2891.85 +/- 2.68 | yes |
| 222 | L0C0 | 1506.3 | 2975.12 +/- 1.28 | yes |
| 223 | L1C0 | 1514.7 | 3093.24 +/- 2.16 | yes |
| 224 | L2C0 | 1513.1 | 2871.68 +/- 1.39 | yes |
| 225 | L3C0 | 1527.2 | 2859.97 +/- 2.23 | yes |
| 226 | L4C0 | 1511.1 | 3153.04 +/- 1.38 | yes |
| 227 | L5C0 | 1533.7 | 2149.13 +/- 2.95 | yes |
| 228 | L0C1 | - | - | no (x) |
| 229 | L1C1 | 1535.0 | 2619.27 +/- 1.42 | yes |
| 230 | L2C1 | 1460.5 | 843.23 +/- 0.12 | yes |
| 231 | L3C1 | - | - | no |
| 232 | L4C1 | - | - | no (x) |
| 233 | L5C1 | 1515.7 | 3017.63 +/- 1.90 | yes |
| 234 | L0C1 | 1530.2 | 2942.53 +/- 1.70 | yes |
| 235 | L1C1 | 1545.4 | 2989.73 +/- 2.04 | yes |
| 236 | L2C1 | - | - | no (x) |
| 237 | L3C1 | 1568.1 | 2938.20 +/- 2.04 | yes |
| 238 | L4C1 | 1532.8 | 2916.50 +/- 1.49 | yes |
| 239 | L5C1 | 1526.7 | 2954.66 +/- 1.68 | yes |

Table A.3.: Overview of the settings of the chambers in supermodule III installed in TRD sector 07. The mean describes the position in ADC counts found by fitting a Gaussian to the ^{83}Kr main decay peak. Chambers which were masked in the OCDB because of low gain or other reasons, are marked with an (x) in the 'Used in the Analysis' column. Details are discussed in Chapter 7.6.4.

| Chamber # | Type | $HV_{nominal}$ (V) | Mean(ADC counts) | Used in the Analysis |
|-----------|------|--------------------|----------------------|----------------------|
| 240 | L0C1 | 1534.9 | 2700.01 +/- 0.968814 | yes |
| 241 | L1C1 | - | - | no (x) |
| 242 | L2C1 | 1530.2 | 2831.75 +/- 0.97 | yes |
| 243 | L3C1 | 1543.8 | 3017.26 +/- 4.26 | yes |
| 244 | L4C1 | 1525.7 | 2857.94 +/- 1.08 | yes |
| 245 | L5C1 | 1533.5 | 3033.95 +/- 4.31 | yes |
| 246 | L0C1 | 1543.0 | 2831.10 +/- 1.23 | yes |
| 247 | L1C1 | 1549.5 | 2935.90 +/- 2.14 | yes |
| 248 | L2C1 | 1544.8 | 3021.87 +/- 1.68 | yes |
| 249 | L3C1 | 1533.8 | 2917.50 +/- 3.28 | yes |
| 250 | L4C1 | 1523.2 | 2545.77 +/- 0.90 | yes |
| 251 | L5C1 | 1531.9 | 2644.74 +/- 2.10 | yes |
| 252 | L0C0 | 1528.9 | 2869.73 +/- 1.32 | yes |
| 253 | L1C0 | 1524.0 | 3115.93 +/- 2.56 | yes |
| 254 | L2C0 | 1527.5 | 2883.26 +/- 1.65 | yes |
| 255 | L3C0 | 1558.3 | 2936.48 +/- 4.66 | yes |
| 256 | L4C0 | 1530.4 | 2950.72 +/- 2.47 | yes |
| 257 | L5C0 | 1515.6 | 3151.25 +/- 3.41 | yes |
| 258 | L0C1 | 1545.7 | 2843.78 +/- 1.46 | yes |
| 259 | L1C1 | 1534.1 | 2822.04 +/- 1.67 | yes |
| 260 | L2C1 | 1539.0 | 2634.47 +/- 1.60 | yes |
| 261 | L3C1 | 1539.5 | 2919.05 +/- 3.11 | yes |
| 262 | L4C1 | 1534.8 | 2647.80 +/- 1.18 | yes |
| 263 | L5C1 | 1508.3 | 3099.49 +/- 1.74 | yes |
| 264 | L0C1 | 1536.2 | 2687.23 +/- 1.14 | yes |
| 265 | L1C1 | 1521.2 | 6054.96 +/- 13.71 | yes |
| 266 | L2C1 | 1536.5 | 2822.47 +/- 1.71 | yes |
| 267 | L3C1 | 1530.3 | 2944.18 +/- 1.80 | yes |
| 268 | L4C1 | 1550.1 | 2975.60 +/- 2.00 | yes |
| 269 | L5C1 | 1518.9 | 2853.46 +/- 1.29 | yes |

Table A.4.: Overview of the settings of the chambers in supermodule I installed in TRD sector 08. The mean describes the position in ADC counts found by fitting a Gaussian to the ^{83}Kr main decay peak. Chambers which were masked in the OCDB because of low gain or other reasons, are marked with an (x) in the 'Used in the Analysis' column. Details are discussed in Chapter 7.6.4.

| Chamber # | Type | $HV_{nominal}$ (V) | Mean(ADC counts) | Used in the Analysis |
|-----------|------|--------------------|------------------|----------------------|
| 270 | L0C1 | 1540.7 | 2795.72 +/- 1.98 | yes |
| 271 | L1C1 | 1552.7 | 2785.97 +/- 1.27 | yes |
| 272 | L2C1 | 1537.2 | 2727.04 +/- 2.16 | yes |
| 273 | L3C1 | 1300.0 | 1223.27 +/- 0.13 | yes |
| 274 | L4C1 | 1522.3 | 2560.37 +/- 1.76 | yes |
| 275 | L5C1 | 1569.2 | 2745.96 +/- 1.10 | yes |
| 276 | L0C1 | 1518.5 | 2892.93 +/- 3.11 | yes |
| 277 | L1C1 | 1525.5 | 2714.25 +/- 0.98 | yes |
| 278 | L2C1 | 1480.1 | 2962.35 +/- 3.23 | yes |
| 279 | L3C1 | 1548.9 | 2927.83 +/- 1.23 | yes |
| 280 | L4C1 | 1543.1 | 2930.92 +/- 2.79 | yes |
| 281 | L5C1 | 1526.0 | 3042.77 +/- 1.30 | yes |
| 282 | L0C0 | 1528.2 | 2976.66 +/- 1.95 | yes |
| 283 | L1C0 | 1523.6 | 3012.48 +/- 1.62 | yes |
| 284 | L2C0 | 1510.0 | 3137.02 +/- 2.18 | yes |
| 285 | L3C0 | 1552.9 | 2924.32 +/- 1.56 | yes |
| 286 | L4C0 | 1526.3 | 2993.93 +/- 2.68 | yes |
| 287 | L5C0 | 1515.0 | 352.785 +/- 0.66 | yes |
| 288 | L0C1 | 1550.8 | 2915.47 +/- 2.25 | yes |
| 289 | L1C1 | 1523.3 | 2561.40 +/- 1.39 | yes |
| 290 | L2C1 | 1550.0 | 2819.78 +/- 1.88 | yes |
| 291 | L3C1 | 1563.9 | 2930.27 +/- 1.58 | yes |
| 292 | L4C1 | 1523.3 | 3046.67 +/- 1.90 | yes |
| 293 | L5C1 | 1518.2 | 3008.84 +/- 1.35 | yes |
| 294 | L0C1 | 1527.4 | 2922.28 +/- 2.34 | yes |
| 295 | L1C1 | 1541.0 | 2896.17 +/- 1.42 | yes |
| 296 | L2C1 | 1537.0 | 2915.02 +/- 1.86 | yes |
| 297 | L3C1 | 1521.6 | 3189.07 +/- 2.06 | yes |
| 298 | L4C1 | 1546.6 | 3058.14 +/- 1.86 | yes |
| 299 | L5C1 | 1538.5 | 2940.24 +/- 2.45 | yes |

Table A.5.: Overview of the settings of the chambers in supermodule IV installed in TRD sector 09. The mean describes the position in ADC counts found by fitting a Gaussian to the ^{83}Kr main decay peak. Details are discussed in Chapter 7.6.4.

| Chamber # | Type | $HV_{nominal}$ (V) | Mean(ADC counts) | Used in the Analysis |
|-----------|------|--------------------|------------------|----------------------|
| 300 | L0C1 | 1535.5 | 2953.28 +/- 1.43 | yes |
| 301 | L1C1 | 1523.6 | 3003.27 +/- 2.87 | yes |
| 302 | L2C1 | 1533.3 | 2821.59 +/- 0.96 | yes |
| 303 | L3C1 | 1536.0 | 2917.39 +/- 2.22 | yes |
| 304 | L4C1 | 1524.2 | 2816.53 +/- 1.16 | yes |
| 305 | L5C1 | 1512.7 | 2527.81 +/- 1.55 | yes |
| 306 | L0C1 | 1531.7 | 2852.82 +/- 1.18 | yes |
| 307 | L1C1 | 1524.2 | 3093.30 +/- 3.11 | yes |
| 308 | L2C1 | 1499.3 | 3217.18 +/- 1.23 | yes |
| 309 | L3C1 | 1531.4 | 3166.17 +/- 2.59 | yes |
| 310 | L4C1 | 1520.0 | 3033.66 +/- 1.07 | yes |
| 311 | L5C1 | 1537.3 | 2975.32 +/- 3.14 | yes |
| 312 | L0C0 | 1516.5 | 2925.49 +/- 1.47 | yes |
| 313 | L1C0 | 1540.6 | 2656.38 +/- 1.90 | yes |
| 314 | L2C0 | 1526.5 | 2936.61 +/- 1.71 | yes |
| 315 | L3C0 | 1528.6 | 3179.62 +/- 2.51 | yes |
| 316 | L4C0 | 1534.2 | 3041.60 +/- 1.52 | yes |
| 317 | L5C0 | 1541.6 | 3017.44 +/- 2.54 | yes |
| 318 | L0C1 | - | - | no (x) |
| 319 | L1C1 | 1504.4 | 3117.87 +/- 2.04 | yes |
| 320 | L2C1 | 1520.2 | 3016.88 +/- 1.36 | yes |
| 321 | L3C1 | 1519.8 | 2641.36 +/- 1.18 | yes |
| 322 | L4C1 | 1532.8 | 2680.11 +/- 1.04 | yes |
| 323 | L5C1 | 1520.4 | 2973.75 +/- 1.72 | yes |
| 324 | L0C1 | 1514.5 | 3062.18 +/- 1.62 | yes |
| 325 | L1C1 | 1480.0 | 1966.97 +/- 0.58 | yes |
| 326 | L2C1 | 1515.7 | 2937.53 +/- 1.30 | yes |
| 327 | L3C1 | 1537.3 | 2644.59 +/- 1.21 | yes |
| 328 | L4C1 | 1535.0 | 2940.28 +/- 1.40 | yes |
| 329 | L5C1 | 1546.6 | 2936.60 +/- 1.60 | yes |

Table A.6.: Overview of the settings of the chambers in supermodule VII installed in TRD sector 10. The mean describes the position in ADC counts found by fitting a Gaussian to the ^{83}Kr main decay peak. Chambers which were masked in the OCDB because of low gain or other reasons, are marked with an (x) in the 'Used in the Analysis' column. Details are discussed in Chapter 7.6.4.

| Chamber # | Type | $HV_{nominal}$ (V) | Mean(ADC counts) | Used in the Analysis |
|-----------|------|--------------------|-------------------|----------------------|
| 330 | L0C1 | 1530.0 | 2895.88 +/- 1.66 | yes |
| 331 | L1C1 | 1530.0 | 3177.78 +/- 6.70 | yes |
| 332 | L2C1 | 1530.0 | 2849.34 +/- 1.81 | yes |
| 333 | L3C1 | 1530.0 | 2866.75 +/- 6.19 | yes |
| 334 | L4C1 | 1530.0 | 2936.07 +/- 1.57 | yes |
| 335 | L5C1 | 1530.0 | 2681.30 +/- 4.05 | yes |
| 336 | L0C1 | 1530.0 | 2961.77 +/- 1.75 | yes |
| 337 | L1C1 | 1530.0 | 3457.07 +/- 22.42 | yes |
| 338 | L2C1 | 1530.0 | 2711.03 +/- 2.26 | yes |
| 339 | L3C1 | 1530.0 | 3376.85 +/- 26.71 | yes |
| 340 | L4C1 | 1530.0 | 3260.14 +/- 10.20 | yes |
| 341 | L5C1 | 1530.0 | 3486.48 +/- 11.10 | yes |
| 342 | L0C0 | 1530.0 | 2740.57 +/- 1.50 | yes |
| 343 | L1C0 | 1530.0 | 3119.08 +/- 3.22 | yes |
| 344 | L2C0 | 1530.0 | 3326.74 +/- 3.93 | yes |
| 345 | L3C0 | 1530.0 | 2860.30 +/- 4.54 | yes |
| 346 | L4C0 | 1530.0 | 2977.97 +/- 1.89 | yes |
| 347 | L5C0 | 1530.0 | 4283.14 +/- 27.96 | yes |
| 348 | L0C1 | 1530.0 | 3145.03 +/- 3.51 | yes |
| 349 | L1C1 | 1530.0 | 2861.59 +/- 3.86 | yes |
| 350 | L2C1 | 1530.0 | 3014.16 +/- 4.60 | yes |
| 351 | L3C1 | 1530.0 | 2840.78 +/- 2.24 | yes |
| 352 | L4C1 | 1530.0 | 2795.08 +/- 3.51 | yes |
| 353 | L5C1 | 1530.0 | 3034.46 +/- 3.69 | yes |
| 354 | L0C1 | 1530.0 | 2660.59 +/- 1.88 | yes |
| 355 | L1C1 | 1530.0 | 2642.12 +/- 1.76 | yes |
| 356 | L2C1 | 1530.0 | 2956.12 +/- 3.30 | yes |
| 357 | L3C1 | - | - | no - NOISE |
| 358 | L4C1 | 1530.0 | 2927.59 +/- 1.58 | yes |
| 359 | L5C1 | 1530.0 | 3076.51 +/- 2.89 | yes |

Table A.7.: Overview of the settings of the chambers in supermodule IX installed in TRD sector 11. The mean describes the position in ADC counts found by fitting a Gaussian to the ^{83}Kr main decay peak. Details are discussed in Chapter 7.6.4.

| Chamber # | Type | $HV_{nominal}$ (V) | Mean(ADC counts) | Used in the Analysis |
|-----------|------|--------------------|-------------------|----------------------|
| 450 | L0C1 | 1530.0 | 2724.68 +/- 1.97 | yes |
| 451 | L1C1 | 1530.0 | 3030.86 +/- 3.58 | yes |
| 452 | L2C1 | 1530.0 | 2959.51 +/- 5.27 | yes |
| 453 | L3C1 | 1530.0 | 3008.90 +/- 3.28 | yes |
| 454 | L4C1 | 1530.0 | 2924.68 +/- 7.00 | yes |
| 455 | L5C1 | 1530.0 | 3744.99 +/- 12.43 | yes |
| 456 | L0C1 | 1530.0 | 2725.26 +/- 3.69 | yes |
| 457 | L1C1 | 1530.0 | 3041.87 +/- 3.35 | yes |
| 458 | L2C1 | - | - | (xx) |
| 459 | L3C1 | 1530.0 | 2978.33 +/- 2.81 | yes |
| 460 | L4C1 | 1530.0 | 2976.34 +/- 4.62 | yes |
| 461 | L5C1 | 1530.0 | 3657.45 +/- 15.50 | yes |
| 462 | L0C0 | - | - | not installed (x) |
| 463 | L1C0 | - | - | not installed (x) |
| 464 | L2C0 | - | - | not installed (x) |
| 465 | L3C0 | - | - | not installed (x) |
| 466 | L4C0 | - | - | not installed (x) |
| 467 | L5C0 | - | - | not installed (x) |
| 468 | L0C1 | 1530.0 | 2555.46 +/- 1.38 | yes |
| 469 | L1C1 | - | - | no (x) |
| 470 | L2C1 | 1530.0 | 2710.38 +/- 1.93 | yes |
| 471 | L3C1 | 1530.0 | 3386.86 +/- 5.61 | yes |
| 472 | L4C1 | 1530.0 | 3191.52 +/- 8.95 | yes |
| 473 | L5C1 | 1530.0 | 3633.78 +/- 13.91 | yes |
| 474 | L0C1 | - | - | no - NOISE |
| 475 | L1C1 | 1530.0 | 3236.23 +/- 3.54 | yes |
| 476 | L2C1 | 1530.0 | 2770.02 +/- 2.01 | yes |
| 477 | L3C1 | 1530.0 | 3224.80 +/- 5.99 | yes |
| 478 | L4C1 | 1530.0 | 3234.66 +/- 6.01 | yes |
| 479 | L5C1 | 1530.0 | 2507.36 +/- 2.56 | yes |

Table A.8.: Overview of the settings of the chambers in supermodule XI installed in TRD sector 15. The mean describes the position in ADC counts found by fitting a Gaussian to the ^{83}Kr main decay peak. Chambers which were masked in the OCDB because of low gain or other reasons, are marked with an (x) in the 'Used in the Analysis' column. Chamber 458 is marked with (xx), because no valid chamber spectrum is available due to a three broken pads, however the chamber was included in the analysis. Details are discussed in Chapter 7.6.4.

| Chamber # | Type | $HV_{nominal}$ (V) | Mean(ADC counts) | Used in the Analysis |
|-----------|------|--------------------|-------------------|----------------------|
| 480 | L0C1 | 1530.0 | 2637.96 +/- 2.19 | yes |
| 481 | L1C1 | 1530.0 | 3187.44 +/- 5.91 | yes |
| 482 | L2C1 | 1530.0 | 3289.97 +/- 5.36 | yes |
| 483 | L3C1 | 1530.0 | 3124.15 +/- 6.41 | yes |
| 484 | L4C1 | 1530.0 | 3118.10 +/- 4.14 | yes |
| 485 | L5C1 | 1530.0 | 3154.81 +/- 3.59 | yes |
| 486 | L0C1 | - | - | no -NOISE |
| 487 | L1C1 | 1530.0 | 3055.30 +/- 6.92 | yes |
| 488 | L2C1 | 1530.0 | 3220.03 +/- 8.51 | yes |
| 489 | L3C1 | 1530.0 | 3157.41 +/- 6.93 | yes |
| 490 | L4C1 | 1530.0 | 3265.94 +/- 3.52 | yes |
| 491 | L5C1 | 1530.0 | 3283.75 +/- 22.44 | yes |
| 492 | L0C0 | 1530.0 | 3035.16 +/- 2.40 | yes |
| 493 | L1C0 | 1530.0 | 3717.86 +/- 60.58 | yes |
| 494 | L2C0 | 1530.0 | 3141.60 +/- 5.44 | yes |
| 495 | L3C0 | 1530.0 | 3111.32 +/- 7.11 | yes |
| 496 | L4C0 | 1530.0 | 3229.23 +/- 6.11 | yes |
| 497 | L5C0 | 1530.0 | 3241.12 +/- 5.24 | yes |
| 498 | L0C1 | 1530.0 | 2817.32 +/- 3.07 | yes |
| 499 | L1C1 | 1530.0 | 3101.16 +/- 10.40 | yes |
| 500 | L2C1 | 1530.0 | 3328.73 +/- 6.48 | yes |
| 501 | L3C1 | 1530.0 | 3352.70 +/- 4.08 | yes |
| 502 | L4C1 | 1530.0 | 3459.71 +/- 13.28 | yes |
| 503 | L5C1 | 1530.0 | 3511.74 +/- 18.80 | yes |
| 504 | L0C1 | 1530.0 | 2844.20 +/- 2.91 | yes |
| 505 | L1C1 | 1530.0 | 3067.93 +/- 3.10 | yes |
| 506 | L2C1 | 1530.0 | 3262.41 +/- 28.60 | yes |
| 507 | L3C1 | 1530.0 | 3293.28 +/- 10.30 | yes |
| 508 | L4C1 | 1530.0 | 2499.96 +/- 1.37 | yes |
| 509 | L5C1 | 1530.0 | 3027.73 +/- 2.59 | yes |

Table A.9.: Overview of the settings of the chambers in sector VIII installed in TRD sector 16. The mean describes the position in ADC counts found by fitting a Gaussian to the ^{83}Kr main decay peak.

| Chamber # | Type | $HV_{nominal}$ (V) | Mean(ADC counts) | Used in the Analysis |
|-----------|------|--------------------|------------------|----------------------|
| 510 | L0C1 | 1525.4 | 2530.35 +/- 0.80 | yes |
| 511 | L1C1 | 1518.7 | 2951.74 +/- 2.07 | yes |
| 512 | L2C1 | 1503.6 | 2544.93 +/- 2.41 | yes (x) |
| 513 | L3C1 | 1536.1 | 3106.03 +/- 1.06 | yes |
| 514 | L4C1 | 1539.1 | 2881.46 +/- 3.33 | yes |
| 515 | L5C1 | 1533.6 | 2922.33 +/- 0.82 | yes |
| 516 | L0C1 | 1532.0 | 2936.98 +/- 1.24 | yes |
| 517 | L1C1 | 1550.6 | 2945.28 +/- 2.33 | yes |
| 518 | L2C1 | 1527.5 | 3055.48 +/- 2.32 | yes |
| 519 | L3C1 | 1550.7 | 2640.76 +/- 0.89 | yes |
| 520 | L4C1 | - | - | no (x) |
| 521 | L5C1 | 1504.2 | 3003.82 +/- 1.07 | yes |
| 522 | L0C0 | 1532.3 | 3048.53 +/- 1.55 | yes |
| 523 | L1C0 | 1506.1 | 2844.15 +/- 1.76 | yes |
| 524 | L2C0 | 1544.0 | 2765.46 +/- 3.70 | yes (x) |
| 525 | L3C0 | 1528.5 | 2615.94 +/- 0.99 | yes |
| 526 | L4C0 | - | - | no (x) |
| 527 | L5C0 | 1500.9 | 3252.21 +/- 1.89 | yes |
| 528 | L0C1 | 1549.8 | 2922.31 +/- 1.37 | yes |
| 529 | L1C1 | 1540.9 | 2643.88 +/- 1.31 | yes |
| 530 | L2C1 | 1518.6 | 3056.87 +/- 1.74 | yes |
| 531 | L3C1 | 1523.7 | 2725.83 +/- 1.09 | yes |
| 532 | L4C1 | - | - | no (x) |
| 533 | L5C1 | - | - | no (x) |
| 534 | L0C1 | 1508.7 | 2946.37 +/- 1.43 | yes |
| 535 | L1C1 | 1530.1 | 2639.03 +/- 1.29 | yes |
| 536 | L2C1 | 1524.6 | 3038.26 +/- 1.73 | yes |
| 537 | L3C1 | 1537.3 | 2853.82 +/- 1.58 | yes |
| 538 | L4C1 | 1591.6 | 2353.01 +/- 4.20 | yes |
| 539 | L5C1 | - | - | no (x) |

Table A.10.: Overview of the settings of the chambers in supermodule V installed in TRD sector 17. The mean describes the position in ADC counts found by fitting a Gaussian to the ^{83}Kr main decay peak. Chambers which were masked in the OCDB because of low gain or other reasons, are marked with an (x) in the 'Used in the Analysis' column. Details are discussed in Chapter 7.6.4.

Bibliography

- [1] G. Lemaître, "Un univers homogène de masse constante et de rayon croissant rendant compte de la vitesse radiale des nébuleuses extragalactiques", *Annales de la Societe Scientifique de Bruxelles*, A47, p. 49-59, (1927).
- [2] E. Hubble, "A relation between distance and radial velocity among extra-galactic nebulae", *Proc. Natl. Acad. Sci. USA* **15**, 168-173, (1929).
- [3] A.A Penzias; R. W. Wilson, "A Measurement Of Excess Antenna Temperature At 4080 Mc/s". *Astrophysical Journal Letters* **142**: 419-421 (1965).
- [4] M.D. Gladders *et al.*, "Cosmological Constraints from the Red-Sequence Cluster Survey", *The Astrophysical Journal* **665** (1): 128-132, (2007).
- [5] The ALICE Collaboration, F. Carminati *et al.*, "ALICE: Physics Performance Report, Volume I", *J. Phys. G: Nucl. Part. Phys.* **30**, 1517 (2004).
- [6] K. Yagi *et al.*: "Quark-Gluon Plasma", Cambridge University Press, (2005).
- [7] The ALICE Collaboration, "ALICE: Technical Design Report of the Transition Radiation Detector", ALICE TDR 009, CERN-LHCC-2001-021 (2001).
- [8] B. Hess, Diploma Thesis, "Online Electron Identification for Triggering with the ALICE Transition Radiation Detector", Ruprecht-Karls Universität Heidelberg, (2011).
- [9] D. Lohner, Diploma Thesis, "Tracking Resolution of the ALICE Transition Radiation Detector", Ruprecht-Karls Universität Heidelberg, (2010).
- [10] F. Abe *et al.* (CDF Collaboration), "Observation of Top Quark Production in pp Collisions with the Collider Detector at Fermilab". *Physical Review Letters* **74** (14) (1995).
- [11] S. Abachi *et al.* (DØ Collaboration), "Search for High Mass Top Quark Production in pp Collisions at $\sqrt{s} = 1.8$ TeV". *Physical Review Letters* **74** (13) (1995).
- [12] B. Povh; K. Rith; C. Scholz; F. Zetsche: "Teilchen und Kerne", 7. Auflage Heidelberg: Springer (2006).
- [13] F. Englert; R. Brout, "Broken Symmetry and the Mass of Gauge Vector Mesons". *Physical Review Letters* **13** (9) (1964).
- [14] P. Higgs, "Broken Symmetries and the Masses of Gauge Bosons", *Physical Review Letters* **13** (16) (1964).

-
- [15] QR Ahmad *et al.*, "Measurement of the Rate of $\nu_e + d \rightarrow p + p + e^-$ Interactions Produced by 8B Solar Neutrinos at the Sudbury Neutrino Observatory". *Physical Review Letters* **87** (7) (2001).
- [16] The ALPHA Collaboration, "Confinement of antihydrogen for 1000 seconds". arXiv:1104.4982, (2011).
- [17] Planck Science Team (.PDF). Planck: The Scientific Programme (Blue Book). ESA-SCI (2005)-1. Version 2. European Space Agency. Retrieved 2009-03-06, (2005).
- [18] N. Cabibbo, "Exponential hadronic spectrum and quark liberation", *Physics Letters* **59**, 67-69, (1975).
- [19] P. Braun-Munzinger; K. Redlich; J. Stachel: "Particle Production in Heavy Ion Collisions". nucl-th, 0304013, (2003).
- [20] M. McGuigan *et al.*, "Simulation of a relativistic collision between two gold nuclei", Time, 2000.
- [21] K. Nakamura *et al.* (*Particle Data Group*), *J. Phys. G* **37**, 075021 (2010) and 2011 partial update for the 2012 edition.
- [22] C. Grupen and B. A. Shwartz: "Particle Detectors", 2nd ed. Cambridge: Cambridge University Press (2008).
- [23] W. Blum; W. Riegler; L. Rolandi: "Particle Detection with Drift Chambers", 2. Auflage Heidelberg: Springer (2008).
- [24] K. Kleinknecht: "Detektoren für Teilchenstrahlung", 3. Aufl. Stuttgart: Teubner (1992).
- [25] A. Andronic; S. Biagi; P. Braun-Munzinger; C. Garabatos; G. Tsileidakis; "Drift velocity and gain in argon- and xenon-based mixtures", *Nucl. Instrum. Methods A* **523**, 302 (2004).
- [26] The ATLAS Collaboration, "ATLAS detector and physics performance: Technical Design Report 2", ATLAS TDR 15, CERN/LHCC 99-15 (1999).
- [27] Rudolf LEY, PS Division, CERN, 02.09.96
- [28] The CMS Collaboration, "CMS Physics Technical Design Report, Volume II: Physics Performance", *J. Phys. G: Nucl. Part. Phys.* **34** 995 (2007).
- [29] The LHCb Collaboration, "LHCb reoptimized detector design and performance : Technical Design Report", LHCb TDR 9, CERN-LHCC-2003-030 (2003).
- [30] The ALICE Collaboration, "ALICE: Technical Design Report of the Inner Tracking system (ITS)", ALICE TDR 004, CERN-LHCC-99-12 (1999).
- [31] The ALICE Collaboration, "ALICE: Technical Design Report of the Time Projection Chamber", ALICE TDR 007, CERN-LHCC-2000-001 (2000).

- [32] The ALICE Collaboration, "ALICE: Technical Design Report of the Time of Flight System (TOF)", ALICE TDR 008, CERN-LHCC-2002-016 (2002).
- [33] The ALICE Collaboration, "ALICE: Technical Design Report of the Photon Spectrometer (PHOS)", ALICE TDR 002, CERN/LHCC-99-4 (1999).
- [34] W. Sommer, Ph.D. Thesis, unpublished, "Measurements of Quarkonia with the central detectors of ALICE", Goethe Universität Frankfurt am Main, (2008).
- [35] The ALICE Collaboration; "The ALICE Transition Radiation Detector". URL http://aliceinfo.cern.ch/Public/en/Chapter2/Chap2_TRD.html From: 08/15/2011.
- [36] The ALICE Collaboration, "Definition of the ALICE Coordinate System and Basic Rules for Subdetector Components Numbering", ALICE-INT-2003-038 (2003).
- [37] J. Cuveland, Diploma Thesis, unpublished, "Entwicklung der globalen Spurrekonstruktionseinheit für den ALICE-Übergangsstrahlungsdetektor am LHC (CERN)", Ruprecht-Karls Universität Heidelberg, (2003).
- [38] D. Emschermann, private communication.
- [39] M. Al-Helwi, Diploma Thesis, "Gain Calibration of the ALICE Transition Radiation Detector with Krypton-83", Ruprecht-Karls Universität Heidelberg, (2010).
- [40] B. Lasiuk and C. A. Whitten, "Use of Krypton-83 as a calibration source for the STAR TPC." STAR Note 360, (1998).
- [41] A. Chan *et al.*, "Performance of the HPC calorimeter in DELPHI", IEEE Transactions on Nuclear Science A **42** (1995) 491.
- [42] S. Afanasiev *et al.*, "The NA49 large acceptance hadron detector", Nucl. Instrum. Methods A **430** 210, (1999).
- [43] C.L. Dunford and T.W. Burrows, Online Nuclear Data Service, Report **IAEA-NDS-150** (NNDC Informal Report **NNDC/ONL-95/10**), Rev. 95/10 (1995)9, International Atomic Energy Agency, Vienna, Austria.
- [44] H. Krieger, "Grundlagen der Strahlungsphysik und des Strahlenschutzes", 2. Auflage Heidelberg: Springer (2007).
- [45] S. Agostinelli, *et al.*, "Geant4: A simulation toolkit", Nucl. Instrum. Meth. A, vol. 506, no. 3, pp.250 - 303 , (2003).
- [46] A. Andronic, private communication.
- [47] The LCG TDR Editorial Board, "LHC Computing Grid: Technical Design Report", LCG-TDR-001, CERN-LHCC-2005-024, (2005).
- [48] J.D. Jackson, "Classical electrodynamics", 3. Edition: Wiley (1999).
- [49] ROOT Class TSpectrum, <http://root.cern.ch/root/html/doc/TSpectrum.html> From: 29/11/2011.

- [50] R. Schicker, private communication.
- [51] Y. Wang, private communication.
- [52] E. Sickling, Diploma Thesis, "Alignment of ALICE TRD Modules using Cosmic Ray Data", Westfälische Wilhelms-Universität Münster, (2009).
- [53] S. Huber, Ph.D. Thesis, "Ausrichtung des ALICE Übergangsstrahlungsdetektors sowie Zweiteilchenintensitätsinterferometrie identischer Pionen aus p+p Kollisionen bei LHC Energien von 900 GeV und 7.0 TeV", Technische Universität Darmstadt, (2011).
- [54] R.E. Kalman, "A new approach to linear filtering and prediction problems", Journal of Basic Engineering, 82:35-45, (1960).
- [55] K. Aamodt *et al.*,
URL <http://aliceinfo.cern.ch/static/alipro/html/roothtml/AliTrackFitter.html>.
From: 11/11/2011.
- [56] K. Aamodt *et al.*,
URL <http://aliceinfo.cern.ch/static/alipro/html/roothtml/AliTrackResiduals.html>.
From: 11/11/2011.

Acknowledgements

At this point I would like to take the opportunity to thank the people who helped and supported me in the work for this thesis:

At first, I want to thank my supervisor Dr. Kai Schweda, who encouraged me to enter the field of nuclear and detector physics and eventually join the ALICE TRD group in Heidelberg to write this thesis. Through his knowledge, support and experience I was able to continuously advance in my studies.

I especially want to thank Prof. Dr. Johanna Stachel for her support I received within the work for my thesis.

Prof. Dr. Dirk Dubbers I thank for his approval to be the second corrector of this thesis. In addition I would like to thank the members of the ALICE TRD group in Heidelberg for many fruitful discussions and hints for further development of my work.

Prof. Dr. Christoph Blume and Dr. Dariusz Miskowiec I would like to thank for their support concerning all questions and issues on calibration and alignment of the ALICE TRD. I also thank Dr. Anton Andronic and the ALICE team at GSI Darmstadt for their helpful advice.

For the accomplishment of the Krypton data taking I am thankful for the support of Dr. Chilo Garabatos and Nora Pitz as well as the ALICE team at CERN.

I also want to express my gratitude to Dr. Yvonne Pachmayer, Jochen Klein, Daniel Lohner and Xianguo Lu, whose office doors were always open. Through their expertise they significantly helped me to improve the analysis, and eventually this thesis.

Finally, I want to express my deepest gratitude to my family, my girlfriend and many friends who bore with me and encouraged me every day anew.

This work has been supported by the Helmholtz Association under contract number VHNG- 147 and and the Federal Ministry of Education and Research under promotional reference 06HD197D.

Erklärung

Ich versichere, dass ich diese Arbeit selbständig verfasst und keine anderen als die angegebenen Quellen und Hilfsmittel benutzt habe.

Heidelberg, den 07.12.2011

.....
Johannes Stiller